



HAL
open science

Caractérisation géométrique et mécanique multi-échelle de la dentine humaine

Wenlong Wang

► **To cite this version:**

Wenlong Wang. Caractérisation géométrique et mécanique multi-échelle de la dentine humaine. Autre. Université Paris Saclay (COMUE), 2016. Français. NNT : 2016SACLC083 . tel-01418144

HAL Id: tel-01418144

<https://theses.hal.science/tel-01418144>

Submitted on 16 Dec 2016

HAL is a multi-disciplinary open access archive for the deposit and dissemination of scientific research documents, whether they are published or not. The documents may come from teaching and research institutions in France or abroad, or from public or private research centers.

L'archive ouverte pluridisciplinaire **HAL**, est destinée au dépôt et à la diffusion de documents scientifiques de niveau recherche, publiés ou non, émanant des établissements d'enseignement et de recherche français ou étrangers, des laboratoires publics ou privés.

NNT : 2016SACL083

THESE DE DOCTORAT
DE
L'UNIVERSITE PARIS-SACLAY
PREPAREE A
“ÉCOLE POLYTECHNIQUE ET CENTRALESUPELEC”

ÉCOLE DOCTORALE N° 579
Sciences mécaniques et énergétiques, matériaux et géosciences

Spécialité de doctorat: Génie Mécanique

Par

M. Wenlong WANG

Caractérisation géométrique et mécanique multi-échelle de la dentine humaine

Thèse présentée et soutenue à Antony, le 8 Décembre 2016 :

Composition du Jury :

M, Dejou, Jacques	Professeur, Aix Marseille Université	Président
M, Huyghe, Jacques	Professeur, University of Limerick	Rapporteur
M, Grimal, Quentin	Professeur, Université Pierre et Marie Curie	Rapporteur
M, Schmitt, Nicolas	Professeur, ENS Université Paris Saclay	Examineur
M, Gourrier, Aurélien	CR, Université Grenoble Alpes	Examineur
M, Puel, Guillaume	Professeur, CentraleSupélec Université Paris Saclay	Directeur de thèse
M, Allain, Jean-Marc	MCF, Ecole Polytechnique Université Paris Saclay	Co-directeur de thèse
Mlle, Vennat, Elsa	MCF, CentraleSupélec Université Paris Saclay	Encadrante

Acknowledgment

First of all, I would like to thank my three supervisors: Prof. Allain, Prof. Vennat and Prof. Guillaume who give me the opportunity to have a scientific research experience in my life. I really appreciate it very much. I am also grateful for their expert guidance, suggestion and support.

Then, I would like to thank Dr. Gourrier, Dr. Genthial, Dr. Grimal and Dr. Xiran for their kind help and supports in confocal microscope and RUS measurement. Also, my gratitude goes to M. Hakim, M. Nicolas, M. Eric, M. Alexandre, M. Simon and Mme. Eva for technical help and supports.

Finally, I would like to express my gratitude to my family, especially to my girl Yadong, who is always supporting me, accompanying by my side and giving me the power to continue.

ABSTRACT

Human dentin is one of the main components of human tooth. It shows a hierarchical structure from a multi-scale point of view. Generally speaking, dentin can be seen as a hard biomaterial consisting in 3 phases: the porous phase made of tubules, the inclusion phase made of peritubular dentin and the matrix phase made of intertubular dentin. These hierarchical structures strongly determine its mechanical properties. The knowledge of its structure, its mechanical property and its deformation behavior due to the variation of the external environment may be useful to improve the dentin restoration process. In this work, four observation techniques (μ CT, optical microscope, ESEM and confocal microscope) have been used and compared. Particularly, confocal microscopy is proposed to allow 3D visualization of the complex dentin porous network. Compared with usual 2D observation tool, it may provide new information. For example, near the DEJ, tubules show a more complex tree structure than the Y-shaped deduced from 2D observations. These findings may also allow to achieve more realistic modeling considering the complex porous structure inside human dentin.

Later on, compression test associated with DIC was carried out within an integrated system which can control simultaneously the humidity and the temperature of the environment. Using this system, the elastic modulus of human dentin was measured to be 16.7GPa with a standard deviation of 5.1GPa. And the Poisson's ratio was found to be 0.31. The dilatation behavior of human dentin due to relative humidity was also explored. Furthermore, resonant ultrasound spectroscopy was performed in order to compare the results with these mechanical testing. At

the micro-scale, the mechanical properties of peritubular dentin and intertubular dentin were characterized by nanoindentation. The two methods used in this work (dynamic CSM method and the static unload method) present the same trends of elastic moduli for the two components. Peritubular dentin has a higher elastic modulus (26.7GPa with a standard deviation of 3.1GPa) than intertubular dentin (16.2GPa with a standard deviation of 5.5GPa). Besides, the creep behavior of dentin was assessed by nanoindentation. Four elements Maxwell-Voigt model can be used to model dentin's creep behavior.

To sum up, a morphological and mechanical study of the dentinal tissue has been performed. New techniques, such as confocal microscopy have been used and showed their usefulness in order to give new insight into the dentinal tissue. The mechanical testing protocols that have been set up at different scales will enable to better understand the structure-property relationship by using them associated with the observation tools validated in this work.

Key words: mechanical properties, human dentin, multi-scale.

CONTENTS

Introduction	1
1 Bibliography review	3
1.1 The tooth structure	4
1.1.1 The Global Structure of Human Tooth	4
1.1.2 The Structure of Human Dentin	5
1.1.3 Dentinogenesis	12
1.1.4 Evolution with Age	14
1.1.5 Dental Restoration	15
1.2 Review of Mechanical Properties of Human Dentin	17
1.2.1 Macro-scale Mechanical Properties	17
1.2.2 Micro-scale Mechanical Properties	23
1.3 Techniques Used in the Thesis	27
1.3.1 Digital Image Correlation	27
1.3.2 Nanoindentation	33
1.4 Summary of the Bibliographic Review	36
2 Multi-scale observation	39
2.1 Micro-CT Observations	39
2.2 Optical Microscope Observations	40
2.3 ESEM Observation	43

2.4	Confocal Microscope Observations	47
2.5	Summary of microstructure observation	56
3	Meso-scale Mechanical Characterization of Human dentin	59
3.1	Compression setup with Optical Imaging under Humidity and Temperature Control	60
3.1.1	Experimental setup	61
3.1.2	Sample preparation	62
3.1.3	Sample observation	63
3.1.4	Error estimation	65
3.2	In-situ Compression Test within the setup	72
3.2.1	Compression test	72
3.2.2	Influence of the Humidity	75
3.2.3	Influence of the temperature	81
3.3	Resonant Ultrasound Spectroscopy	84
3.3.1	Principle of RUS	85
3.3.2	Results of RUS	87
3.4	Summary of Meso-scale Mechanical Characterization of Human Dentin . . .	90
4	Micro-scale Mechanical Characterization	91
4.1	Nanoindentation for peri and intertubular dentin	91
4.1.1	Sample preparation	91
4.1.2	Indentation Parameters	92
4.1.3	Atomic Force Microscope observation	92
4.1.4	Results of nanoindentation	94
4.1.5	Summary of nanoindentation experiments	101
4.2	Viscoelastic behavior	102
4.2.1	Strain rate sensitivity	103
4.3	Summary of micro-scale mechanical characterization	104

5	Conclusion and Perspectives	107
5.1	Conclusion	107
5.2	Perspectives	109
5.2.1	Microscale observations and mechanical characterization by AFM . .	109
5.2.2	3D visualization with FIB-SEM	110
5.2.3	FEM modeling	112
	Bibliography	121
	Appendices	137
A	ESEM observations	139
B	Dentin Compression Tests	143
C	Humidity Dilatation Results	151
D	A New Method Combining Finite Element Analysis and Digital Image Correlation to Assess Macroscopic Mechanical Properties of Dentin	157
E	Résumé	171

INTRODUCTION

Dentin is one of the main tissue of the tooth. Its composition and complex hierarchical structures allow it to support large stresses during the mastication process. Tissue pathological changes (ex. tooth decay or cavity) or aging phenomenon can effect its strength. Knowledge of intact dentin's geometrical structures and mechanical properties is essential for predicting the consequences of micro-structural alterations. Besides, in the field of restorative dentistry, knowledge of its micro-structure and mechanical properties is also essential to understand the effects of the restorative dental procedures.

Dentin has a complex composite structure arranged at different scales from micro to macro-scale. In the literature, only a few studies are dealing with the relationship between structure and mechanical properties of dentin. Since the last century, the micro-structure and the mechanical properties of the dentinal tissue have been investigated at different scales through various techniques. Elastic property as one of the crucial parameters has been drawn a great attention. Cavities inside tooth are repaired by the resin composites. The modulus of the composite needs to match with the dentin substance in order to prevent stress concentration at the dentin-restoration interface. Moreover, numerical predictions in dentistry require the thorough knowledge of the elastic modulus of dentin. However, the reported Young's modulus of human dentin shows a great variability among all the measurements, based either on bending, indentation, tension, compression or ultrasound techniques. Four causes of the variability are inter donor, intra donor, technique artifact and experimental problems (wrong geometry). Thus, a well established evaluation of geometrical structure and mechanical characterization

of human dentin is still needed. The aim of this thesis is to explore the protocols for geometrical and mechanical characterization for human dentin, and then investigate its mechanical properties at different scales.

In this manuscript, the following parts will be presented:

In part 1, a detailed bibliography is presented. The tooth structure is illustrated. Then, dentin characteristics are presented. Hierarchical structures and mechanical properties evaluated at different scales are reviewed. Finally, two techniques used in the thesis (digital image correlation (DIC) and nanoindentation) are presented.

In part 2, different observation methods are described and used on dentin: micro computed tomography, histology, optical microscope, confocal laser scanning microscope (CLSM), and environmental scanning electron microscope (ESEM). Their advantages and disadvantages for dentin imaging are then discussed.

In part 3, an *in-situ* experimental setup was built up. It combined a mechanical test system with a controlled the environmental conditions (relative humidity and temperature). The mechanical test refers to a compression device associated with a microscope to measure the displacement by DIC. The elastic mechanical properties of human dentin are assessed by uniaxial compression. Different environmental conditions are tested and their effect are discussed. Resonant ultrasound spectroscopy (RUS) is performed as a comparison.

In part 4, nanoindentation tests are carried out in order to have the elastic moduli for each components of dentin at the micro-scale. The same approach is used to investigated the viscoelastic behavior of dentin.

Finally, a conclusion chapter summarizes the relevant results. The perspective of this work is addressed to some numerical calculations. The influence of tubules geometry and the implicit numerical model constructions based on the confocal microscope are involved.

BIBLIOGRAPHY REVIEW

The microstructure of dentin is obviously influencing its mechanical properties. So to understand those properties, it is important to start from the structural observations. Before sailing towards a proper direction, an overall view of existing knowledge concerning dentin structure and its mechanical properties is necessary. The first part of this chapter provides an overview of the dentinal tissue. It begins with an introduction to the tooth structure. Later on, it focuses on the dentin as the main constituent of the tooth. More attention is then paid to its hierarchical structures at different scales as well as its composition. The second part reviews the reported mechanical properties determined by different techniques from a multi-scale point of view. The last part presents briefly some techniques used in this work (digital image correlation and nanoindentation). Finally, the difficulties and challenges of this work are shortly discussed.

1.1 The tooth structure

1.1.1 The Global Structure of Human Tooth

A slice view of micro-computed tomography of a human tooth is shown in Fig. 1.1B. Tooth is composed of multiple constituents mainly including: the dentin, enamel and pulp. From a geometrical point of view, tooth can be divided into three parts: the crown, the neck and the root. The root part is embedded into the maxilla (upper jaw) or the mandible (lower jaw) and is covered by gums to keep its stability. A model of human mouth is shown in Fig. 1.1A. The crown part is exposed in the mouth. The neck part acts as a link between the crown and the root.

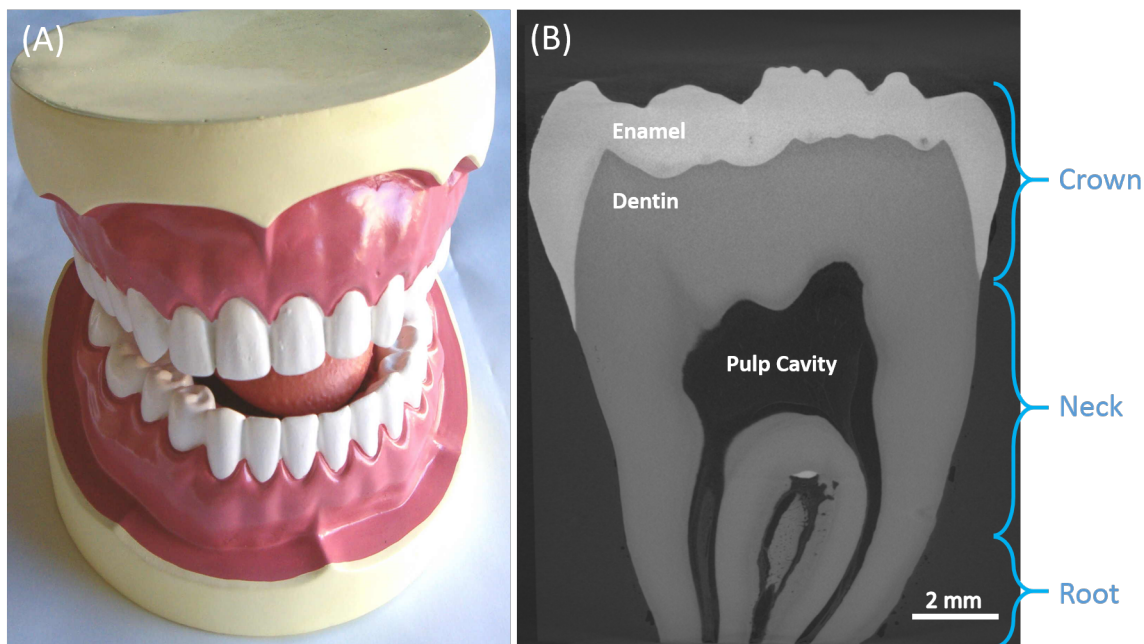


Figure 1.1 – (A) Photo of a human mouth model. (B) Slice view by micro-computed tomography of one human tooth illustrating the three main constituents: dentin, enamel and pulp.

Generally, the outermost part of the tooth is covered by enamel. It is the hardest and most highly mineralized tissue among the tooth components. Enamel contains 96% of mineral, and 4 % water and organic material [Cate-Ten 1998]. The mineral phase of enamel is mostly

hydroxyapatite, which is a crystalline calcium phosphate [Johnson et al. 1998]. This large content of minerals leads to its relatively high strength, but also a higher brittleness [Cate-Ten 1998]. Below the enamel "cap", dentin is the major part of the tooth. It is less mineralized and brittle compared with enamel [Johnson et al. 1998]. Dentin plays a very important role to endure and transfer the stresses during mastication. Under the dentinal tissue, the pulp cavity is located at the center of the tooth, and is filled with soft connective tissue. This tissue contains blood vessels and nerves so that pulp is referred as the "nerve" of the tooth.

When the tooth structure is damaged due to cavities or external trauma, a dental restoration or dental filling is commonly used to restore the function, the integrity and the morphology of the missing tooth structure. Thus, the performance of the interface between the dentin and the restorative materials directly determine if the reparation is whether successful or not [Nakabayashi et al., 1982; Pallesen & Qvist, 2003]. To be able to study this interface, a profound understanding of the dentin structure is needed. In the following section, a detailed introduction of dentin is presented.

1.1.2 The Structure of Human Dentin

Macro-scale: the organization of the tubules

Dentin contains microscopic channels which are called dentinal tubules. At macro-scale point of view, the tubules radiate outward through the dentin from the pulp to the exterior cementum or enamel border [Roosen-Runge, 1976; Fehrenbach & Popowics, 2015]. The course of the dentinal tubules is a slight S-curve in the crown, but the tubules are straighter in the incisor ridges, cusps, and root areas (see Fig. 1.2). The ends of the tubules are perpendicular to the dentinoenamel junction [Young et al., 2013].

Micro-scale

At micro-scale, dentin is composed of three parts: tubule lumen, peritubular dentin and intertubular dentin as shown in Fig. 1.3. Tubules lumen represents the porous phase. The



Figure 1.2 – Sectional view of a human incisor. Course of dentinal tubules is a slight S-curve in the crown, but straight at the incisive tip and in the root (fig. from [Young et al. \[2013\]](#)).

peritubular dentin is the surrounding ring around the tubule lumen. The intertubular dentin is the matrix surrounding peritubular dentin. Due to the dentin tubules, dentin can be seen as a porous material. The difference between peritubular dentin and intertubular dentin is the mineral content of the two components. Based on that tissue structure, dentin is often modeled as a continuous fiber-reinforced porous composite with peritubular cuffs as reinforcement and a matrix of intertubular dentin [[Wang et al., 2015](#)].

Due to its porous structure, the mechanical properties are likely influenced by its density and the dimension of tubule lumen. These parameters show a very high inter-individual variation and a location dependence, as illustrated in [Fig. 1.4](#). The values (tubule number density and tubule diameter) are higher in the deep dentin near the pulp cavity than that near the dentinoenamel junction. A bibliography survey of the density and diameter of the tubules is shown in [table 1.1](#). The number of tubules increases from 15000 - 20000 tubules/mm² near

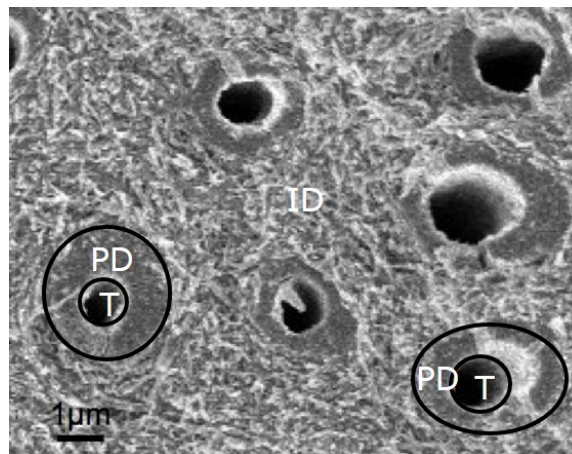


Figure 1.3 – SEM images of dentin showing the tubule lumens (T) with surrounding cuffs of peritubular dentin (PD) between the intertubular dentin (IT) matrix. The scale bar: $1\mu m$.

the DEJ to 45000- 65000 tubules/ mm^2 near the pulp cavity. The diameter of the lumen of the tubules also varies from the DEJ to the pulp surface. In coronal dentin, the average diameter of tubules at the DEJ is $0.5 - 0.9\mu m$, but it increases to $2 - 3\mu m$ near the pulp [Boushell & Sturdevant, 2014]. The statistical structure characteristics have been reviewed by Marshall et al. [1997]: the percentages of tubule area and diameter vary from about 22% and $2.5\mu m$ near the pulp to 1% and $0.8\mu m$ at the dentinoenamel junction (DEJ), and the area percentage of peritubular dentin in crown dentin varies from 60% near the pulp cavity to 3% at the DEJ. As a consequence, the intertubular matrix area varies from 18% at the pulp cavity up to 96% near the DEJ. From the data above, one may infer that the thickness of the peritubular dentin wall should vary from about $2.2\mu m$ near the pulp to $0.3\mu m$ near the DEJ.

As mentioned earlier, the dentinal tubules extend from the DEJ to the outer wall of the pulp. Near the DEJ, the tubules divide into several terminal branches, forming an intercommunicating and anastomosing network (see Fig. 1.5). As reported originally by Mjör & Nordahl [1996], three types of branches were observed and named as major, fine and micro-branches based on their sizes which appeared to be related to their locations. Major branches, $0.5 - 1.0\mu m$ in diameter, are found mainly near the dentinoenamel junction and cementumoenamel junctions. Fine branches, $0.3 - 0.7\mu m$ in diameter, are abundant in areas such as the root dentin part. Microbranches which are even smaller ($0.025 - 0.2\mu m$ in diameter), present

Table 1.1 – Overview of tubules distribution in different locations of human coronal dentin*

Reference	Investigated teeth	Donors age	Tubular density (Number/mm ²)			Tubular size (µm)			Tubule Interval (µm)
			Surface	Middle	Deep	Surface	Middle	Deep	
Ketterl [1961]	11 i	16-30	-	34,000	61,000	-	3.98	3.09	-
Garberoglio & Brännström [1976]	1 i, 24 pm, 5 m	8-60	-	35,000	43,000	-	1.2	1.9	-
Schilke et al. [2000]	30 m	18-23	-	18,781	21,343	-	2.652	2.902	-
Pashley [1989]	-	-	19,000	30,000	45,000	0.4	0.55	1.25	-
Williams et al. [2015]	-i and -m	-	-	-	-	-	-	-	5.5-7.7(i); 7.4-8.4(m)
TRONSTAD [1973]	14 i	13-61	-	-	60,000	-	2-3	< 0.5	-
Mjör & Nordahl [1996]	1 i, 2 c, 8 pm, 2 m	19-71	-	18,000	22,000	-	-	-	-
Brännström & Garberoglio [1972]	-pm	-	-	-	-	-	1.5	1.8-2.0	-
Dourda et al. [1994]	13 m	18-28	-	37,000	48,000	-	-	-	-
Boushell & Sturdevant [2014]	-	-	15,000-20,000	-	45,000-60,000	0.5-0.9	-	2-3	-
Marshall et al. [1997]	-	-	-	-	-	0.8	-	2.5	-
Mjör & Pindborg [1973]	-	-	15,000	35,000	65,000	-	-	-	-

*-, no data reported; i, incisors; pm, premolars; m, molars; Surface, near enamel part; Middle, middle dentin part; Deep, near pulp cavity. Interval, the distance between the two tubules. Table was based on the work from Schilke et al. [2000]

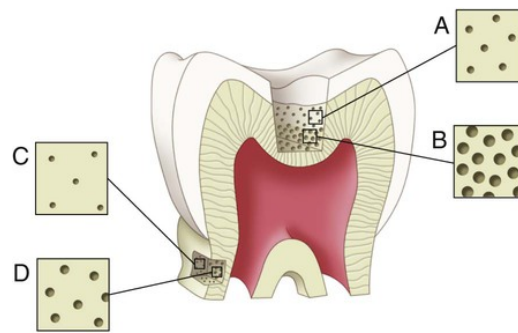


Figure 1.4 – Cartoon of a tooth, showing the variation of the tubule organization in the dentin. Tubules in superficial dentin close to the dentinoenamel junction (DEJ) (A) are smaller and more sparsely distributed compared with deep dentin (B). The tubules in superficial root dentin (C) and deep root dentin (D) are smaller and less numerous than those in comparable depths of coronal dentin (Adopted from [Boushell & Sturdevant, 2014]).

everywhere in the dentin and prolong at right angles from the tubules.

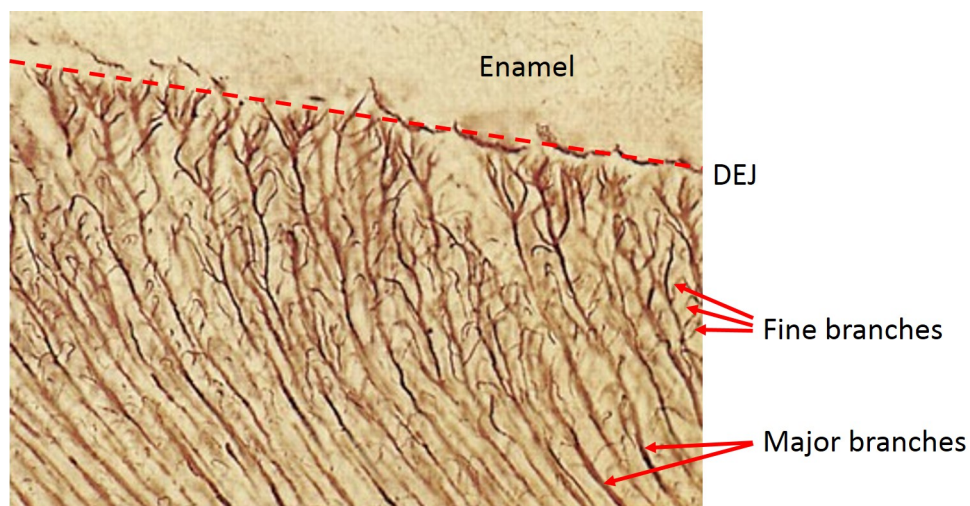


Figure 1.5 – Histological section view showing dentinal tubules and their lateral branching close to the DEJ. No scale bar was found. Image adapted from [Berkovitz et al., 2009]

It is then clear that the tubule structure of the dentin varies considerably through the dentin thickness, this will necessarily lead to a location-dependent variations in mechanical properties. Furthermore, it may also affect the permeability and the restorative bonding properties. Thus, a deep understanding of dentin structure may be crucial for predicting its mechanical behavior.

Nano-scale

At nano-scale, dentin shows a well-organized and complex structure. Approximately 50% (volume percentage) of dentin consists of nanocrystalline apatite mineral phase which is a carbonate-rich hydroxyapatite. An additional 30% (volume percentage) is occupied by a network of type I collagen fibrils, whereas the rest are mainly water [Marshall et al., 1997]. The hydroxyapatite is a mineral form of calcium apatite with the chemical formula $Ca_{10}(PO_4)_6(OH)_2$. Its crystalline structure is shown in Fig. 1.6. The c-axis is defined perpendicularly to its (002) atomic arrangement plan.

The peritubular dentin is a high mineral sheath, devoid of collagen fibrils [Gotliv & Veis, 2007], while, the surrounding intertubular dentin is a composite matrix made of protein fibrils and hydroxyapatite. The diameter of the collagen fibrils is approximately 50 – 100nm [Scott & Symons, 1967; Boyde et al., 1984; Vennat, 2009]. The fibrils arrange in a plane perpendicular to the direction of tubule (Fig. 1.6). In this plan, they are randomly distributed. The mineral hydroxyapatite is mainly extrafibrillar (meaning, it is localized in the interstices between the fibrils) [Pidaparti et al., 1996; Landis & Silver, 2002]. The shapes of the mineral hydroxyapatites are location-dependent. They continuously vary from needle-like near the pulp to plate-like near the enamel [Kinney et al., 2001]. The thickness of the crystallite is roughly 5nm, independently of the location [Kinney et al., 2003]. In the peritubular dentin, the crystals of hydroxyapatite have no overall preferred orientation [Weiner et al., 1999]. In the intertubular dentin, the apatite c-axis of mineral crystallites prefers to orient along the axis of the collagen fiber, as reported by Forien et al. [2015].

Study by Forien et al. [2015] has shown that the mineral particles aligned with collagen compressed in the intertubular dentin. This distributed stress may act as a damage prevention mechanism at nanoscale, protecting against crack initiation due to mastication loads. Various man-made engineered structures, exhibiting improved strength and endurance, benefit from incorporating residual strains/stresses. Understanding the structure of dentin may point us a new thinking direction on how to develop a tough and defect-tolerance material.

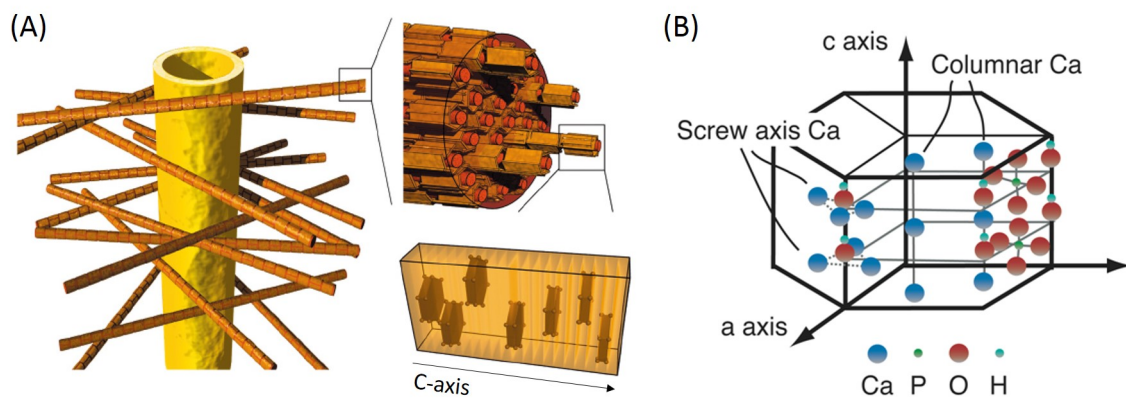


Figure 1.6 – Schematic representation of the dentin nanocomposite structure. (A) Highly mineralized peritubular dentin (yellow hollow cylinder) surrounded by mineralized collagen fibers. The fibrils arrange in a plane perpendicular to the direction of tubule. In this plan they are randomly distributed. The mineral hydroxyapatite located in the interstices between the fibrils. The c-axis of the mineral hydroxyapatite in the fibers is aligned with the collagen axis (Image from [Forien et al., 2015]). (B) Crystalline structure of the hydroxyapatite (adopted from Internet).

At nanoscale, bone and dentin are quite similar: they consist of an inorganic hydroxyapatite mineral and a collagen fibril matrix. Both bone and dentin have heterogeneous, hierarchical, composite structures [Boskey, 2007]. However, they are different from how they are built to how they respond to injuries. The illustration of the micro-structure for the cortical bone is shown in Fig. 1.7. It consists of structural unit (osteon), which is composed of a lamellar cuff embedded in a disorganized matrix. Tubule-like structures (Haversian canals) exist at the center of the osteons. Although it reminds the dentinal structures (tubule, peritubular and intertubular dentin), the bone structures are in fact quite different in the organization. Another major difference comes from the regeneration: while bones are dynamic structures constantly developing, repairing by the cells inside it, the dentin seems to lack such regeneration capacity. Unlike bone, if dentin is damaged, it can not heal itself or regrow the tissue that has been lost. The regeneration of pulp tissue can be encased in dentin because the environment in dentin can not provide sufficient blood. Thus, at the base of the roots of the teeth, cells in pulp plasma system can provide a certain amount of repair for dentin. But the enamel doesn't have the regenerative power at all [Huang, 2009].

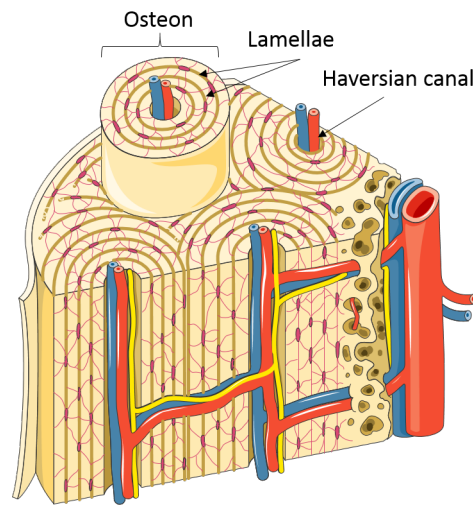


Figure 1.7 – Illustration of cortical bone micro-structure (adopted from the free PowerPoint image bank Servier Medical Art).

1.1.3 Dentinogenesis

Dentin formation (dentinogenesis) is accomplished by odontoblasts cells [Boushell & Sturdevant, 2014]. Odontoblasts are considered as part of pulp and dentin tissues: their cell bodies are in the pulp cavity, and their long, slender cytoplasmic cell processes (the so-called Tomes fibers) extend well (100-200 μm) into the tubules of the dentin (see Fig. 1.8). Because of these odontoblastic cell processes, dentin has the capability to react to physiologic and pathologic stimuli. Tomes fibers occasionally cross the DEJ into enamel. They may serve as pain receptors, explaining the enamel sensitivity experienced by some patients during tooth preparation [Boushell & Sturdevant, 2014].

Dentin formation begins immediately before enamel formation. Dentin formation begins at areas subjacent to the cusp tip or incisal ridge and gradually spreads to the apex of the root. Odontoblasts generate an extracellular collagen matrix as they begin to move away from the adjacent ameloblasts (cells used for formation of enamel). Their secretion gradually modifies the extracellular collagen matrix into a mineralized matrix. The most recently formed layer of dentin is always on the pulpal surface. This unmineralized zone of dentin is next to the cell bodies of odontoblasts (see Fig. 1.8). In contrast to enamel formation, dentin formation

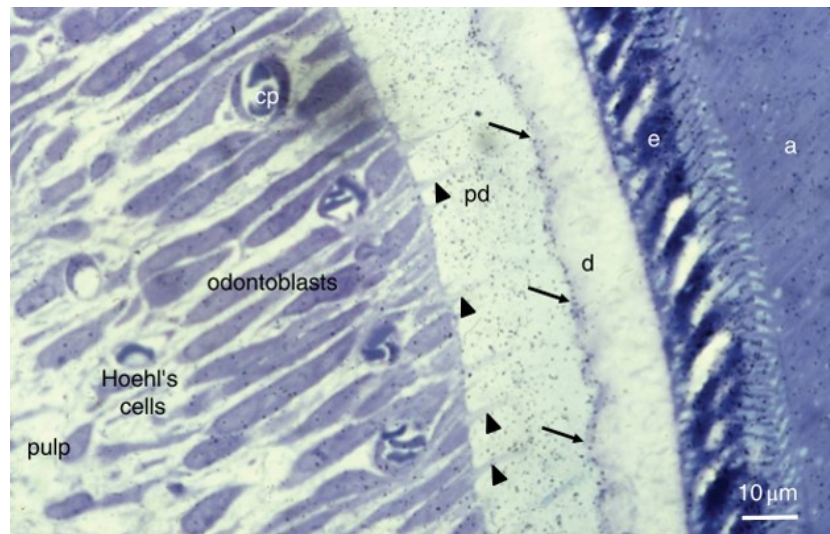


Figure 1.8 – Light microscope image of odontoblasts and forming dentin. On the right, enamel (e) is formed by secretory ameloblasts (a). The mineralization front (arrows) located at the edge of the dentin layer (d). Odontoblast processes (arrowheads) extend through the predentin (pd). Hoehl's cells inside pulp may differentiate into odontoblasts. (Image from [Hand & Frank, 2014]).

continues after tooth eruption and throughout the life of the pulp. The dentin forming the initial shape of the tooth is called primary dentin and is usually completed 3 years after tooth eruption (for permanent teeth). Once the primary dentin is formed, the dentin deposition continues at a reduced rate under physiological conditions: this new type of dentin is called secondary dentin (see Fig. 1.9). In contrast to primary dentin, the tubules have a slightly different orientation in secondary dentin. Secondary dentin is created on the whole surface of the pulp cavity. More secondary dentin is deposited on the roof and floor of the coronal pulp chamber than on the lateral walls [Avery & Steele, 2006]. Compared with primary dentin, the tubules in secondary dentin are less numerous. The structure and composition of secondary dentin are similar with primary dentin [Hand & Frank, 2014].

When moderate non-physiological stimuli are applied to dentin (as caries, attrition or some operative procedures), some affected odontoblasts may die. Replacement odontoblasts (termed secondary odontoblasts) that originate from the pulp start to synthesize reparative dentin (called tertiary dentin). The reparative dentin usually appears as a localized deposit in the pulp cavity immediately subjacent to the injured area in the tooth, just underneath the af-

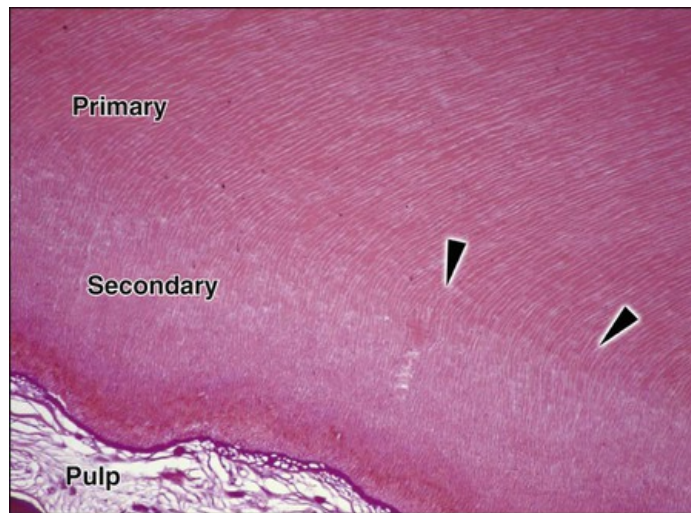


Figure 1.9 – Photomicrograph for the histological sectional view of dentin in pulp area. The tubules have a slightly different orientation in secondary dentin. Arrowheads indicate the junction between the primary and secondary dentin. The color in the image is resulted by the histologic stains (The specific information is not mentioned). Image is adopted from [Nanci, 2008].

fectured tubules (see Fig. 1.10). The tertiary dentin may be deposited rapidly, in which case the resulting dentin appears irregular with sparse and twisted tubules. In contrast, if it is formed slowly because of fewer stimuli, it appears more regular, much like primary or secondary dentin [Avery & Steele, 2006].

1.1.4 Evolution with Age

The age-induced changes are much more obvious in dentin than in enamel. The dentin of aging people is characterized by a continuous narrowing of the lumen of the tubules, an increasing calcification in peritubular dentin resulting in a gradual reduction of the tubule diameter [Ketterl, 1983]. This continued deposition often leads to complete closure of the tubule (physiologic sclerotic). The dentin associated with physiologic sclerotic dentin is more brittleness and less permeable [Nanci, 2008]. At some points, sclerotic dentin may arise due to slowly advancing caries. It causes an alteration in the primary dentin composition. The peritubular dentin becomes wider, gradually filling the tubules with calcified material, progressing from the DEJ to pulp as shown in Fig. 1.11. These areas are harder, denser, less

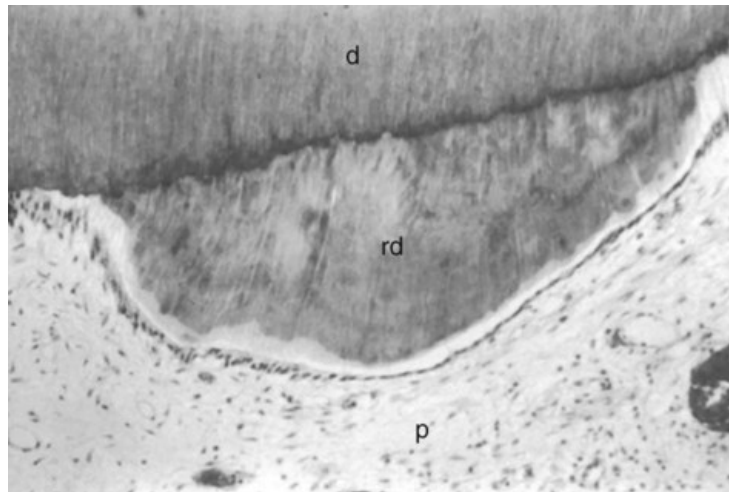


Figure 1.10 – Histological image shows the reparative dentin (rd) in response to a carious lesion (d, dentin, p, pulp) adopted from [Trowbridge, 2003].

sensitive, and more protective of the pulp against subsequent attack [Boushell & Sturdevant, 2014].

1.1.5 Dental Restoration

Dental restoration or dental filling consist in the use of a dental restorative material to restore the function, the integrity and the morphology of missing tooth structure. The structural loss typically results from caries or external trauma. It can be divided into two broad types: direct restorations and indirect restorations [Stappert et al., 2006].

Direct restorations involve placing a soft or malleable filling into the prepared tooth and building up the tooth before the material sets hard. The advantage of direct restorations is that they usually set quickly and can be placed in a single procedure.

Indirect restorations are fabricated outside of the mouth (for example, using a CAD/CAM system). The restoration is usually bonded permanently with a dental cement or resin. One of the indirect restoration process is based on CAD/CAM technology. An optical impression of the prepared tooth is taken using a camera. Next, a specific software takes the digital picture and converts it into a 3D virtual model. A ceramic block that matches the tooth shade is

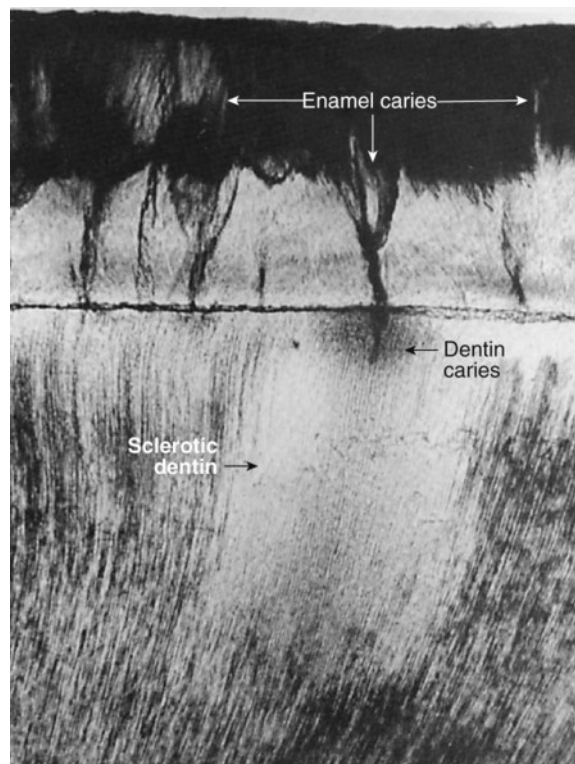


Figure 1.11 – Photograph of the sclerotic dentin occurring under enamel caries(Image from [Avery & Steele, 2006]).

placed in the milling machine. An tooth-colored restoration is machined and ready to bond in place [Van Nieuwenhuysen et al., 2003].

Materials like casting alloys (gold, titanium and etc.), composite resin, glass ionomer cement and dental porcelain are often used in the restoration [Lange & Pfeiffer, 2009; Pallesen & Qvist, 2003]. A key element is the interface between dentin and restorative material. In particular, the standard method is to create a "hybrid layer" between a resin composite and the dentin. This layer is reached firstly by removing the mineral phase at the surface of the dentin (around $20\mu m$ of depth). In that layer, the collagen network is exposed. Then, the restorative resin is infiltrated into the collagen network, and create this layer (see Fig. 1.12). The restorative process is then completed by filling the remaining cavity by a photopolymerizable composite. The durability of such restoration stems from the quality of the hybrid layer. The thickness and mechanical properties will directly affect the restoration process and its durability.

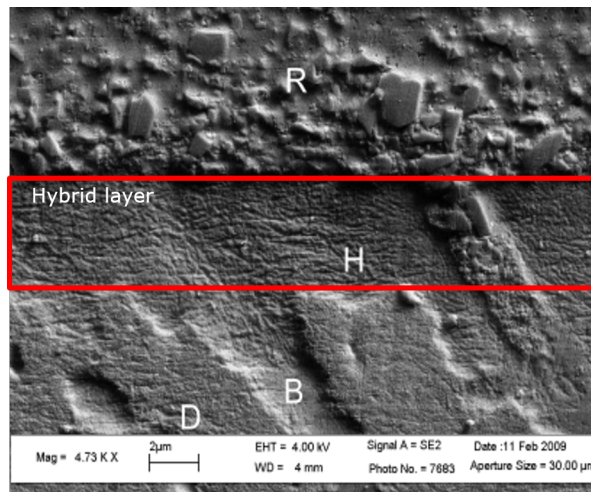


Figure 1.12 – SEM image of hybrid layer. Labeling: hybrid layer (marked with H inside the red rectangle), restorative resin (marked with R), dentin (marked with D), resin branch from hybrid layer (marked with B). Image adopted from [Vennat, 2009].

Thus, a better understanding of the dentin structure, mechanical properties and the relationship between them appears essential. Further issues, such as the influences of resin infiltration, the bonding strength and durability of the hybrid layers will request further attention.

1.2 Review of Mechanical Properties of Human Dentin

In this section, mechanical properties of human dentin are reviewed from a multi-scale point of view. The first part deals with the macro-scale properties. The anisotropic characteristics are studied through tensile, compression and bending tests. Viscoelastic behavior is also reviewed. Finally, the few fracture mechanics and fatigue studies are briefly presented. In the second part, the properties of the local components (peritubular and intertubular dentin), studied by micro-pillar compression test, nanoindentation and AFM are reviewed.

1.2.1 Macro-scale Mechanical Properties

Dentin is a composite made of oriented tubules, peritubular and intertubular dentin, as presented in the previous section. Assuming the changes of the morphology of the tubules

are small in the longitudinal direction, dentin can be approximately described as a transverse isotropic material (see Fig. 1.13) [Kinney et al., 2003, 2004; Lees & Rollins, 1972]. Dentin compression results from Peyton et al. [1952] have shown that the fracture occurs at a small strain (around 2%), so a description limited to linear elasticity should be sufficient. The relation between stress σ and strain ε for transverse isotropic materials can be described by the classical relationship:

$$\begin{bmatrix} \varepsilon_{xx} \\ \varepsilon_{yy} \\ \varepsilon_{zz} \\ 2\varepsilon_{yz} \\ 2\varepsilon_{xz} \\ 2\varepsilon_{xy} \end{bmatrix} = \begin{bmatrix} \frac{1}{E_t} & -\frac{\nu_{tt}}{E_t} & -\frac{\nu_{tl}}{E_t} & 0 & 0 & 0 \\ -\frac{\nu_{tt}}{E_t} & \frac{1}{E_t} & -\frac{\nu_{tl}}{E_t} & 0 & 0 & 0 \\ -\frac{\nu_{tl}}{E_t} & -\frac{\nu_{tl}}{E_t} & \frac{1}{E_l} & 0 & 0 & 0 \\ 0 & 0 & 0 & \frac{1}{G_{tl}} & 0 & 0 \\ 0 & 0 & 0 & 0 & \frac{1}{G_{tl}} & 0 \\ 0 & 0 & 0 & 0 & 0 & \frac{2(1+\nu_{tt})}{E_t} \end{bmatrix} \begin{bmatrix} \sigma_{xx} \\ \sigma_{yy} \\ \sigma_{zz} \\ \sigma_{yz} \\ \sigma_{xz} \\ \sigma_{xy} \end{bmatrix}$$

where E_t , E_l are the transverse and longitudinal modulus respectively, ν_{tl} , ν_{tt} are the associated Poisson's ratios, and G_{tl} is the shear modulus in longitudinal direction.

These transverse and longitudinal moduli have been widely investigated experimentally since the middle of the last century [Bowen & Rodriguez, 1962; Sano et al., 1994; Kinney et al., 2003], using either compression or traction experiments, as summarized in table 1.2. Through tensile tests, the elastic modulus was reported to be 19.3 GPa with a larger deviation (28%) using an optical strain gauge to determine the strain [Bowen & Rodriguez, 1962]. The elastic modulus (E_t) have been estimated to be 13-15 GPa using a strain gauge [Sano et al., 1994]. Through compressive tests, the elastic modulus of human dentin was determined to be 11.6 GPa [Peyton et al., 1952]. In that paper, strain gauges were attached to the steel rods used to apply the load on the dentin. Later publications report a compressive modulus value of around 14 GPa [Stanford et al., 1960; Palamara et al., 2000]. A modulus of 18.5 GPa was reported after load-unload cycles with the strain gauge directly onto the sample [Craig & Peyton,

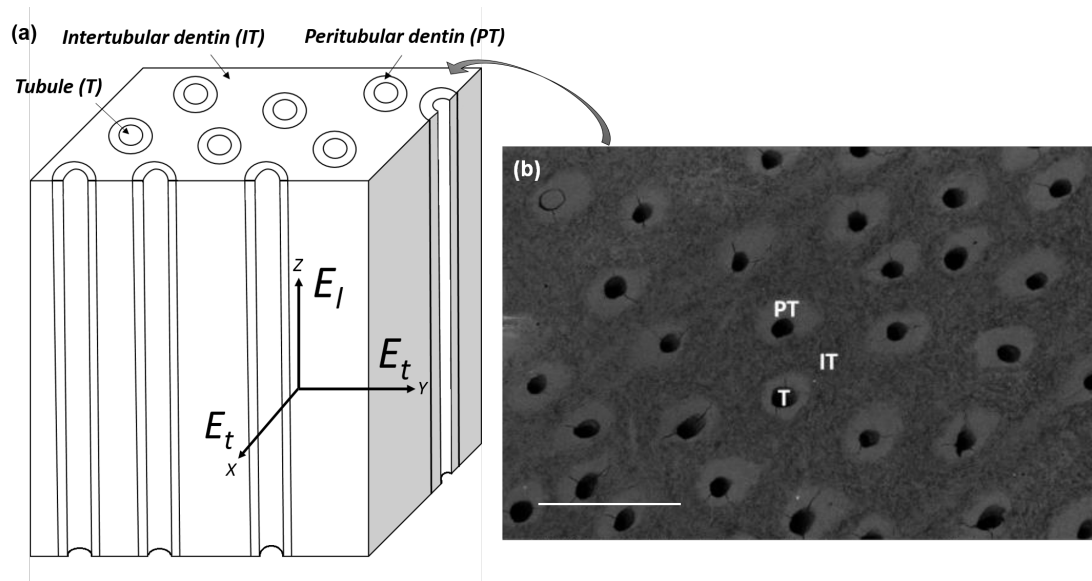


Figure 1.13 – (a) Idealized dentinal structure: the directions of longitudinal modulus (E_l) and transverse modulus (E_t) respectively aligned and perpendicular to the tubules main orientation. (b) Scanning electron microscopy image from the top view of dentin, with the identification of regions of peritubular dentin (PT), intertubular dentin (IT), and a tubule (T). Scale bar: $10\mu m$.

1958]. These large range of moduli obtained in compression may arise from the non-parallel faces of the samples. Recently, Zaytsev & Panfilov [2014] reported elastic modulus values within a range of 3 to 13 GPa as a function of the geometry of the sample. Unfortunately, they did not indicate the method used for the strain measurement. Finally, diametrical compressive and classical compressive tests were performed by Palamara et al. [2000] using digital image correlation (DIC) for strain determination. They obtained moduli of 6.5 ± 2 GPa and 10.7 ± 2.4 GPa, respectively. The measured elastic moduli may be affected by the strain rate if the dentin is viscoelastic. Jantarat et al. [2002] reported a linear dependence of the measured elastic modulus as a function of strain rate (see in Fig. 1.14). It was indicated that the variations on the six decades of the strain rates (corresponding to the experimental range) are lower than the inter-samples variability.

Bending tests seem to be more rarely used, probably due to the fact that small bending setups are not common. Nevertheless, three-point [Rees et al., 1994] or four-point [Ryou et al., 2011] bending tests were used to assess dentin mechanical properties. Rees et al. [1994]

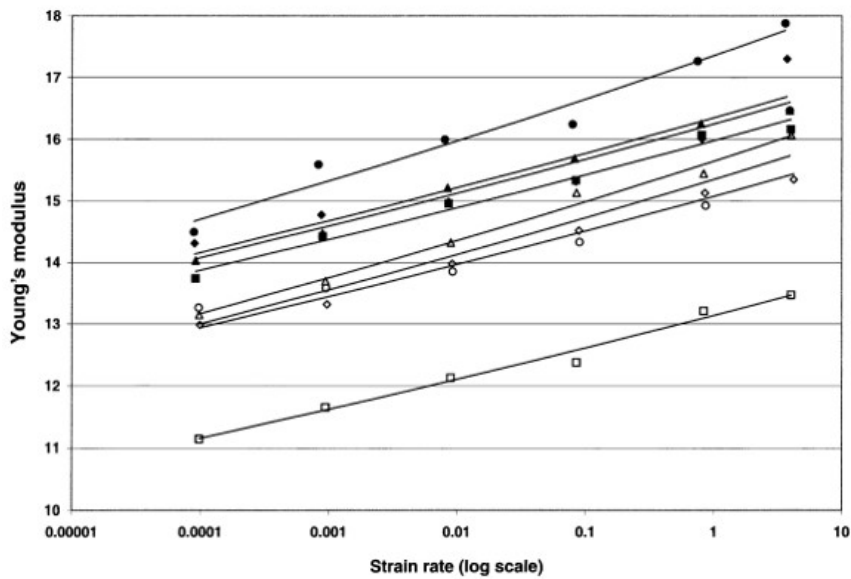


Figure 1.14 – Influence of strain rate on elastic modulus for eight dentin samples, each subjected to six rates of loading (Image from [Jantarat et al., 2002]). The unites for Young's modulus and strain rate are GPa and s^{-1} , respectively.

determined a static elastic modulus of 8.6 ± 0.86 GPa and dynamic storage modulus ranging from 14.3 to 15.9 GPa in the frequency range of 0.1 to 10 Hz. Ryou et al. [2011] obtained an elastic modulus (13-17 GPa) depending on the location.

Ultrasound spectroscopies were also used to determine dentin mechanical properties. Critical angle reflection technique gave a modulus of 36 GPa in the tubule direction (E_l) and 29 GPa in the perpendicular axis (E_t) [Lees & Rollins, 1972]. Resonant ultrasound spectroscopy (RUS) measurements gave different values (from 23 to 25 GPa) [Kinney et al., 2004].

Table 1.2 summarizes the different values of dentin elastic modulus and ultimate strength found in the literature. A wide range of values was obtained using great number of methods for stress and strain assessments.

Fracture properties of dentin were less studied. The intrinsic fracture toughness was measured as $3.08 MPa\sqrt{m}$ with a deviation 10% for coronal dentin [El Mowafy & Watts, 1986]. It was shown that the fracture toughness was high for such a brittle material because either the collagen fibrils or the tubules provide a toughening mechanism. Furthermore, Imbeni et al. [2003] used three point bending test with different notches (a fatigue precrack or artificial

Table 1.2 – Literature review of the macro-scale mechanical properties of human dentin (elastic modulus units: GPa, stress unit: MPa).

Methods	E_l	E_t	$\sigma_{bending}$	$\sigma_{compression}$	$\sigma_{tension}$	ϵ measure	σ measure
RUS [Kinney et al., 2004]	25.0	23.3					
RUS [Lees & Rollins, 1972]	36.0	29.0					
Diametrical compression [Palamara et al., 2000]	6.5 ± 2.0	6.5 ± 2.0			50.9–58.7	DIC	$\sigma_{compression} = \frac{6F}{\pi Dt}$
Compression [Palamara et al., 2000; Neumann & Dr-Salvo, 1957; Craig & Peyton, 1958; Peyton et al., 1952]	E ranged in 1.6-18.3			294–333 [Palamara et al., 2000] 230–300 [Craig & Peyton, 1958; Peyton et al., 1952]		DIC	$\sigma = \frac{F}{S}$
Three-point bending [Rees et al., 1994; Zaytsev & Panfilov, 2014]	E ranged in 8.9-14.5					Crosshead (deflection assessment)	Beam equation
Four-point bending [Eltit et al., 2013; Arola & Reprigel, 2005]	E ranged in 12.1-16.9	145–326				Crosshead (deflection assessment)	Beam equation
Four-point bending [Arola & Reprigel, 2006]	18.7 ± 3.5	15.5 ± 2.8				Crosshead (deflection assessment)	Beam equation
Tension [Bowen & Rodriguez, 1962; Marshall et al., 1997; Sano et al., 1994]		6.0–19.3			30–130	Strain gauge	$\sigma = \frac{F}{S}$
Cantilever bending [Renson & Braden, 1975]	E ranged in 11.1-19.3						Beam equation

d is the crosshead displacement; L is the length of sample in compression direction; F is the load from the compression device; S is the cross section area of the specimen; D is the diameter of cylindrical sample; t is the thickness of cylindrical sample.

notch with root radius ranging from 30 to 50mm) to test the fracture toughness. It was shown to be 1.8 ± 0.1 and $2.7 \pm 0.1 \text{ MPa}\sqrt{m}$ for two notches, respectively. The shape of the crack play a important role during this kind of test.

Due to the mastication of the tooth, the fatigue behavior of the dentin sounds important. The frequency of the loading during the mastication is around 1 Hz, and stress amplitudes about 20 MPa were estimated by Anderson [1956]. Fatigue loading at a constant load ratio (0.1) and at two different cyclic frequencies (2 and 20 Hz) were used to determine the fatigue behavior of human dentin by Nalla et al. [2003]. A fatigue limit at 10^6 cycles was reported to be around 25 and 45 MPa at frequencies of 2 and 20 Hz, respectively. The initiation and growth of a single, dominant crack is the main reason for the failure. A threshold stress intensity of $1.1\text{MPa}\sqrt{m}$ was also estimated. It seems that the mastication stress would not result in a fatigue failure in the dentin tissue.

Effect of Temperature and Relative Humidity

External environmental conditions (ex. temperature and relative humidity) play an important role in dentin mechanical behavior. During a general dental operation, air relative humidity is known as a key factor which determines the quality of bonding between the restoration material and the dentin substrate [Plasmans et al., 1993]. It has been shown that the bonding systems used in tooth reparation are highly sensitive to extrinsic dentin wetness, with a very low adhesion at high air relative humidity [Plasmans et al., 1993; Burrow et al., 1995; Plasmans et al., 1996]. The mechanical properties of dental restorative composites were examined under different the environmental conditions. No significative influence was observed on flexural modulus or strength [Walker et al., 2006]. However, almost no study can be found concerning the influence of different environmental conditions on the mechanical properties of dentin.

1.2.2 Micro-scale Mechanical Properties

Various techniques, such as nanoindentation, AFM or micro-pillar compression have been used to determine the mechanical properties of human dentin at micro-scale. A summary of the results is shown in [table 1.3](#).

Nanoindentation is the natural choice to study the local moduli at the scale of tubules and their peritubular cuffs [[Kinney et al., 1996](#); [Ziskind et al., 2011](#); [Chien et al., 2012](#)]. [Kinney et al. \[1996\]](#) had measured the Young's moduli of dehydrated peritubular and intertubular dentins with a nanoindenter, using the unloading part of the load displacement curve. They found an average elastic modulus of 29.8 GPa for the peritubular dentin [Kinney et al. \[1996\]](#), and in the range of 17.7 to 21.1 GPa for intertubular dentin, with a lower value obtained near the pulp. On dry dentin, a gradual decrease in Young's modulus was observed from the bulk of the peritubular region (values up to 40–42 GPa), to the intertubular dentin region (approximately constant values of 17 GPa) [[Ziskind et al., 2011](#)]. The intertubular region can be considered to be quasi-isotropic, with a slightly higher modulus value (22 GPa) when the indenting tip axis is parallel to the tubular direction, compared to the values (18 GPa) obtained when the indenting tip axis is perpendicular to the tubule direction [[Ziskind et al., 2011](#)].

[Angker et al. \[2004\]](#) studied the relationship between the mechanical properties of carious dentin, obtained by indentation, and the mineral content, determined using backscattered scanning electron imaging. Their results show that the mechanical properties of dentin are strongly correlated to its mineral content (see [Fig. 1.15](#)). They found an exponential increase of the modulus with the mineralization. Thus, the decreases in mechanical properties of carious dentin, namely hardness and elastic modulus, are directly linked to the reduction of its mineral content.

Fracture toughness was also evaluated by indentation technique [[Imbeni et al., 2005](#)]. It was found to be $3.75 \text{ MPa}\sqrt{\text{m}}$ at dentin enamel junction. This was 5 to 10 times higher than in enamel but 75 % lower than in dentin.

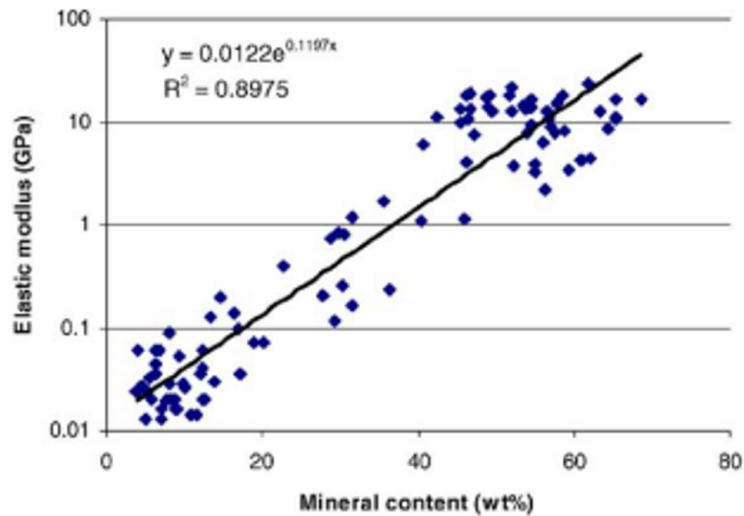


Figure 1.15 – Elastic modulus data of all specimens plotted on a logarithmic scale against mineral content. The data are fitted to an exponential relationship (figure from [Angker et al., 2004]).

Atomic Force microscopy (AFM) is also an interesting method to study the local mechanical properties [Kinney et al., 1999; Balooch et al., 2004; Ryou et al., 2012]. Values of the Young's moduli of the peritubular and intertubular dentins were reported around 30 and 15 GPa respectively [Kinney et al., 1999]. Dynamic modulus maps were also drawn using AFM [Balooch et al., 2004; Ryou et al., 2012]. The study by Balooch et al. [2004] reported that the storage modulus of the intertubular dentin varied between 17 and 23 GPa with a mean value of 21 GPa. Similar result was also found by Ryou et al. [2012] with a mean storage modulus of 19.2 GPa for intertubular dentin and a storage modulus of 31.3 GPa for peritubular dentin. AFM was also used to study the fracture properties by AFM as well [Marshall et al., 2001]. The fracture toughness values was reported as $0.6\text{--}0.9 \text{ MPa}\sqrt{m}$ for enamel, and as $2.8\text{--}3.1 \text{ MPa}\sqrt{m}$ for dentin.

More recently, anisotropic properties related to the tubule orientation were investigated through micro-pillar compression tests [Ziskind et al., 2010; Han et al., 2012]. An array of the dentin pillars (size around $10\text{--}20 \mu\text{m}$) were milled by ultra short laser pulses from a block of dentin. These pillars could then be individually tested in compression with a flat nanoindenter. The modulus was reported in the range of 13-16 GPa depending of the tubule orientation [Han

[et al., 2012](#)], or in the range of 3.5 to 13.0 GPa [[Ziskind et al., 2010](#)]. One of the limitations of these micro-pillar assays is that only ten tubules per pillar could be observed, which is slightly lower than what should be to have a true Representative Volume Element (RVE) [[Grimal et al., 2011](#)].

Table 1.3 – Literature review of the micro-scale mechanical properties of human dentin (elastic modulus units: GPa, stress unit: MPa).

Reference	Sample	Methods	E_p	E_i	$E_{composite}$	$K (MPa\sqrt{m})$	Depth or load
Kimney et al. [1996]	intact dentin	Nanoindentation	29.8	17.7-21.1			500,200,50nm
Ziskind et al. [2011]	intact dentin	Nanoindentation	40-42	18-22			200-300 μN
Imbeni et al. [2005]	DEJ	Indentation				3.75	20-50 μm
Kimney et al. [1999]	intact dentin	Modified AFM	30	15			400-700 μN
Balooch et al. [2004]	intact dentin	Dynamic modulus map (AFM)		21 (s)			
Ryou et al. [2012]	intact dentin	Dynamic modulus map (AFM)	31.3 (s)	19.2 (s)			
Marshall et al. [2001]	Enamel	AFM				0.6-0.9	
Ziskind et al. [2010]	intact dentin	Micro-pillar compression			3.5-13.0		
Han et al. [2012]	intact dentin	Micro-pillar compression			13-16		
Angker et al. [2004]	carious dentin	ultra-micro indentation			23.1		700-19,750nm

E_p is the elastic modulus of peritubular dentin; E_i is the elastic modulus of intertubular dentin; $E_{composite}$ is the elastic modulus at micro-scale for micro-pillar compression; K is fracture toughness; s means storage modulus.

1.3 Techniques Used in the Thesis

In this section, two of the techniques used in the thesis are briefly introduced: digital image correlation and nanoindentation.

1.3.1 Digital Image Correlation

This section is largely based on the work of Allais et al. [1994], Doumalin & Bornert [2000] and Bornert et al. [2009]. Precise strain measurement is necessary to determine accurately the mechanical properties. One of the most frequently used method is the Digital Image Correlation (DIC). It is an optical method based on image analysis to obtain accurate 2D and 3D displacements. DIC is now frequently used, especially in micro and nano-scale mechanical testing applications, due to its relative ease of implementation and robustness [Chu et al., 1985; Doumalin & Bornert, 2000; Sutton et al., 2009]. It has been used in engineering structures studies [Peters & Ranson, 1982; Chu et al., 1985; Sutton et al., 1993; Lu et al., 1997], the engineering materials studies [Zhao & Jin, 1996; Zhang et al., 1999; Bastawros et al., 2000; McGowan et al., 2001] even at large strain (greater than 50%) [Tong, 1997; Wattrisse et al., 2001]. In recent years, the improvement of DIC has been focused on controlling the various sources of errors [Schreier et al., 2000; Bornert et al., 2009; Wang et al., 2009]. Due to this advantages and also to its contactless measure ability and its robustness, DIC has also been widely used in the field of biomechanics [Verhulp et al., 2004; Zhang & Arola, 2004; Sztefek et al., 2010].

Principle of DIC

DIC is used to measure the *in-plane* components of displacement field in the observation zone by searching the same matching-subsets between the reference image and the deformed one. To do so, a subset domain is selected in the reference image around a chosen position. Then, the correlation is performed by searching the most alike subset in a predefined search

zone of the deformed image (see Fig. 1.16). A parameter, known as "correlation coefficient", quantifies the similarity level of the two subset domains, generally based on the comparison of the grey levels. Its minimum determines the new position of the subset in the deformed image.

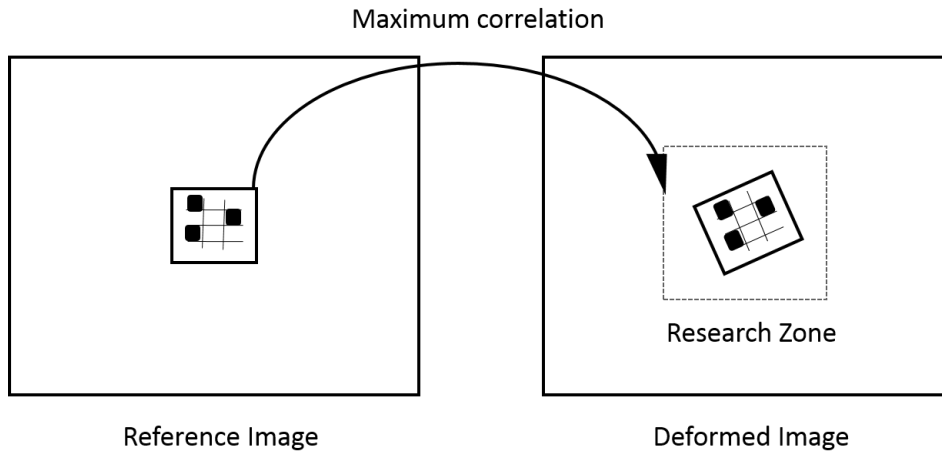


Figure 1.16 – Principle of the DIC technique.

Correlation coefficient (CMV approach)

Correlation coefficient can be defined in different forms. The software we used CorrelManuv, developed by M. Bornert, was based on the normalized correlation coefficient [Doumalin, 2000]:

$$C(\Phi) = 1 - \frac{\sum_{\mathbf{X} \in D} [f(\mathbf{X}) - \bar{f}][g(\mathbf{x}) - \bar{g}]}{\sqrt{\sum_{\mathbf{X} \in D} [f(\mathbf{X}) - \bar{f}]^2 \sum_{\mathbf{X} \in D} [g(\mathbf{x}) - \bar{g}]^2}} \quad \text{with} \quad \mathbf{x} = \Phi(\mathbf{X}) \quad (1.1)$$

where $f(\mathbf{X})$ is the grey level at pixel \mathbf{X} in reference image while $g(\mathbf{x})$ is the grey level at pixel \mathbf{x} in deformed image, related to \mathbf{X} by the tested transformation Φ . \bar{f} and \bar{g} are means value of the grey level matrices, f and g , over these subsets.

In a digital image, the pixel limits the resolution. Nevertheless, sub-pixel resolution on the displacement can be reached by interpolation. In practice, two kinds of interpolation are used:

interpolation of grey levels and interpolation of correlation coefficients [Doumalin, 2000].

Material transformation

Performing the correlation on different subsets (at different localizations), we obtain a discrete displacement fields between reference and deformed images. The next step is to determine the material transformation Φ which gives the current position \mathbf{x} from the position \mathbf{X} in reference configuration:

$$\mathbf{x} = \Phi(\mathbf{X}) \quad (1.2)$$

It can be rewritten as:

$$\Phi(\mathbf{X}) = \mathbf{X} + \mathbf{u}(\mathbf{X}) \quad (1.3)$$

where \mathbf{u} is the displacement vector at point \mathbf{X} . Consider \mathbf{X}_0 is a point in the reference image (the center of a correlation domain D), then the transformation of a point \mathbf{X} near \mathbf{X}_0 can be expanded by Taylor's series:

$$\Phi(\mathbf{X}) = \mathbf{X} + \mathbf{u}(\mathbf{X}_0) + \frac{\partial \mathbf{u}}{\partial \mathbf{X}}(\mathbf{X}_0) \cdot (\mathbf{X} - \mathbf{X}_0) + \frac{1}{2}(\mathbf{X} - \mathbf{X}_0) \cdot \frac{\partial^2 \mathbf{u}}{\partial \mathbf{X}^2}(\mathbf{X}_0) \cdot (\mathbf{X} - \mathbf{X}_0) + \dots \quad (1.4)$$

This equation expressed with different orders provides different approximation levels of the transformation Φ on the correlation domain D . In practice, such an approximation is exclusively performed at the orders of 0 (a translation) and of 1 (corresponding to a translation and homogeneous deformation of the domain). Certainly, higher orders could be used to describe more accurately the transformation matrix. The small size, of the order of few pixels, of the domain D limits the accuracy on the higher order terms. The use of larger domains is possible but the deformation of the domain in the current configuration prevents an accurate positioning, apart by having an appropriate guess of the strain. Indeed, even the first order approximations are often done iteratively: the strain is estimated by zero order method, which is used as an input for the first order calculation.

Strain measurement

The Lagrangian transformation Φ has been defined in Eq. (1.4), and the gradient of this transformation at \mathbf{X} can be written as:

$$F(\mathbf{X}) = \frac{\partial \Phi}{\partial \mathbf{X}}(\mathbf{X}) = \mathbf{I} + \frac{\partial \mathbf{u}}{\partial \mathbf{X}}(\mathbf{X}) \quad (1.5)$$

where \mathbf{I} is the second order identity tensor. The Green-Lagrange strain is defined as follows:

$$\mathbf{E} = \frac{1}{2}(\mathbf{F}^T \cdot \mathbf{F} - \mathbf{I}) \quad (1.6)$$

where \mathbf{T} denotes the transpose of a tensor. For the case of small deformation ($|\frac{\partial \mathbf{u}}{\partial \mathbf{x}}| \ll 1$), typically a few percents of strain and a few degrees of rigid rotation, the small strain tensor can be expressed with a linearized expression:

$$\boldsymbol{\varepsilon} = \frac{1}{2}(\mathbf{F}^T + \mathbf{F}) - \mathbf{I} \quad (1.7)$$

Evaluation of transformation gradient and deformation

Evaluation of the transformation gradient is crucial but difficult in practice. First, the displacement field is evaluated by DIC discretely (at each subset center). Thus, its derivate has to be evaluated by finite difference methods or the finite element methods [Gaye, 2015].

In finite difference method, the theoretical derivative can be replaced by a finite difference with respect to certain gauge length Δl . The simplified displacement gradient tensor can be calculated as [Germaineau, 2007]:

$$\begin{aligned} \frac{\partial \alpha}{\partial x} &= \frac{\alpha(X_0 + l, Y_0) - \alpha(X_0 - l, Y_0)}{2l} \\ \frac{\partial \alpha}{\partial y} &= \frac{\alpha(X_0, Y_0 + l) - \alpha(X_0, Y_0 - l)}{2l} \end{aligned} \quad (1.8)$$

where $\alpha = uorv$ and l_0 is the distance of the regular grid. Eq. (1.8) allows calculating the displacement gradient. Then, the Green-Lagrange deformation is obtained through eq. (1.6).

In finite element method, the local transformation gradient at point \mathbf{X} can be defined as the average of the infinitesimal gradient over a selected surface Ω [Allais et al., 1994]:

$$\mathbf{F}(\mathbf{X}) \approx \langle \mathbf{F} \rangle_{\Omega} = \frac{1}{|\Omega|} \int_{\Omega} \mathbf{F} dw \quad (1.9)$$

where $|\Omega|$ is the area of Ω . Using Green's theorem, this transformation gradient can be calculated from the displacement of its boundary (current position \mathbf{x} and its outgoing normal vector \mathbf{n} in reference configuration):

$$\mathbf{F}(\mathbf{X}) = \frac{1}{|\Omega|} \int_{\partial\Omega} \mathbf{x} \otimes \mathbf{n} ds \quad (1.10)$$

In practice, the contour $\partial\Omega$ is chosen as a polygonal path coinciding with measurement points nearby the evaluated position \mathbf{X} and the transformation is linearly interpolated between two neighbor positions. Based on these assumptions, the integral eq. (1.10) can be expressed discretely for each in-plane components of $\mathbf{F}(\mathbf{X})$:

$$F_{xx} = \langle F_{xx} \rangle_{\Omega} = \frac{1}{2|\Omega|} \sum_{n=1}^M x_n (Y_{n+1} - Y_{n-1}) \quad (1.11)$$

$$F_{xy} = \langle F_{xy} \rangle_{\Omega} = \frac{1}{2|\Omega|} \sum_{n=1}^M x_n (X_{n+1} - X_{n-1}) \quad (1.12)$$

$$F_{yx} = \langle F_{yx} \rangle_{\Omega} = \frac{1}{2|\Omega|} \sum_{n=1}^M y_n (Y_{n+1} - Y_{n-1}) \quad (1.13)$$

$$F_{yy} = \langle F_{yy} \rangle_{\Omega} = \frac{1}{2|\Omega|} \sum_{n=1}^M y_n (X_{n+1} - X_{n-1}) \quad (1.14)$$

where (x_n, y_n) are the coordinates of the n th contour point in the deformed configuration, and (X_n, Y_n) are the coordinates of the n th point in the reference configuration. Definition of the

integration schemes can be found in the reference of [Bornert et al., 2009]. In addition, the in-plane part of the deformation gradient can be decomposed into an in-plane rotation and a extension. The eigenvalues and eigenvectors of the latter lead to the two in-plane eigenvalues of the Green-Lagrange strain tensor (E_1 and E_2 with $E_2 > E_1$) and the angle θ between the principal direction E_2 and vertical axis of the reference image. The definition of these quantities is presented in Fig. 1.17.

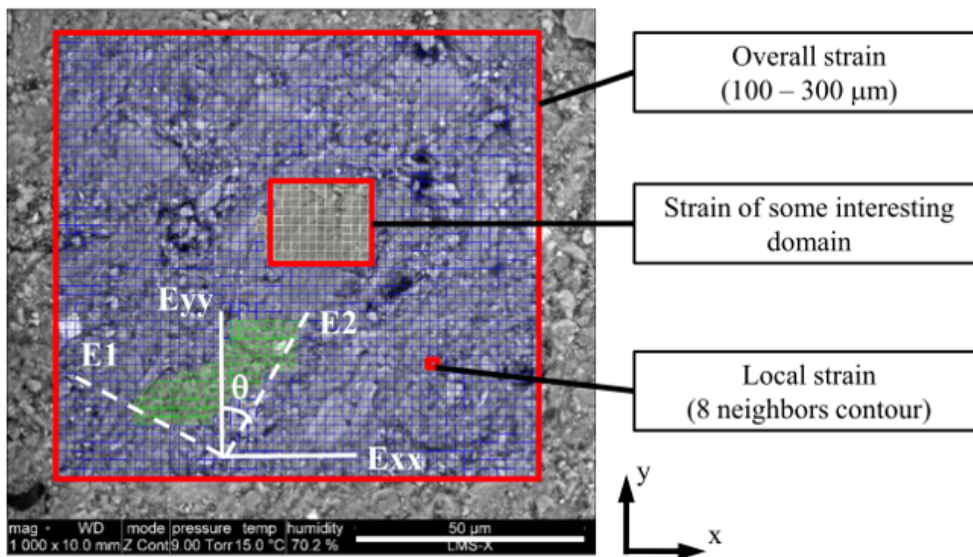


Figure 1.17 – Illustration of discrete measurement positions on an image associated with various averaging domains computed with Correlmanuv software (Image from [Wang, 2012]).

The local transformation and deformation can be calculated approximately surrounding the considered point within a selected integral scheme. Particularly, when Ω is selected to be the whole region of interest (ROI), the global strain of such region can also be evaluated. Furthermore, the average strain over a prescribed constituent of the heterogeneous material can also be evaluated from DIC technique [Allais et al., 1994].

1.3.2 Nanoindentation

This section is largely based on the work of [Oliver & Pharr \[1992\]](#). Nanoindentation was performed to evaluate the mechanical properties of human dentin at nano-scale. A tip was used to contact with the sample surface (see [Fig. 1.18](#)), while recording the force and displacement, which can be used to extract mechanical parameters. A Nano-indenter XP indentation system (MTS Corporation, USA) with a Berkovich indenter was used in this work.

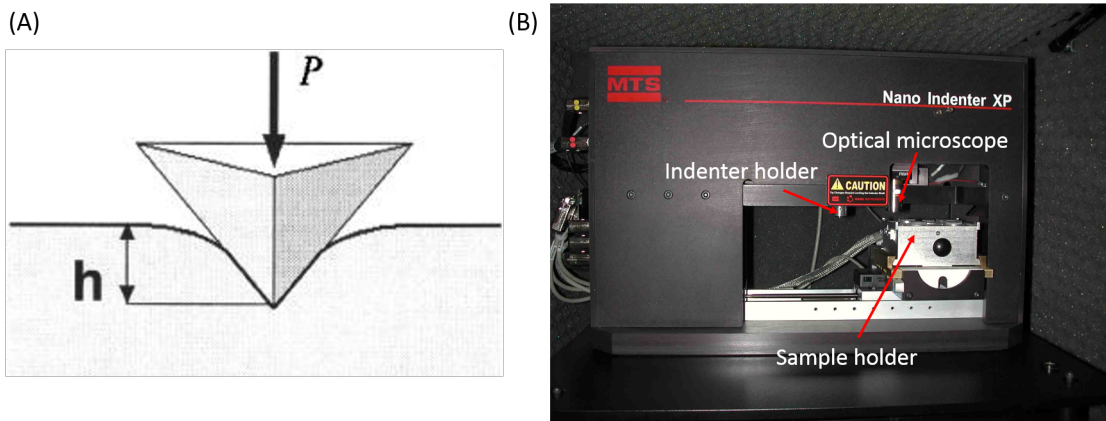


Figure 1.18 – (A) Illustration of the principle of indentation testing (Image from [[den Toonder et al., 2005](#)]). (B) Photo of the Nano-indenter XP instrument used in this work.

A typical load-displacement curve of an indentation test is shown in [fig. 1.19](#). The initial stage of the unloading part is considered as an elastic process. From this elastic unloading section, the modulus and hardness of the sample material can be extracted [[Oliver & Pharr, 1992](#)]: at the maximum load, the contact stiffness S is:

$$S = \frac{dP}{dh} = 2E^* \sqrt{\frac{A}{\pi}} \quad (1.15)$$

where A is the projection of the contact area and E^* is the reduced modulus which is a combination of the indenter mechanical parameters (E_i, ν_i) and the sample ones (E_s, ν_s):

$$\frac{1}{E^*} = \frac{1 - \nu_s^2}{E_s} + \frac{1 - \nu_i^2}{E_i} \quad (1.16)$$

The modulus of the diamond indenter tip is 1141GPa and its Poisson's ratio is 0.07 [Oliver & Pharr, 1992].

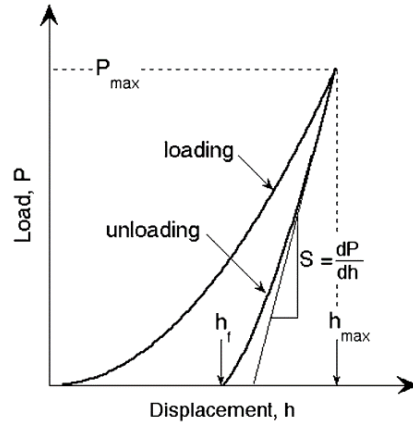


Figure 1.19 – A schematic representation of load displacement curve during a indentation process. Image was from the work of Oliver & Pharr [2004]

The indentation hardness can be defined as [Oliver & Pharr, 1992]:

$$H = \frac{P_{max}}{A} \quad (1.17)$$

where P_{max} is the maximum indentation load and A is the projected area of the indentation impression.

Continuous Stiffness Method (CSM)

The CSM measures continuously the applied contact force and the displacement of the indenter during loading part of the indentation. A small harmonic oscillation is added on the imposed force. The amplitude and phase of the corresponding displacements of the indenter were measured [Li & Bhushan, 2002; Odegard et al., 2005; Oliver & Pharr, 2004, 1992]. A illustration of the principle of CSM is showed in fig. 1.20.

The model of Oliver & Pharr [1992] gives the phase difference ϕ between force and dis-

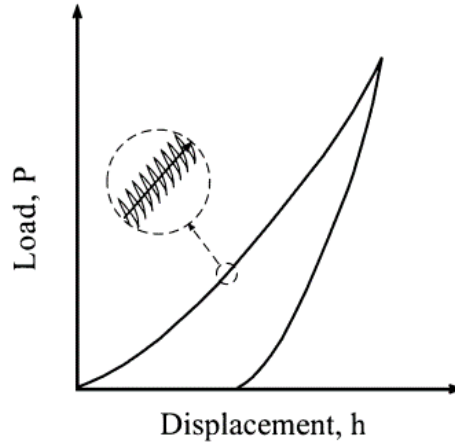


Figure 1.20 – Illustration of CSM loading cycles. A small oscillation is applied on top of the force consignment during the loading process (Image from [Li & Bhushan, 2002]).

placement signals and the ratio between the force amplitude and the displacement amplitude:

$$\left| \frac{P_a}{h_a(\omega)} \right| = \sqrt{[(S^{-1} - C_f)^{-1} + K_i - m\omega^2]^2 + \omega^2 D^2} \quad (1.18)$$

$$\tan(\phi) = \frac{\omega D}{(S^{-1} + C_f)^{-1} + K_i - m\omega^2} \quad (1.19)$$

where C_i is the compliance of the load frame (1.13 m/MN), K_i is the stiffness of the indenter frame (around 60 N/m) and D is the damping coefficient (around 54Ns/m). The contact stiffness is computed using the above equations. The reduce modulus is determined by [Oliver & Pharr, 2004]:

$$E^* = \frac{S}{2\beta} \sqrt{\frac{\pi}{A}} \quad (1.20)$$

where A is the projected contact area of the indenter, and β is the indenter shape factor (for Berkovich indenter, $\beta = 1.034$). Using eq. (1.16), the sample modulus can be determined.

The method based on unloading part of the displacement curve measures the mechanical properties of the material at small-scale. However, its accuracy of this method depends on the calibration process and the determination of the indent area, which can be affected by imperfection, for example the tip geometry. Unlike the unload method, the CSM method evaluates the mechanical properties in the loading part, and it offers several distinct advantages as re-

viewed by [Oliver & Pharr \[2004\]](#). First, it provides continuous results as a function of depth. Second, the time required for calibration and testing procedures is dramatically reduced because there is no need for multiple indentations or unloading. Third, at high frequencies, CSM avoids some complicated effects of time-dependent plasticity and thermal drift. Finally, the CSM allows one to measure stiffness changes and damping changes with the point of contact. However, the CSM is likely to be much more sensitive than the unload method to the near-surface forces, like adhesion between the tip and the sample.

1.4 Summary of the Bibliographic Review

Dentin is an inhomogeneous, hierarchical biological material. From the structural point of view, it is a three-phase porous composite material consisted of tubules (porous phase), peritubular dentin (inclusion phase) and intertubular dentin (matrix phase). These hierarchical structures strongly determine its mechanical properties.

At macro-scale, mechanical properties of dentin have been widely characterized using classical tensile, compression, bending and ultrasounds tests. According to the values reported, the elastic modulus of human dentin falls in a broad range, between 6.0 and 36.0GPa. At micro-scale, nanoindentation is one of the techniques used to characterize mechanically the different components of dentin (i.e. peritubular and intertubular dentin). According to the literature review, elastic moduli of peritubular and intertubular dentin are in the range of 30-42 GPa and 15-22 GPa, respectively.

A possible reason for Young's modulus variability is the small dimensions of the samples (typical size of a compression sample is around 2 – 3mm). At that scale, irregular specimen geometry modifies strongly the results of the mechanical tests and make it difficult to analyze. Thus, a well controlled sample preparation will be the first challenge of this thesis.

External environmental conditions, as air relative humidity, are important factors to determine the quality of a restoration. Information on the evaluation of dentin properties with

temperature or humidity will help to know the properties that should be possessed by restoration materials or implants.

The next chapter deals with the observation protocols we used on dentin, including micro-computed tomography (μ CT), histology, optical microscopy, confocal laser scanning microscopy (CLSM) and environmental scanning electron microscope (ESEM).

In chapter 3, an *in-situ* experimental setup that was built up in this thesis is presented. It combines a compression system with a control of the environment (relative humidity and temperature). The elastic mechanical properties of human dentin were assessed by uniaxial compression under different environmental conditions.

Chapter 4 focuses on the mechanical properties of dentin constituents at micro-scale. Nanoindentation tests were carried out in order to measure the elastic moduli for each components of dentin. Viscoelastic behavior was also investigated using the same approach.

Finally, a conclusion chapter summarizes the relevant results. The perspective of this work will be addressed by some numerical calculations. It will be related to the influence of the tubule's geometry and the implicit numerical model based on local structural information.

MULTI-SCALE OBSERVATION

Several protocols were used to observe dentin at different scales. At macro-scale, micro computed tomography (micro-CT) was used to have an overview of the tooth components. At micro-scale, techniques including histology, optical microscopy, environmental electronic scanning microscopy (ESEM) and confocal laser scanning microscopy (CLSM) were performed and are discussed. As conclusion, the advantages and disadvantages of each technique are reviewed.

2.1 Micro-CT Observations

Micro-CT is a technique that provides three-dimensional images of the internal structure of an object. Several radiographs of a sample are recorded at different angles, which are then used to reconstruct its inner structure in 3D. Conventional tomography uses the X-ray beam produced by high speed electron striking on a pure metal target. By moving the X-ray source, a sectional image of the sample in the focal plan can be made as in medical imaging. Consequently, structures in the focal plane appear sharper, while structures in other planes appear blurred. By modifying the direction and extent of the movement, operators can select different focal planes which contain the structures of interest [Langer, 2008].

A non-carious human third molar was used here. The tooth was obtained in the faculty of the dentistry of Paris Descartes University. The obtained molar was embedded in an Epoxy resin. A micro-CT (X50CT, NSI, at LMT of ENS Paris Saclay) was used to scan the specimen. The scanning parameters were set as: 14 watts, 150 kilovolts, 93 micro-amperes, $\times 10$ magnification, resulting in an image of $958 \times 1262 \times 872$ voxels with a voxel size of $15.3 \times 15.3 \times 15.3 \mu m^3$ shown on Fig. 2.1. Dentin, as the major part of tooth, occupies 74.1% (volume percentage) of the 2 solid phases (enamel and dentin).

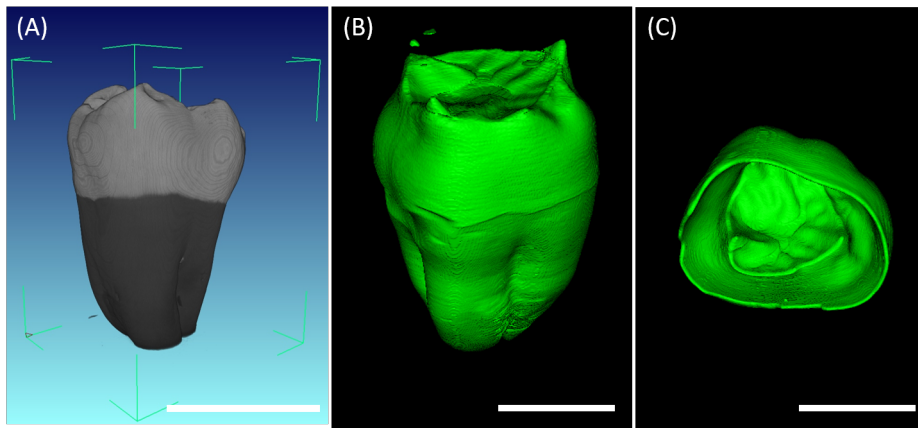


Figure 2.1 – Rendering the geometry of a human third molar. (A) whole tooth geometry, (B) 3D reconstruction of the dentin component. The pulp cavity inside the dentin which is not shown here. (C) 3D reconstruction of the enamel component of the molar. Scale bar: 10mm.

As shown in Fig. 2.2, it is easier to distinguish the enamel and the dentin due to their highly different mineral composition. The small density contrast and the small scale of contrast resolution, the microstructural parts of the dentin (tubule, peritubular dentin and intertubular dentin) make them hardly distinguishable with such technique.

2.2 Optical Microscope Observations

At micro-scale, dentin has three main geometrical features as presented in chapter 1: tubules (cylindrical pores), peritubular dentin (highly mineralized cuffs around tubules), intertubular dentin (the matrix surrounding the tubules and their peritubular collar).

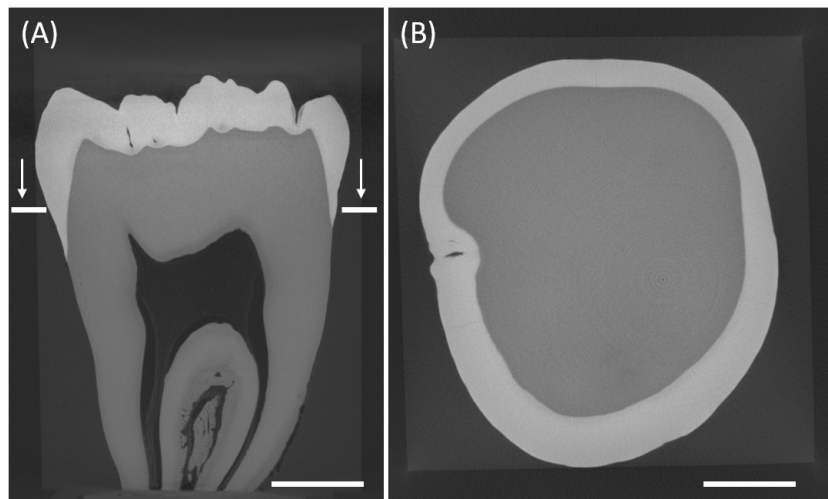


Figure 2.2 – Cross section views of a human molar. (A) Vertical cross section view. (B) Horizontal cross section view (indicated in A). Scale bar: $300\mu\text{m}$.

Traditional optical microscopy was performed to have views of human dentin microstructures. Non-carious human third molars were used here. The teeth were obtained in the faculty of dentistry of Paris Descartes University. Two modes of the optical microscope were used: reflective light microscopy and transmission light microscopy. It should be noted that the sample preparation for these two kinds of microscopy are quite different. For reflective light microscopy, a classical polishing protocol is the most suitable. Our sample was polished progressively by 80, 500, 800, 1200, 1400, 2000, 2400, 4000 grit SiC polishing papers under water irrigation, and finally turned to cloth polishing with $1\mu\text{m}$ diamond suspension liquid. For transmission light microscopy, the sample has to be fine enough in order to be sufficiently transparent. So, a histology cutting is performed. The tooth sample embedded into resin was cut into slices with a thickness around 1mm by a sectioning saw (Isomet low speed saw, BUEHLER Co., Lake Bluff, IL, USA). Then, the slices were pasted onto a glass chip and then polished under water irrigation (4000 grid SiC polishing papers), to reach near $100\mu\text{m}$ thickness.

Fig. 2.3 shows typical images of intact dentin from the reflective optical microscope (InfiniteFocus, Alicona Co., Raaba, Austria) and the transmission optical microscope (Axiovert, Zeiss Co., Germany). Unlike micro-CT, the dentin micro-structure can be well distinguished.

However, it is hard to extract quantitative values on the peritubular dentin with these techniques due to the too low contrast with intertubular dentin.

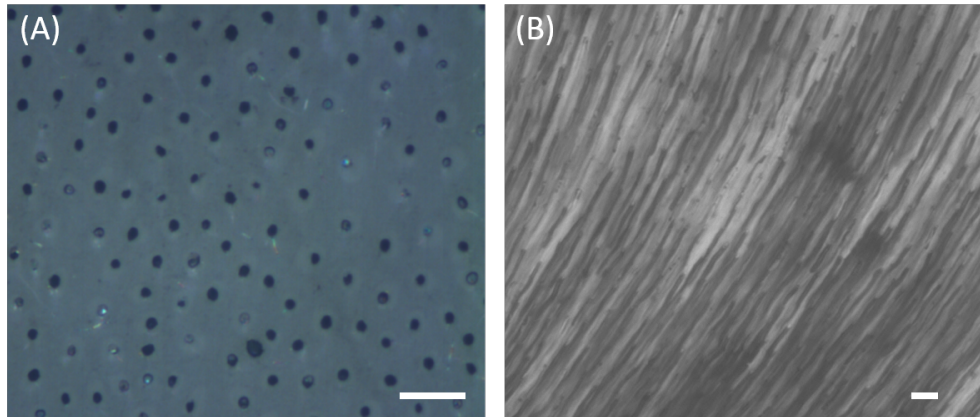


Figure 2.3 – Observation of intact dentin by optical microscopes: (A) top view from reflective light microscope and (B) lateral view from transmission light microscope. The samples were obtained from different teeth. The tubules can be distinguished by both techniques, whereas the peritubular dentin can hardly be distinguished. Scale bar: $10\mu\text{m}$.

The main advantages of optical microscopy are non-invasive, fast (as a consequence, large fields can be easily imaged) and easily available. Limitations of optical microscopy lie in three areas [Abramowitz & Davidson, 2007]. Firstly, optical microscope of both reflection and transmission light can only image dark or strongly refracting objects efficiently. Hence, tubules in dentin are clearly distinguished due to its porous structure, while the peritubular dentin can not be distinguished from the intertubular dentin. Secondly, although the resolution of an optical microscope can be down to $0.5\mu\text{m}$ (for green lighting) [Heintzmann & Ficiz, 2006], in practice, the resolution is not as good because of the lens quality, or the sample surface state (flatness, degree of reflection and absorption in different phases). Thirdly, light from points outside the focal plane can reduce the image quality and the resolution. Transmission light microscope avoids such disadvantage, but it requests a sufficient amount of transmitted light. This may be a problem of the preparation since the dentin slice needs to have very small thickness. Compared with reflection light microscopy, transmission light microscopy can be seen as a more destructive observation method.

An alternative imaging method is the electron microscopy. In the same way that light has a

wavelength, the movement of high-speed electrons also has a wavelength, which is thousands of times shorter than visible light. So electron microscopes are able to resolve really small objects: this theoretical resolution is approximately one-twentieth of one nanometer (10^{-9} m) [Inada et al., 2009]. This means that electron microscopes can be used to visualize viruses, molecules and even individual atoms and in our study can be used to image down to collagen fibers and hydroxyapatite crystallites.

2.3 ESEM Observation

Environmental scanning electron microscope (ESEM) is one type of scanning electron microscopes (SEM), which allows the presence of gas in the chamber. Unlike the conventional SEM, the ESEM obviates the need for special specimen preparation, in particular of a metallic coating for non-conducted samples. Also a specimen can be imaged at various temperatures and different humidity atmospheres. Thus, their original material characteristics can be better preserved. It is extremely useful for biological samples which are often non-conductive and very sensitive to the relative humidity.

The price to pay for the ESEM is the presence of the gas leads to scattering of the electrons that lead to a reduction of signal. The best current resolution of ESEM is around 5nm [Donald, 2003].

Non-carious human third molars were used in this study. A typical image by ESEM (Quanta 600, FEI Co., America) is shown in Fig. 2.4. The BSE (back scattering electron) mode was used in order to have maximal contrast for peritubular and intertubular dentins, taking advantage of their highly different mineral phases. The chamber pressure was set at 266Pa, and the temperature at 5°C, resulting to a relative humidity of 30%. The electron beam voltage was set at 10kV. Working distance was adjusted at 10mm. The maximum field of view is $340 \times 340 \mu m^2$. Each image was captured in 10min with a resolution of 2048×1768 pixels resulting a dimension of $0.17 \mu m$ for each pixel.

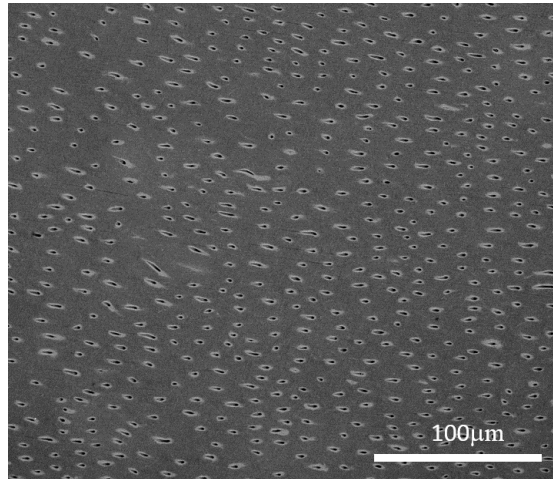


Figure 2.4 – Intact dentin observed by ESEM in BSE mode. ESEM parameters: pressure: $266Pa$, temperature: $5^{\circ}C$ (relative humidity: 30%), working distance: $10mm$ and HV: $10KV$. The tubules (black porous phase) and peritubular dentin (grey cuff around the tubules) were well distinguished.

The percentage of each different components of the dentin (peritubular and intertubular dentin) can be extracted with the open-source software *Fiji-ImageJ*. The different steps of the image treatment are shown in [Fig. 2.5](#). Firstly, the image was treated to have the area fraction of the tubules. A *rolling ball background subtraction* was applied on the original image. A local background value is determined for every pixel by averaging over a very large ball around the pixel. This value is hereafter subtracted from the original image, hopefully removing large spatial variations of the background intensities. The ball radius should be set to at least the size of the largest object that is not part of the background. Here, the ball radius was set as $6\mu m$. Then, the image was segmented into a binary image by the *auto-threshold operation*. The percentage area information of the tubules can then be obtained by the fraction of the pixels in black. Secondly, the fraction of peritubular dentin is determined. An *enhance local contrast operation* was applied on the image to enhance the peritubular dentin. This operation implements the method of contrast limited adaptive histogram equalization [[Zuiderveld, 1994](#)] for enhancing the local contrast of an image. Then, a *smoothing* operation was applied to reduce the noise from the background. Finally, an *auto-thresholding* operation was performed to obtain a binary image of the peritubular dentin. The area percentage information of the peritubular dentin can then be extracted from the fraction of the black pixels. In this

image (Fig. 2.4), the tubules occupies 2.89% (area fraction), while peritubular dentin 7.52%. The remaining part is intertubular dentin.

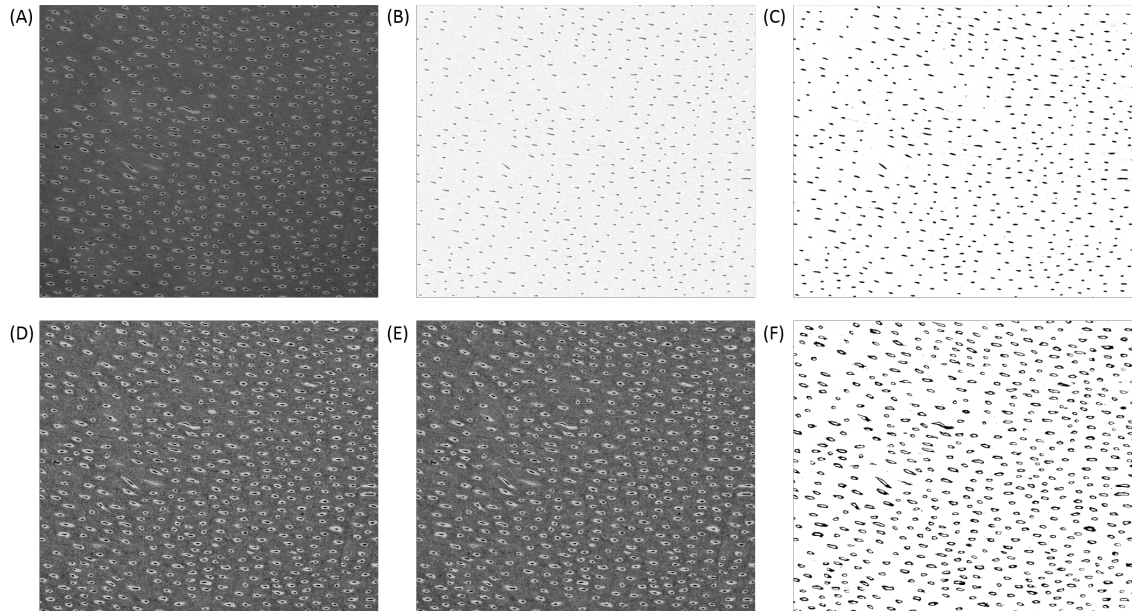


Figure 2.5 – The image treatment process by *ImageJ* to calculate the area fraction for tubule and peritubular dentin. (A) original image from ESEM. (B) *Subtract background operation* (Rolling ball radius: $6\mu\text{m}$). (C) *Auto-threshold* by algorithm *RenyiEntropy*. (D) Original image was treated by *Enhance local contrast operation* (Block-size: 127; Histogram: 256; Maximum: 3). (E) *Smooth operation* for (D). (F) *Auto-threshold* by algorithm *Minimum* for (E).

A dentin parallelepiped block extending from root dentin to crown dentin was prepared by a computer numerically controlled drilling machine (Lyra-GACD SA, France). The whole surface was imaged in ESEM by stitching a matrix of 11×4 images, using the image stitching process of the software *Fiji-ImageJ* [Preibisch et al., 2009]. The whole resulting view of the surface of this block is shown in Fig. 2.6, with the locations of the root dentin (left) and the DEJ (right).

An area of interest of $200 \times 200\mu\text{m}^2$ was used to determine the local area fraction of the different components of the dentin. This zone of interest was moved from root dentin to crown dentin to have the components evolution with position in the length. For each position, the area fractions were obtained from four images in the perpendicular (width) direction to estimate a standard deviation (SD). The distance along the length was normalized by the

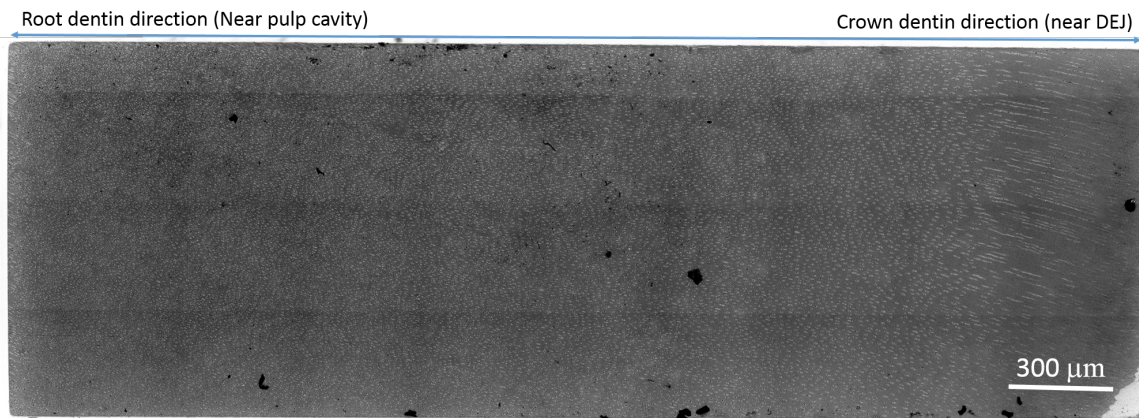


Figure 2.6 – The whole surface of the dentin parallelepipedic block extending from root dentin (left) to crown dentin (right). The image is the result of the stitching of 11×4 images ($320 \times 320 \mu\text{m}^2$). The stitching was done with *Fiji*.

sample length. **Fig. 2.7** shows the area fraction of each component of dentin estimated from root dentin near pulp cavity ($x = 0$) to the part near the DEJ ($x = 1$). Dentin is heterogeneous: from pulp cavity to DEJ, the area fraction of the tubules decreased from 7.73% (SD: 0.23%) to 3.08% (SD: 0.44%), and the area fraction of peritubular dentin decreased from 20.71% (SD: 4.33%) to 2.84% (SD: 2.07%). Four samples were also studied: the curves are shown in the appendix.A. The global statical results show that the area fraction of tubules in the root dentin near the pulp cavity was 9.39% (SD: 2.77%). The area fraction of the tubules near DEJ was 3.29% (SD: 0.98%). The area fraction of the peritubular dentin varied from 15.04% (SD: 6.04%) to 4.82% (SD: 1.58%) from root dentin to crown dentin part.

Marshall et al. [1997] reported that the area percentage of peritubular dentin in crown dentin varies from 60% near the pulp cavity to 3% at the DEJ, and that the percentage area of tubule varies from about 22% near the pulp to 1% at the DEJ. The values were deduced from measures at the two locations. They show a strong gradient in the peritubular dentin and tubules fraction from the pulp cavity to the DEJ. Our results by ESEM show a similar trend, with a less stiff gradient. In our experiment, the samples were drilled from the crown dentin to root dentin (see **Fig. 2.8**). The root dentin has narrow dimension and is near the pulp cavity. So, one side of the sample originating from the root dentin (see **Fig. 2.6**) was considered as the part near the pulp cavity. However, a change in the distance from the wall of the pulp

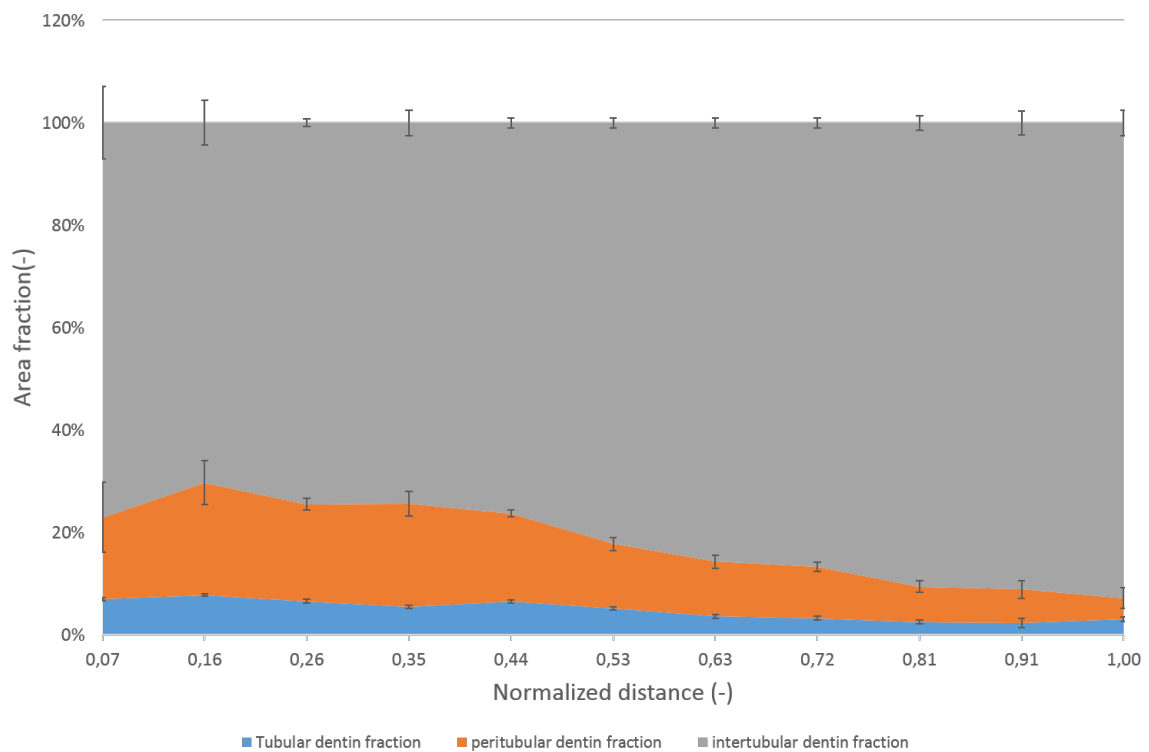


Figure 2.7 – The distributions of the area fraction for the three dentin components (sample AC2). Horizontal axis starts from the part near pulp cavity, and ends near DEJ.

cavity would lead to a significant modification of the results. It is also possible that, during aging, sclerosis of the dentin component would further modify the area fraction of the tubules and peritubular dentin inside the sample, which leads to the different values measured here.

ESEM provides a satisfactory resolution to distinguish the three dentin components. However, only 2D information can be extracted. In the next section, 3D visualization based on confocal microscope is explored.

2.4 Confocal Microscope Observations

Confocal microscopy is an optical imaging technique with increased resolution and contrast by collecting only the signal from the microscope's focal plane [Pawley & Masters, 1996]. Furthermore, apart from a better quality of image, it also allows three-dimensional

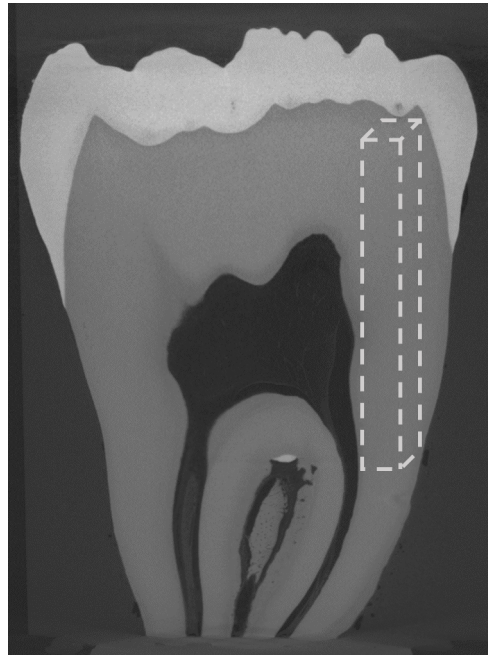


Figure 2.8 – Illustration of the sample location inside the tooth. The dash frame indicates the approximative location for the dentin samples.

visualization of a specimen area by assembling a stack of images taken along the vertical axis by moving the focal plan [Semwogerere & Weeks, 2005].

The majority of confocal microscopes are based on the collection of fluorescence signal from dyes (fluorophores) in the sample. Thus, in the study case here, only the tubule that have to be filled by a fluorescent solution can be imaged. The confocal microscope combines the ideas of point-by-point illumination of the specimen and rejection of out-of-focus light signal [Semwogerere & Weeks, 2005]. The point-by-point illumination brings a drawback: less emitted photons are collected in a given time. Hence, for an accurate measurement, it is essential to have a long enough time collection. This increases the time needed to create an image. One solution is to use a very high intensity light source to increase the number of the emitted photons per instant. Thus, a laser light source is often used with the additional benefit of possibilities of a wide range of wavelengths [Minsky, 1988]. The maximal lateral resolution is then around 180-160 nm, while the maximal resolution in the Z direction (depth) is of the order of 350-600 nm [Nasse et al., 2007], the objective lens determines both the magnification, the field of view, and the actual resolution.

Confocal microscope allows 3D visualization. But the penetration depth of the laser is rather limited in dentin. Because of the diffusion of the light by the tissue, the laser would result in defocussing when the focal plan is deep enough. For dentin tissue, the max depth of the imaging is around $50\mu\text{m}$.

The dentinal morphology has been widely studied in a two dimensional point of view [Mjor & Pindborg, 1973; Bertassoni et al., 2012; Nalla et al., 2005; Marshall et al., 2001; Balooch et al., 2004]. However, its 3D micro-structure seems to be less studied. Here, the confocal microscopy was proposed to fill this gap. It permits us to have the 3D visualization of the local dentinal porous micro-structure and Sto deduce some quantitative data (like the tubule diameter distribution and the local porosity).

3D visualization of dentinal porous structure by confocal microscope

In this section, the confocal microscopy was used to investigate the dentinal porous structure in a zone near the dentin enamel junction. In this area, Mjör & Nordahl [1996] has pointed out through a 2D SEM study that the associated tubules have a complex geometrical structure. Previous studies [Wang & Weiner, 1997; Imbeni et al., 2005] have showed that such a complex porous structure may play an important role to support the mechanical stresses during the mastication. The 3D visualization of the micro-structure in this area may then be helpful to understand its mechanical performance.

Materials and Methods

A. Sample preparation

A non-cariou human third molar was embedded with resin (Epofix). It was then cut into longitudinal sections with a sectioning saw (Presi Mecatome T210). The blade was 150mm in diameter with a constant rotating speed of 3200 t/min. The thickness of the blade was around $400\mu\text{m}$. The obtained sample section (longitudinal) was polished with 2000 grid paper, and then 4000 grid paper into a thickness around $200\mu\text{m}$. Then, the sample section were stained for 24 hours in a water solution with 0.02% in mass percentage of Rhodamine-B. And then,

the obtained tooth section was mounted in between glass slides in the same medium.

B. Observation

The observations were conducted in the LIPHY laboratory of the University Grenoble Alpes. All the imaging operations were conducted by Dr. Gourrier and Dr. Genthial. Firstly, the sample was observed by a classical optical microscope (Olympus IX 71, LIPHY, Genoble) to have an overview of the whole sample surface and the selected location (area near DEJ). Then, the sample was observed by a confocal microscope (TCS SP8, Leica TCS, LIPHY, Grenoble). The resolution of the obtained image was 2048×2048 pixels. The pixel size was $189.30nm \times 189.30nm$. The z distance between the stack images was 350nm. The resulting voxel size was $189.30nm \times 189.30nm \times 350nm$.

C. Image analysis and 3D Visualization

The open source software named *Fiji-ImageJ* (<http://imagej.nih.gov/ij/>) was used for image analysis and 3D visualization. For the image analysis, *rescale tool* was used to transfer the original voxel size ($189.30nm \times 189.30nm \times 350nm$) into isovoxel ($350nm \times 350nm \times 350nm$) if needed. *Particle analysis tool* was used to separate the tubules which can be identified by the threshold value. Then, each tubule can be extracted individually. The inertial axis of the tubule was also estimated through *Particle Analysis Tool*. The *thickness tool* estimated the local pore size distribution based on a maximal covering sphere algorithm, which defines the thickness at a point as the diameter of the greatest sphere that fits within the structure and which contains the point [Hildebrand & Rüeggsegger, 1997; Dougherty & Kunzelmann, 2007]. *volume viewer tool* and *3D viewer tool* were used for 3D visualization [Schmid et al., 2010], .

The scheme illustration of the image treatment protocol used in this study is shown in Fig. 2.9. A selected area of interest was cropped from the original confocal image stack. After operation of erosion and dilation, the image can then be processed by *particle analysis tool* to detect each tubules: the solid in Fig. 2.9 are the tubules. Each tubule is marked with an unique color. Through different thresholds, each tubule can be extracted. Erosion and

dilation treatments remove the branches along the tubules. Using the *particle analysis tool* in BoneJ plugin, the principal direction of inertia of that specific tubule can be calculated. Finally, the projection of the tubules along its principal inertia axis can be obtained. Three Y-shaped branches were isolated and analyzed to obtain the skeleton by applying the *analysis skeleton(2D/3D) tool*.

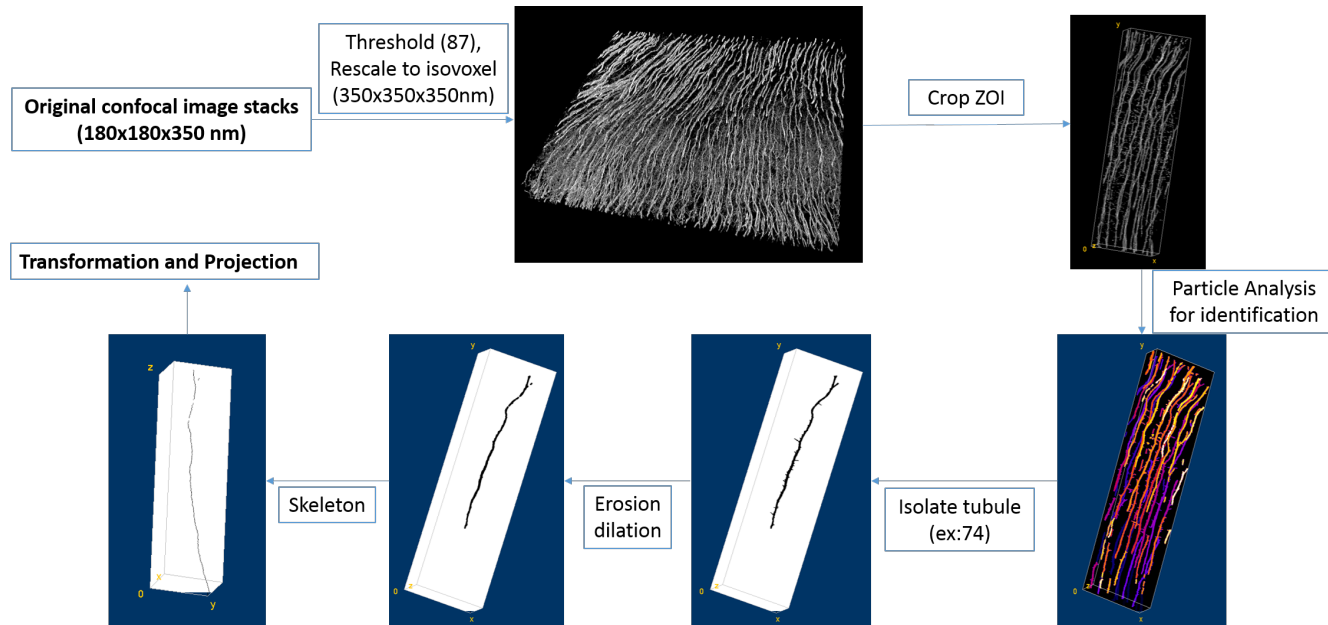


Figure 2.9 – Illustration of the image treatment and analysis protocol to analyze the shape of the tubules.

Results and Discussions

A. 3D visualization

The chosen area is indicated in Fig. 2.10: a zone near DEJ was selected. Images generated by the surface reflective photon signal (the way of conventional optical microscope, see Fig. 2.10.B) and the transmission signal (the way of the confocal microscope, see Fig. 2.10.C) were also recorded. Very limited details can be observed on common optical microscope images. The fine branches associated with the major tubules were almost invisible while they are visible on the transmission image.

Compared with 2D images, 3D visualization provides more details on the micro-structure

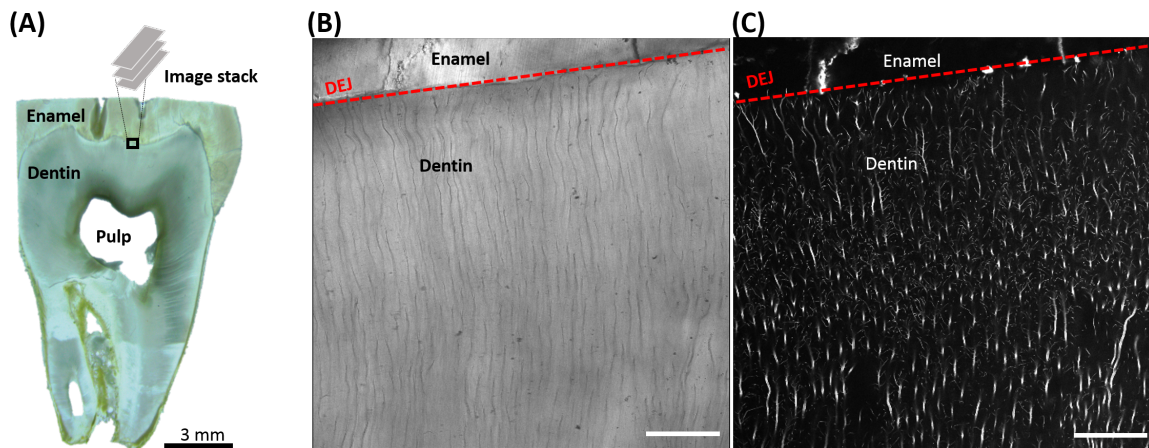


Figure 2.10 – (A) Location of the studied area (in a black rectangle) observed using a light optical microscope. Scale bar:3mm. (B) Image generated from the surface reflective photon as the common way of optical microscope. (C) Image generated from the transmission photon as the way of confocal microscope. In both images, the DEJ is the adjacent area between the dentin and enamel which is marked by a red dashed line. Scale bar:8 μm

of the tubule network (see Fig. 2.11). The tubules present a more complex structure than the one visible on the 2D images. A wave-like shape near DEJ was observed for the major tubule. At DEJ, the tubules show a complex tree structure, whereas on 2D images, only Y shaped structures were observed (see Fig. 2.10). A more detailed zooming figure is shown in Fig. 2.12. A finite element model for numerical calculations can be build from these images. An example of surface mesh is shown in Fig. 2.13.

It has been reported by Mjor & Pindborg [1973] that three types of branches (major, fine and microbranches) can be observed in human dentin. We observed here major and fine branches. Microbranches (25-200nm in diameter) are too small for the resolution of the confocal microscope. The fine branches associated with DEJ were found to have a Y-shape geometry in 2D study, while 3D images show a more complex shape. It may indicate that the initial behavior of the odontoblasts at DEJ has a synergistic effect for the formation of the dentin. For the main branches, Mjör & Nordahl [1996] pointed out a S-shape with a 2D study. 3D representation here presents a wavy shape, although not clearly structured.

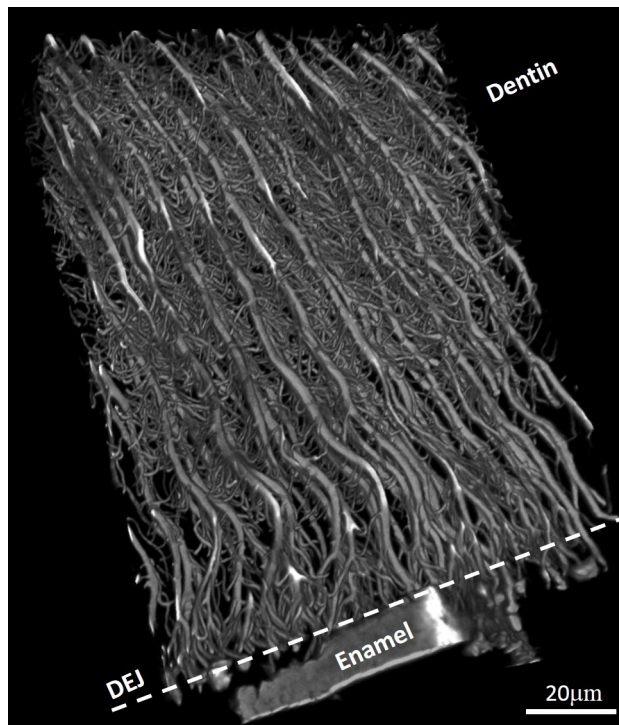


Figure 2.11 – Confocal 3D visualization of dentin tubules near DEJ. Enamel and dentin parts are indicated, their junction (DEJ) being marked by a dash line in the image.

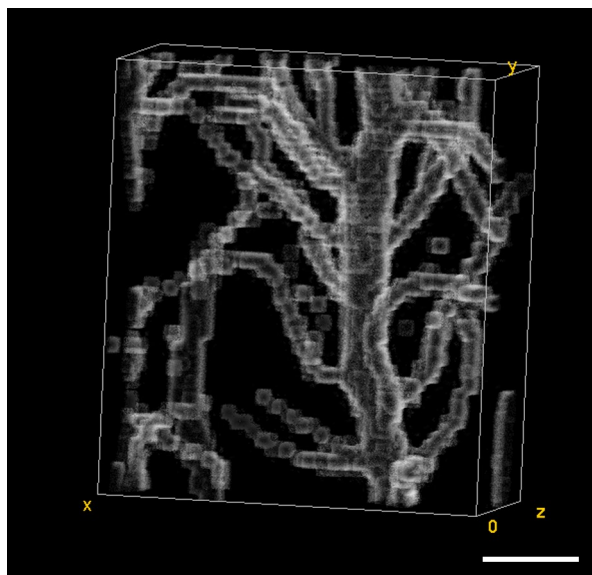


Figure 2.12 – The complex tree structure of the tubule geometry at DEJ. The top is adjacent with enamel part. Scale bar: 4 μm .

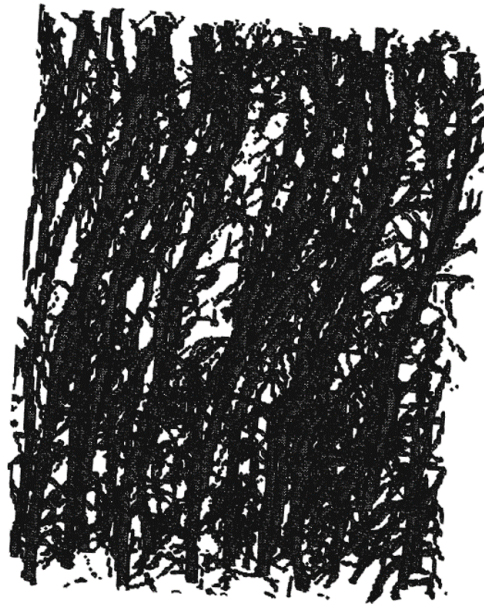


Figure 2.13 – Surface mesh with 752675 triangles for the complex tubule geometry.

B. Tubule diameter and porosity assessment

The diameter of the tubule can be estimated by a maximal covering sphere algorithm. The distribution of the local tubule diameter is plotted as a color map (see Fig. 2.14.A). The corresponding diameter was found to be a trimodal distribution with average values of $2\mu m$, $1.5\mu m$ and $0.75\mu m$, respectively (see Fig. 2.14.B). They correspond to the main and fine branches. As reported by Mjor & Pindborg [1973], three types of branches were reported according to their dimensions. Major branches (delta branchings) were found to be ranged in between 0.5 and $1.0\mu m$ in diameter. Fine branches were observed to be ranged in between 0.3 and $0.7\mu m$ in diameter, extending out from the tubules at roughly 45° . They are abundant in the area with low tubule density such as the zone near DEJ. The tubule size found here was larger than the one obtained from the previous SEM studies [Mjor & Pindborg, 1973] possibly due to the noise of the signal or the choice of threshold.

Local porosity was also estimated slice by slice based on the stack of confocal images (see Fig. 2.15). The signal intensity was decreasing with depth leading to a declining trend in the local porosity. The average results are summarized in Table 2.1. The obtained values turn out to be slightly larger than the previous studies [Pashley, 1989]. The signal noise and the

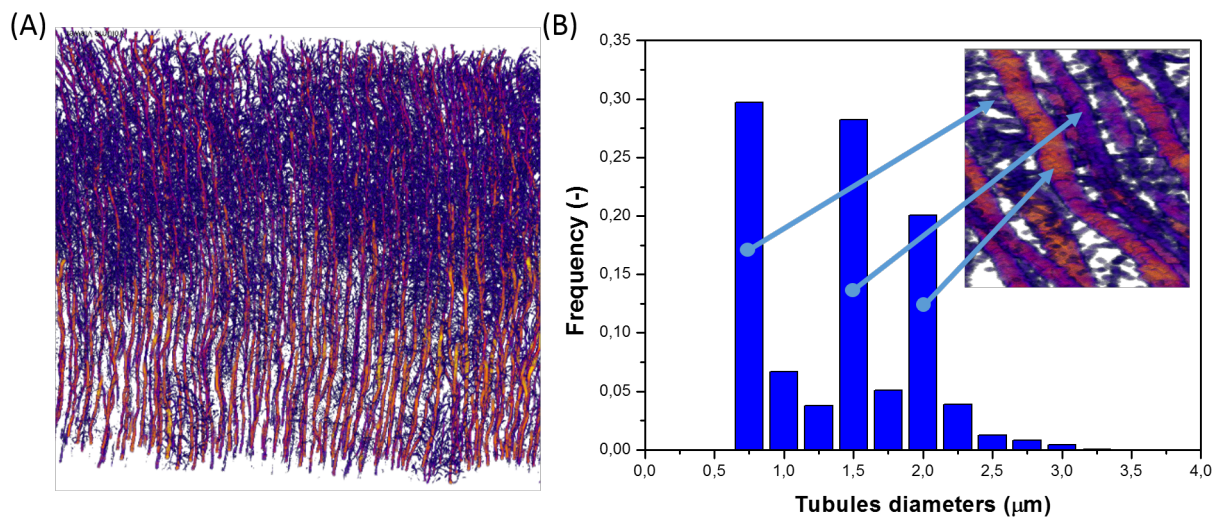


Figure 2.14 – (A) Color map representing the local diameter of the tubules near the DEJ. (B) Pore size distribution obtained using the Maximal Covering Sphere algorithm. A trimodal distribution was observed with average values of $2\mu\text{m}$, $1.5\mu\text{m}$ and $0.75\mu\text{m}$ associated with main and fine branches.

threshold are likely to be the reason for such a mismatch. It should be mentioned that the protocol based on the confocal microscope can be served as a new way to characterize the geometrical structures of dentin porous network. Better understanding the relationship between the macro-mechanical properties and the micro-structure of human dentin may provide some helpful suggestions for the case of filling restoration process.

Table 2.1 – Local porosity estimations for human dentin

Method	Location in dentin	Local porosity(S.D.)	Reference
Mercury Porosimetry	Whole dentin	4%	[Vennat et al., 2009]
SEM	Near DEJ	0.96%	[Pashley, 1989]
Confocal Microscope	Near DEJ	5.2%(0.4)	Here

Conclusion of CLSM observations

In this work, a new observation protocol based on confocal microscope was explored. As an example, 3D visualization of the complex dentin tubules micro-structure near DEJ was explored. It gives more details compared with classical 2D observations. In particular, the shape of the connection at DEJ shows a complex tree structure, while on 2D images, only

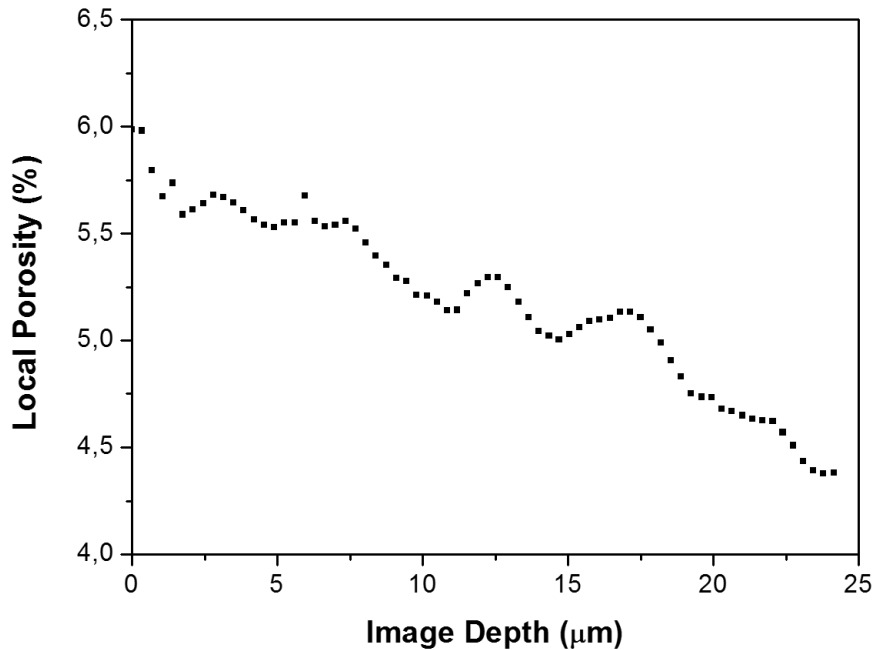


Figure 2.15 – Variation of the local porosity as a function of depth.

Y-shape structures were observed. Based on 3D visualization, first attempt was made to mesh the complex geometry with surface triangles. Besides, some quantitative data concerning about the local porosity distribution and the pore size distribution were also estimated. The results are slightly larger than the ones in the literature due to the lower signal to noise ratio and thresholding artifacts. The motivation of this work here was to present a new approach for 3D visualization and analysis of the complex dentin porous network. It may be useful to develop more realistic numerical model considering the complex geometrical feature of human dentin.

2.5 Summary of microstructure observation

Four techniques of observation were presented in this chapter. Their characteristics are summarized in [Table 2.2](#). Micro-CT provides the largest image field, allowing a 3D visualization of the whole tooth. However, the limited voxel resolution makes it impossible to

distinguish the detailed constituents of the dentin (tubules, peritubular dentin and intertubular dentin). Light optical microscope has a moderate image field size. It is the easiest way to have an overview of dentin at meso-scale with an intermediate resolution. The contrast is not sufficient to observe quantitatively the different dentin components but it gives the geometry of the sample in a short time. ESEM has its powerful environmental control ability with high resolution and contrast. Dentin can be observed without any special surface preparation, and its main structure components are visible. Based on fluorescence contrast, confocal microscopy is interesting for the 3D visualization and characterization of the dentin porous structure. The main limitation of this technique is the restriction of the image depth (roughly $40\mu m$). Tubules show more complicated tree-shapes near the DEJ, than "simply" Y-shaped deduced from 2D observations. Geometrical characteristics, like porosity and pore size distributions, can be evaluated, the high resolution enabling to visualize fine branches. Unfortunately, the morphological analysis is restricted to the porous network in which fluorescent fluid can penetrate.

Clearly, none of these observation techniques can be regarded as the best one. Each technique has its own advantages and drawbacks. For different questions, it will be always necessary to choose the proper one or combining different technologies. For instance, although the manual chosen threshold methods bring noise in the measurements by confocal microscope, it can be reduced through the use of SEM images. Other techniques are also available, which are not used here. For example, focused ion beam (FIB) combined with SEM (under BSE mode) can be used to realize the 3D visualization of the dentin structure with great details, as discussed in the perspective part.

Table 2.2 – Summary of the multiscale observation protocols for dentin

Methods	Image field dimension	Pixel (Voxel) Resolution	Environmental control	3D Visualization	Phase resolution†
Micro-CT	Whole tooth	$15.3\mu m \times 15.3\mu m \times 15.3\mu m$	×	✓	×
Optical microscopy‡	$990mm^2$	$0.2\mu m$ to $1mm$	×	×	×
ESEM	$340\mu m \times 340\mu m$	$1mm - 20nm$	✓	×	✓
Confocal microscopy	$387.50\mu m \times 387.50\mu m$	$189.30nm \times 189.30nm \times 350nm$	×	✓	×

Note: †optical microscope represents just light optical microscope here. ‡phase resolution means the ability to distinguish the dentine’s constituents (tubules, peritubular dentin and intertubular dentin).

MESO-SCALE MECHANICAL CHARACTERIZATION OF HUMAN DENTIN

External environmental conditions (i.e. temperature and relative humidity) play an important role in dentin mechanical behavior. During the general dental surgery, air relative humidity is always seen as a key factor for the bonding strength between the restoration material and the dentin substrate [Plasmans et al., 1993]. This bonding is also highly sensitive to environmental wetness, with a very low adhesion at high air relative humidity [Plasmans et al., 1993; Burrow et al., 1995; Plasmans et al., 1996]. Thus, understanding the influence of the environmental conditions on dentin is crucial to anticipate the properties requested for restorative materials.

Several studies have been made to characterize the thermal expansion coefficient of human dentin [Hengchang et al., 1989; Kishen & Asundi, 2001; Waters, 1979]. The oldest study [Hengchang et al., 1989] was conducted using a traditional dilatometer in distilled water. Over a range of 10 to 80 °C, a value of 10.56 (S.D.: 2.38) 10^{-6} (unit: $^{\circ}\text{C}^{-1}$) was measured. Such global measure doesn't provide any local information on the response of the different

components of the dentin micro-structure [Waters, 1979; Kinney et al., 2003]. Later on, local information was obtained through digital Moiré interferometry and thermo-mechanical analysis. Direct evidence of two major regions of thermal deformation were obtained: an expansion at low temperature (below 55 °C) and a contraction at higher temperatures. The thermal expansion coefficient was reported to depend not only on the temperature range but also on the location inside the tooth [Kishen & Asundi, 2001]. Recently, evidence from Forien et al. [2016] have shown that the water-assisted functional coupling between collagen fibrils and the hydroxyapatite inside the dentin sample would lead to a compressive strain after heat treatment.

This chapter aims to develop an integrated system which realizes a mechanical test under controlled temperature and relative humidity. The *in-situ* 2D deformations are measured with digital image correlation (DIC) techniques. Even if DIC is now quite common in biomechanics, reported applications of DIC to dental materials are rather limited [Wang et al., 2015; Zhang & Arola, 2004]. One limitation is that a careful calibration is needed to measure very small strains. So, we present first, an evaluation of the precision of the strain measurement for our integrated system. Compression results on dentin are then presented as a function of the environmental conditions. A resonant ultrasound spectroscopy (RUS) measurement was also done to measure the elastic modulus of the dentin sample in order to compare with the compression results.

3.1 Compression setup with Optical Imaging under Humidity and Temperature Control

In this section, a setup associating an optical imaging system and a compression machine is described. It is used to measure simultaneously the relative humidity, temperature and the strain. First, the experimental setup and the sample preparation are detailed. Errors on strain measurement were then quantified.

3.1.1 Experimental setup

The setup mainly consists of three parts: a mechanical loading device, an environmental control machine and an optical microscope (see Fig. 3.1). The mechanical loading device was installed inside an isolated, cuboid, environmental chamber made of polycarbonate. The environmental control machine (Secasi technologies, Germany) imposed the temperature and relative humidity inside the environmental chamber by continuous suction processes. One sensor (Rotronic, Swiss) was measuring continuously the temperature and relative humidity in the chamber. The whole experimental setup was located inside a room whose temperature was controlled by air conditioning. The testing system is illustrated in Fig. 3.2.

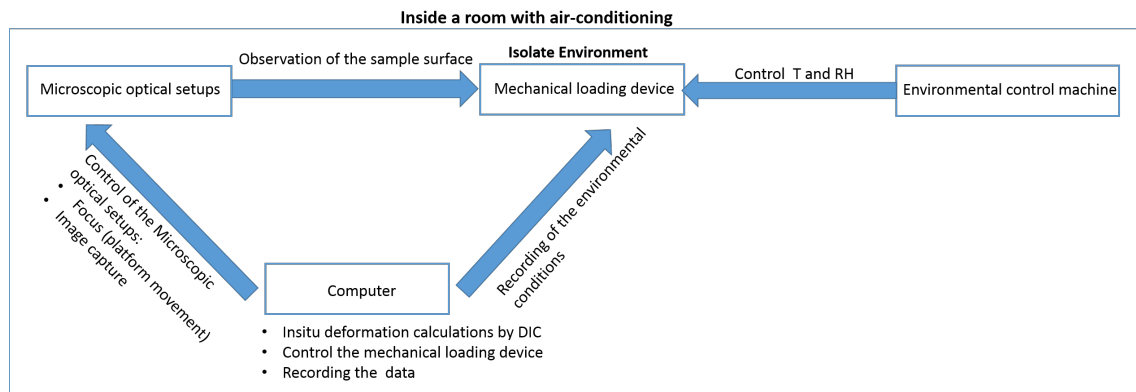


Figure 3.1 – The principle of the experimental setup. It consists three main parts: mechanical loading device, environmental control machine and optical microscope.

Similarly to [Gaucher et al., 2004; Yang et al., 2012], the optical microscope is made of a 8 Megapixels CCD camera (AVT GX3300) combined to a mitutoyo objective lens ($\times 5$ or $\times 10$ of magnification). With this optical combination, the observed object area is around $1.5 \times 1.5 \text{ mm}^2$. The image is formed of $3296(h) \times 2472(v)$ pixels, which are squares of $5.5 \mu\text{m}$, associated in the real image to sizes of 1.1 and $0.55 \mu\text{m}$ for the 2 objectives respectively. The respective fields of view are then of $3.625 \times 2.719 \text{ mm}^2$ and $1.812 \times 1.359 \text{ mm}^2$. Due to the small depth of field of the objectives, ($3.5 \mu\text{m}$ for objective $\times 10$), the camera has been mounted on a servo-controlled X–Y–Z translation stage. It allows the automatic adjustment of the Z position (normal to sample surface) so that the object is at the focus of the objective

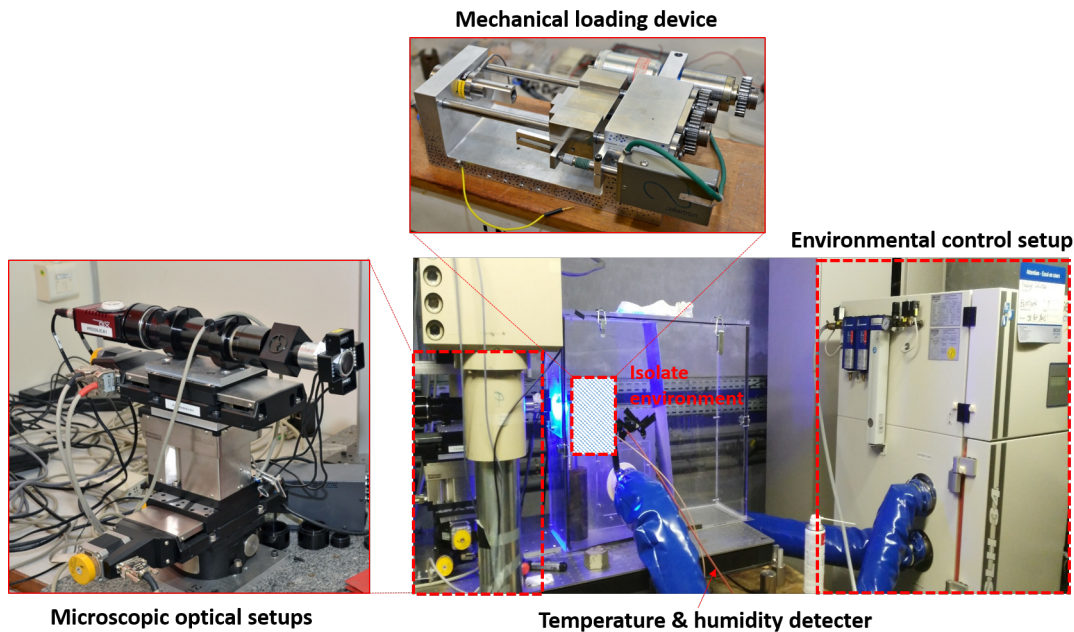


Figure 3.2 – The test system consists of three parts: microscopic optical setup for image acquisition, mechanical loading device installed inside an isolate environment and an environmental controlling setup. The sample was installed in the compression setup. Its speckled face was faced to the camera. Courtesy (and copyright) of the two bottom images to P. Lavialle (Ecole Polytechnique).

(using a contrast maximization algorithm). X and Y motions can be used to observe several juxtaposed zones and stitch them, or to follow a given region during an experiment, with an accuracy around $3\mu m$. An additional motorized rotation stage is used to align the X–Y translation stage CCD with the surface of the sample so that the focus is preserved on all the surface of the sample. The stages and the Sylvia control software (control stages, strain measurements) were developed by H. Gharbi, with the help of V. de Greef (LMS - Ecole Polytechnique, CNRS).

3.1.2 Sample preparation

For mechanical tests, the sample geometry is one of the most key factors [Davis, 2004]. The mechanical parameters such as the elastic modulus are determined by the stress and strain measurement within the elastic range of specimen. Compression test is supposed to apply an

3.1. Compression setup with Optical Imaging under Humidity and Temperature Control

uniaxial stress onto the sample; if the sample geometry is irregular, the stress state would not be really uniaxial and the strains would be heterogeneous. This would lead to an incorrect result or a too complex analysis. Thus, the sample preparation should be considered as one of the most important steps in the mechanical tests.

Ten crown dentinal parallelepipeds were prepared to be used as compression samples. To do so, intact human third molars were embedded into epoxy resin. Then, the overall shape of the dentinal parallelepiped beams was obtained using computer numerically controlled milling prototype (Lyra-GACD SA, France). From this rough shape, the final geometry was obtained by careful polishing. The sample was first mounted in a sample holder fixed by two screws (see Fig. 3.3, left). The whole sample holder was then installed under a piston shaped device: the plunger of the piston device applies a force on the sample holder in order to make a controlled, flat surface (see Fig. 3.3). Rotating the sample allows to have four long faces polished the same way, while being properly parallel. For the 2 small faces, the samples were fixed in the piston by pressing the large faces on a carefully built sample holder (see Fig. 3.3, right). It allows to polish these 2 faces parallel to each other and perpendicular to the other ones. For all the surfaces of the specimen, the polishing was done with SiC papers from 800 to 2000 grit under water irrigation, followed by a final cloth polishing with $1\mu\text{m}$ diamond suspension liquid. Between each polishing step, the sample was washed in an ultrasonic cleaner for 3-5 min to remove the debris. The dimension of the parallelepiped was measured (around $3\text{mm} \times 1\text{mm} \times 1\text{mm}$, see Fig. 3.4). The samples were observed with an optical microscope (Keyence at LMS of Ecole Polytechnique) to control their shapes. The angle between two parallel edges was validated to be less than 4 degrees. The dimensions of the ten samples are summarized in Table 3.1.

3.1.3 Sample observation

Dentin consists of tubules, peritubular dentin (PD) and intertubular dentin (ID). PD is more mineralized than IT, so the two can be well distinguished in ESEM using the BSE mode.

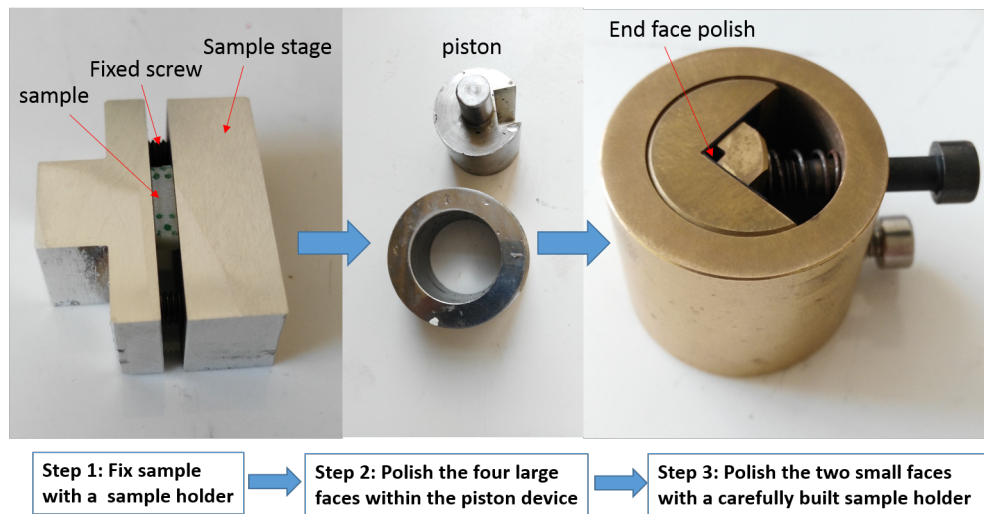


Figure 3.3 – Photos of the sample preparation setups. The sample was mounted in a sample holder fixed by two screws (left image). The whole sample holder was installed under a piston shaped device (image in the middle) for polishing four large face of the sample. The last two small faces were polished by fixing the sample on a carefully built holder (the right one).

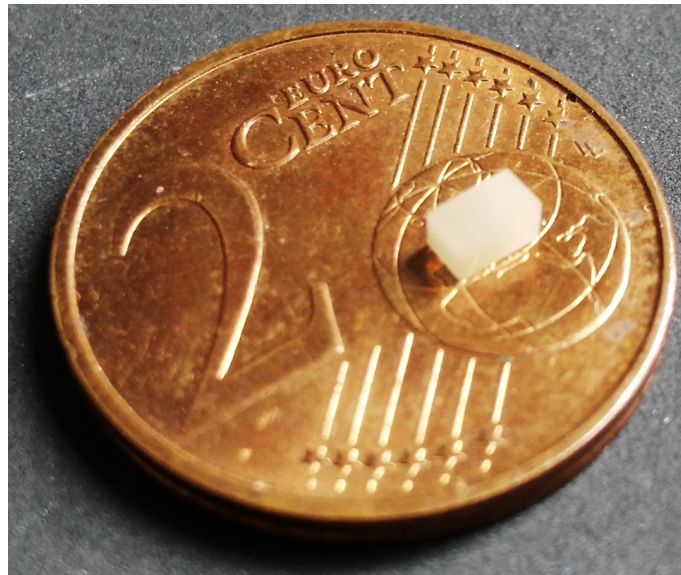


Figure 3.4 – Photo of the dentin specimen AC1.

3.1. Compression setup with Optical Imaging under Humidity and Temperature Control

Table 3.1 – Summary of the dimensions of the ten dentin samples

Sample	Dimension(mm)	Mass (mg)	Density(mg/mm³)
AC1	0.95 × 1.16 × 3.05	6.86	2.04
AC2	0.77 × 0.66 × 3.06	3.35	2.18
AC3	0.65 × 0.79 × 2.58	2.83	2.13
AC4	1.00 × 0.88 × 1.99	3.66	2.10
AC5	1.36 × 1.28 × 2.88	10.56	2.10
AC6	1.05 × 1.07 × 2.19	5.30	2.16
AC7	1.10 × 0.78 × 2.47	4.51	2.12
AC8	0.95 × 1.14 × 2.14	4.83	2.10
AC9	1.42 × 1.40 × 2.02	8.56	2.12
AC10	1.00 × 0.90 × 3.03	5.86	2.15

Three perpendicular faces of the samples were observed using the same protocol as the one presented in section 2.3. Images for sample AC1 are shown on [Fig. 3.5](#). Images of the other samples can be found in the appendix.A.

Due to the insufficient contrast of the original sample (pure white for DIC), ink speckles were painted onto the face which will be used for DIC analysis. The ink markers have an average diameter around $12\mu m$ with a standard deviation of $2.6\mu m$ (see [Fig. 3.6](#) for AC1).

3.1.4 Error estimation

Method

In the images, grey levels reflect numbers of discrete and independent signals received by detectors during integration time. As such, they carry an intrinsic noise. The image noise caused by the camera was measured on a sample without any deformation. When the isolate system reached the stable state at the selected conditions (temperature and relative humidity) for at least 15 minutes, the measured deformations were regarded as noise. The temperature was kept at room temperature (25 °C). The deformations were estimated with 20 images for two objectives ($\times 5$ and $\times 10$) under different humidities using the auto-focus process of the optical microscope. A mesh frame (number of elements are 7×7) was defined with an element

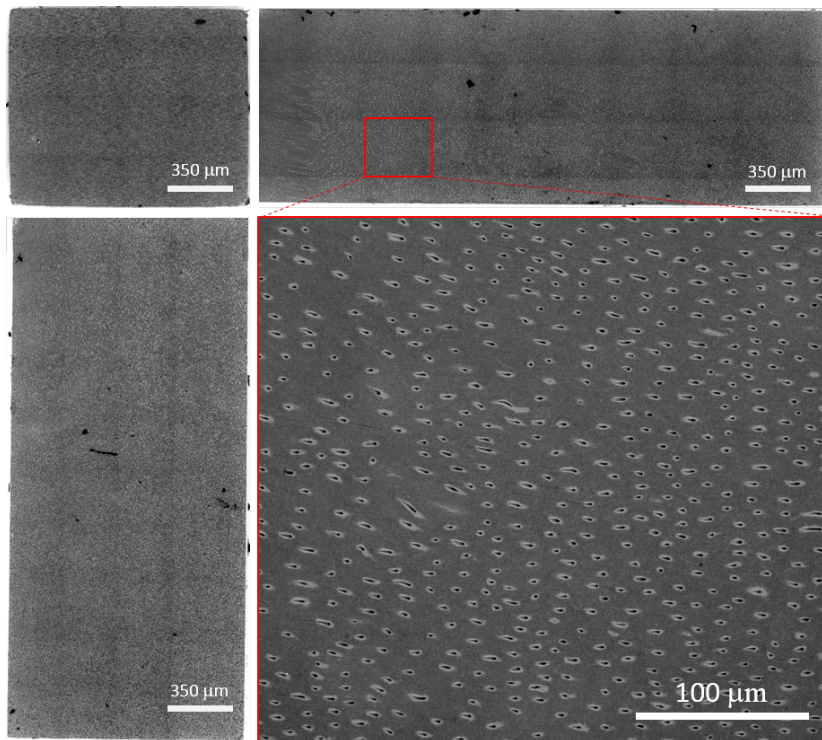


Figure 3.5 – ESEM stitching images of three perpendicular faces for the sample AC1. The image at down right corner is a zoom on a part of the top right image. Tubules appear in black, PD in white and ID in grey.

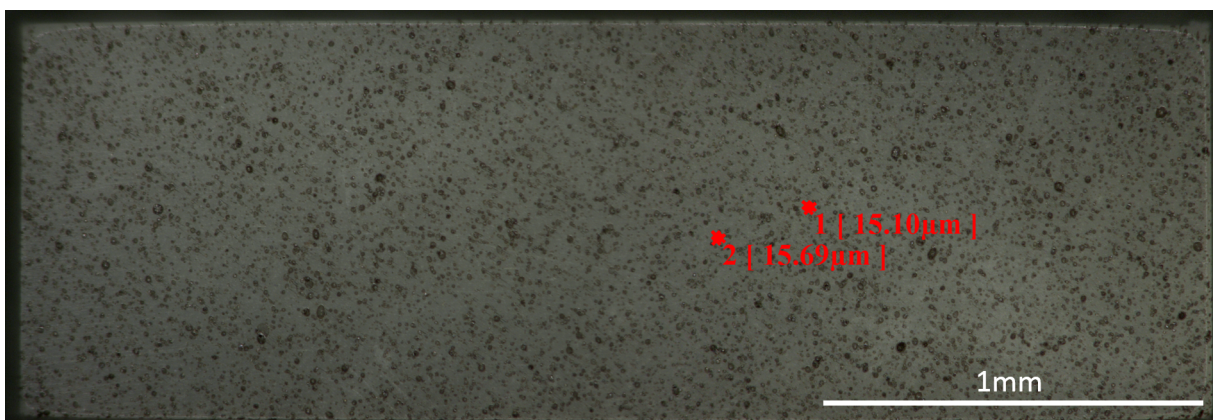


Figure 3.6 – Optical image (Keyence) of the surface with ink speckles (sample AC1).

3.1. Compression setup with Optical Imaging under Humidity and Temperature Control

size of 150 pixel \times 150 pixel in the center of the image. During the image acquisition, the deformation (ϵ_{xx} , ϵ_{yy} , ϵ_{xy}) and the rigid-body rotation angle between the principal direction and vertical axis of the reference image (R_{yy}) were calculated in real-time.

Apart from image noise, another error is induced by the inaccurate sub-pixel image reconstruction by imperfect grey level interpolation in the DIC technique [Choi & Shah, 1997; Schreier et al., 2000; Wang et al., 2014]. The correlation coefficient and/or its gradient must be assessed at non-integer locations to obtain sub-pixel accuracy, which requires interpolation on grey levels and grey level derivatives. The bias between the reconstructed intensity pattern (by interpolation) and the real intensity pattern is the origin of the translation error.

The translation error was also evaluated at selected environmental conditions (room temperature, relative humidity: 55%). A translation of the camera was conducted in the three directions: X and Y directions (horizontal and vertical directions of the image) and Z direction (camera focus direction). For translation in X and Y, images were taken every $1\mu m$ between $-20\mu m$ to $20\mu m$. For Z direction translation, images were taken every $0.1\mu m$ between $-10\mu m$ to $10\mu m$. Errors due to motion in the Z direction does not belong to the translation error, but to out-of-focus errors. The first image (the position 0) was set as the reference image.

Results

Fig. 3.7 shows the image noise on the deformation and rotation for two very different humidities (55% and 88%). The humidity did not seem to affect the noise level: the deformation stay at the level of micro-epsilon $\mu\epsilon$ ($1\mu\epsilon$ means 1×10^{-6}). The results are summarized in Table 3.2. For objective $\times 10$, the noise error of the strain ϵ_{xx} ranged from $-20\mu\epsilon$ to $20\mu\epsilon$ with an average value of -1.36×10^{-21} (S.D. 8.08×10^{-6}) and -3.90×10^{-21} (S.D. 1.39×10^{-5}) for two humidities, respectively. The noise error of the strain ϵ_{yy} ranged from $-15\mu\epsilon$ to $13\mu\epsilon$ with an average value of -2.71×10^{-21} (S.D. 6.95×10^{-6}) and -8.67×10^{-20} (S.D. 6.24×10^{-6}) for the two humidities, respectively. The measured strain ϵ_{xy} ranged from $-15\mu\epsilon$ to $15\mu\epsilon$ with an average value of 6.35×10^{-22} (S.D. 2.84×10^{-6}) and -3.79×10^{-20} (S.D. 7.92×10^{-6})

for the two humidities, respectively. The rotation angle has a noise error between -10×10^{-4} to 7×10^{-4} degree.

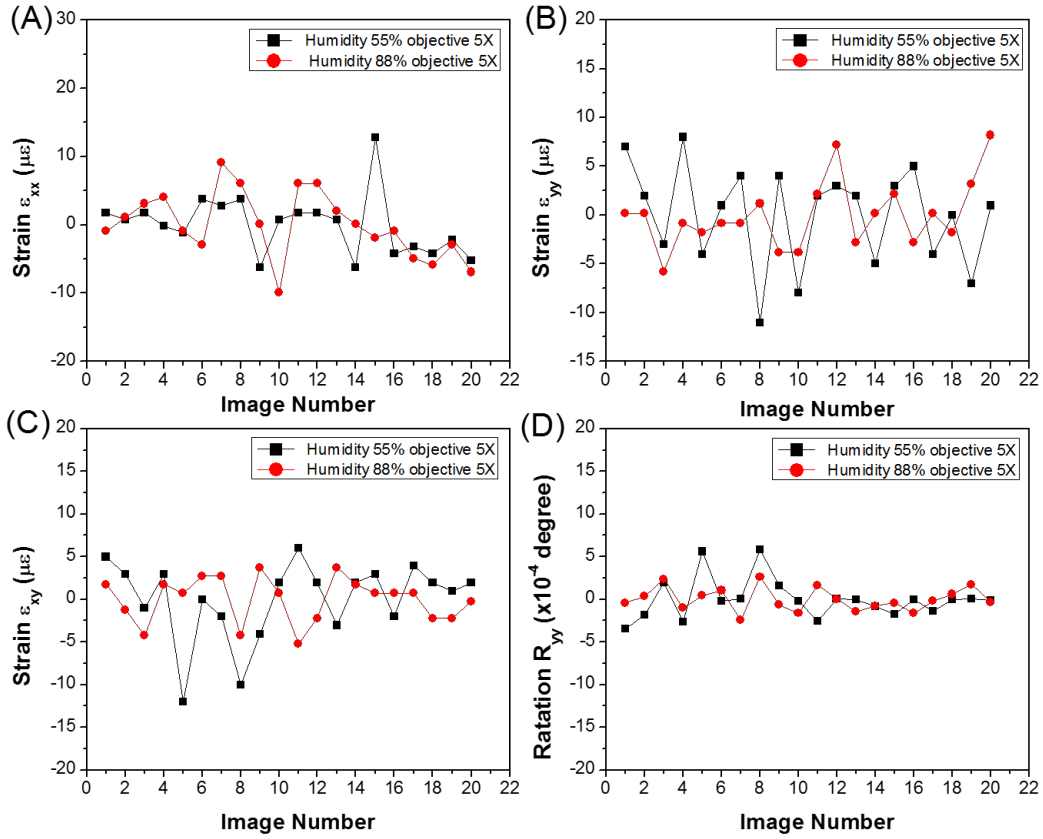


Figure 3.7 – Image noise measurement for objective 5x under relative humidity of 55% and 88%: (A) ϵ_{xx} (B) ϵ_{yy} (C) ϵ_{xy} (D) R_{yy}

Table 3.2 – Image noise measured under different humidities for the two objectives.

Objective	Relative humidity	ϵ_{xx} (SD)	ϵ_{yy} (SD)	ϵ_{xy} (SD)	R_{yy} (SD)
×10	20%	-1.36×10^{-21} (8.08 × 10 ⁻⁶)	-2.71×10^{-21} (6.95 × 10 ⁻⁶)	6.35×10^{-22} (2.84 × 10 ⁻⁶)	7.61×10^{-4} (1.75 × 10 ⁻⁴)
	90%	-3.90×10^{-21} (1.39 × 10 ⁻⁵)	-8.67×10^{-20} (6.24 × 10 ⁻⁶)	-3.79×10^{-20} (7.92 × 10 ⁻⁶)	0.14×10^{-4} (0.04 × 10 ⁻⁴)
×5	55%	-2.31×10^{-21} (4.42 × 10 ⁻⁶)	-8.67×10^{-20} (5.14 × 10 ⁻⁶)	-4.74×10^{-21} (4.61 × 10 ⁻⁶)	8.67×10^{-5} (2.37 × 10 ⁻⁴)
	88%	3.90×10^{-19} (4.89 × 10 ⁻⁶)	-2.22×10^{-22} (3.46 × 10 ⁻⁶)	-8.67×10^{-20} (2.67 × 10 ⁻⁶)	1.11×10^{-4} (1.38 × 10 ⁻⁴)

Fig. 3.8 shows the X and Y translation errors. The measured errors are summarized in Table 3.3. The measured ϵ_{xx} , ϵ_{yy} and ϵ_{xy} are the same for translations in X or Y. For translation in direction X, the measured strains ranged between $-44\mu\epsilon$ and $84\mu\epsilon$. The resulting average values of the translation errors were $1.95\mu\epsilon$ (S.D. 26.49) for ϵ_{xx} , $16.88\mu\epsilon$ (S.D.22.08) for ϵ_{yy} and $2.48\mu\epsilon$ (S.D. 20.96) for ϵ_{xy} , respectively. For translation in direction Y, the measured strains ranged between -82 and $59\mu\epsilon$. The resulting average values of the translation errors were $-27.23\mu\epsilon$ (S.D. 28.41) for ϵ_{xx} , $3\mu\epsilon$ (S.D. 30.69) for ϵ_{yy} and $-4.58\mu\epsilon$ (S.D. 25.61) for ϵ_{xy} , respectively.

Table 3.3 – Camera translation error estimations (values inside the brackets: standard deviation)

	ϵ_{xx} ($\mu\epsilon$)	ϵ_{yy} ($\mu\epsilon$)	ϵ_{xy} ($\mu\epsilon$)
Translation in X ($\times 10$)	1.95 (26.49)	16.88 (22.08)	2.48 (20.96)
Translation in Y ($\times 10$)	-27.23 (28.41)	3 (30.69)	-4.58 (25.61)
Translation in X ($\times 5$)	35.54 (17.04)	15.81 (12.05)	2.39 (31.52)
Translation in Y ($\times 5$)	-29.96 (42.25)	22.80 (68.0)	-2.03 (32.17)

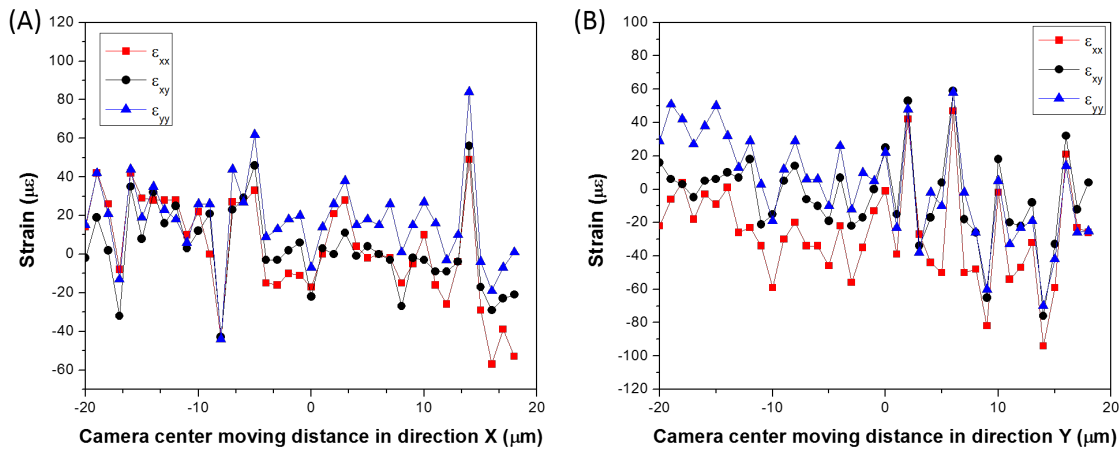


Figure 3.8 – Camera translation error estimations for objective $\times 10$. (A) translation in direction X; (B) translation in direction Y

The measured strains are strongly influenced by the focal distance (see Fig. 3.9). Z translation is different from the other two types of measurements. It is associated with an out-of-focus alteration of the image, which leads to an artificial dilatation. A camera closer from the

3.1. Compression setup with Optical Imaging under Humidity and Temperature Control

sample would cause a dilatation effect. In the focal length, the dilatation is proportional to δZ . Out of the focal length, the blur and optical aberration lead to a more complex response. If the focal distance was within the field of depth (from $-1\mu m$ to $1\mu m$), the measured strain had a relative low translation error, which ranged from $-50\mu\epsilon$ to $50\mu\epsilon$. However, if the focal distance was not controlled in that range, the resulting strains would contain large error. This proves the importance of the auto-focus process for the small scale DIC deformation measurement.

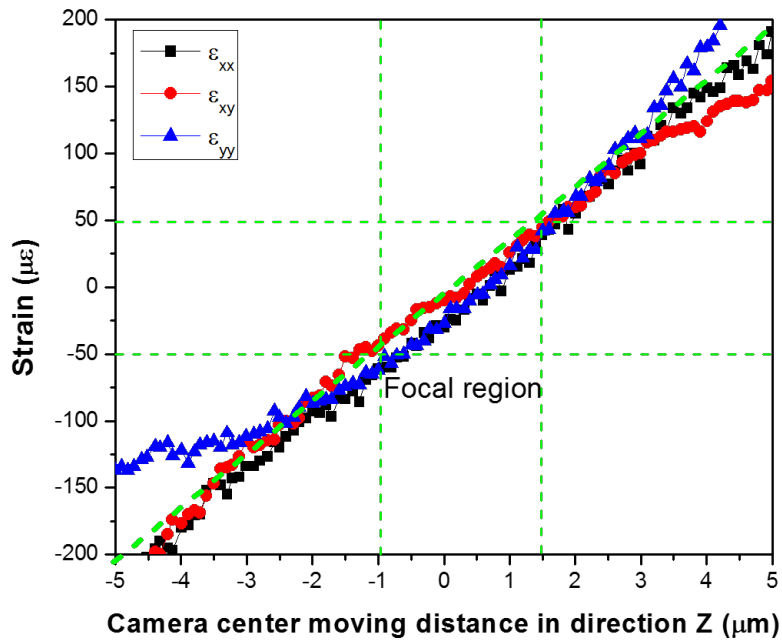


Figure 3.9 – Out-of-focus error due to the camera translation in Z direction (focus direction). The solid green line indicates the expected response

3.2 In-situ Compression Test within the setup

3.2.1 Compression test

The uniaxial compression setup was used to measure the mechanical properties of dentin for three different relative humidity (55%, 75% and 90%). The temperature was kept as room temperature (around 25 °C). The force applied was kept under 80N so that the samples remained within the range of elastic behavior. So, a load cell of 100N was selected for force measurement. The displacement speed of the crosshead was chosen as $1\mu m/s$. The associated strain rate should be around $3 \times 10^{-4} s^{-1}$ to $5 \times 10^{-4} s^{-1}$ for perfectly stiff device. The camera system (objective $\times 10$) was capturing one image every 5 seconds. The deformations were calculated with a mesh frame of 7 by 7 joined elements with an element size of 150 pixel \times 150 pixel.

Results from compression

The stress and strain curve of sample AC8 is shown on [Fig. 3.10](#). The nonlinear shape of the curve is likely due to the non-perfect shape of the specimen or the non-perfect parallelism of the crossheads. Elastic modulus was derived both from the load part and unload part of the stress-strain curve by a standard linear fit. We measured respectively 17.46 GPa (standard error: 0.36) and 19.66 GPa (standard error: 0.50) for sample AC8. The stress-strain curves for all samples can be found in appendix.B, and the results are summarized in [Table 3.4](#). The average moduli were 16.66 (SD:5.06) GPa and 17.78 (SD:5.04) GPa for load and unload parts of the stress-strain curve. These values are in accordance with the values reported by [Peyton et al. \[1952\]](#) but also by [Jantararat et al. \[2002\]](#) for the same range of strain rates. It should be mentioned that larger strain rates would lead to an increase of the measured elastic modulus.

Poisson's ratio (defined as $-\frac{\epsilon_{xx}}{\epsilon_{yy}}$) was plotted against the deformation in [Fig. 3.11](#) for sample AC8. Due to the initial non-linear response, Poisson's ratio measurement starts with a non-significant region before reaching a stable value of 0.31 ± 0.02 .

Table 3.4 – Summary of the compression results

Sample	Relative Humidity (%)	Temperature (°C)	Modulus deduced from load (GPa)	Modulus deduced from unload (GPa)	Poisson's ratio (-)
AC1	55.02 (0.10)	29.60 (0.18)	20.86	21.11	0.31 (0.02)
AC2	56.00 (0.06)	24.30 (0.20)	21.11	21.60	0.29 (0.01)
AC3	55.62 (0.11)	25.72 (0.28)	18.66	19.93	0.31 (0.05)
AC4	55.72 (0.07)	25.94 (0.18)	18.88	20.61	0.36 (0.10)
AC6	54.80 (0.05)	26.83 (0.28)	11.07	12.55	0.21 (0.06)
AC7	55.70 (0.07)	26.85 (0.11)	22.66	22.99	0.21 (0.05)
AC8	54.53 (0.09)	30.20 (0.24)	17.46	19.66	0.31 (0.02)
AC9	52.67 (0.08)	30.66 (0.20)	6.71	6.63	0.33 (0.09)
AC10	55.48 (0.09)	25.97 (0.20)	12.56	14.91	0.28 (0.03)

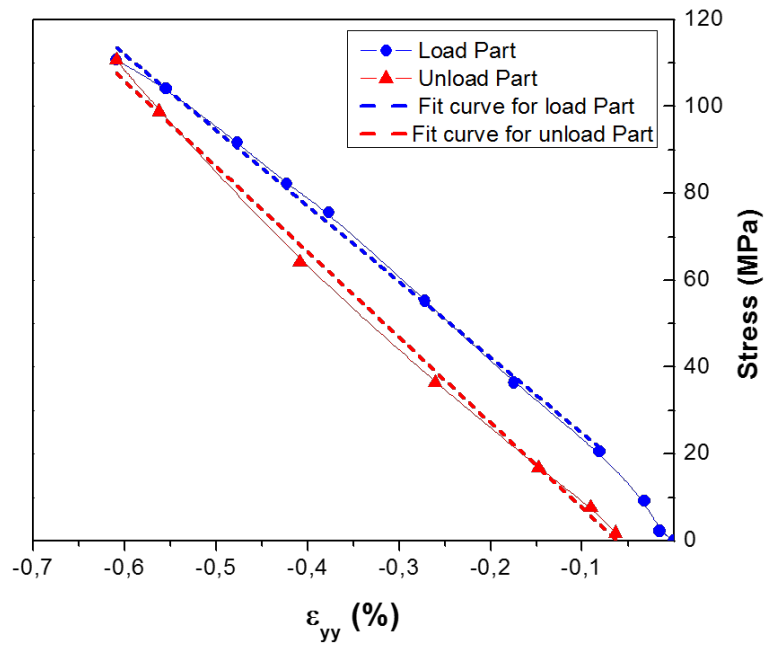


Figure 3.10 – Typical stress-strain curve of compression test for sample AC8.

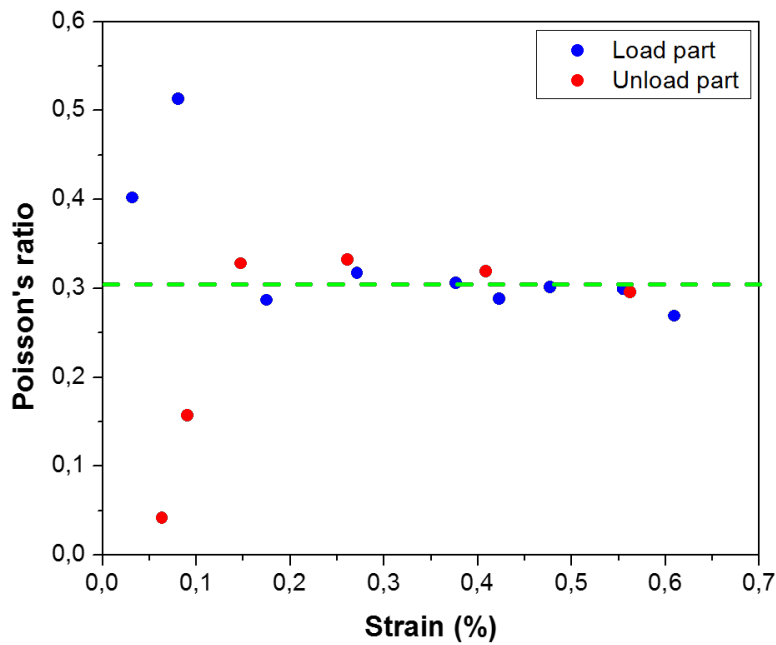


Figure 3.11 – Poisson's ratio as a function of the applied strain for sample AC8.

As shown in Fig. 3.12, uniaxial compression induced an important out-of-plan motion. The auto-focus process compensated this motion, allowing to obtain the correct strain. This process decreased the error due to delocalization. Poisson's effect of a sample with 1mm

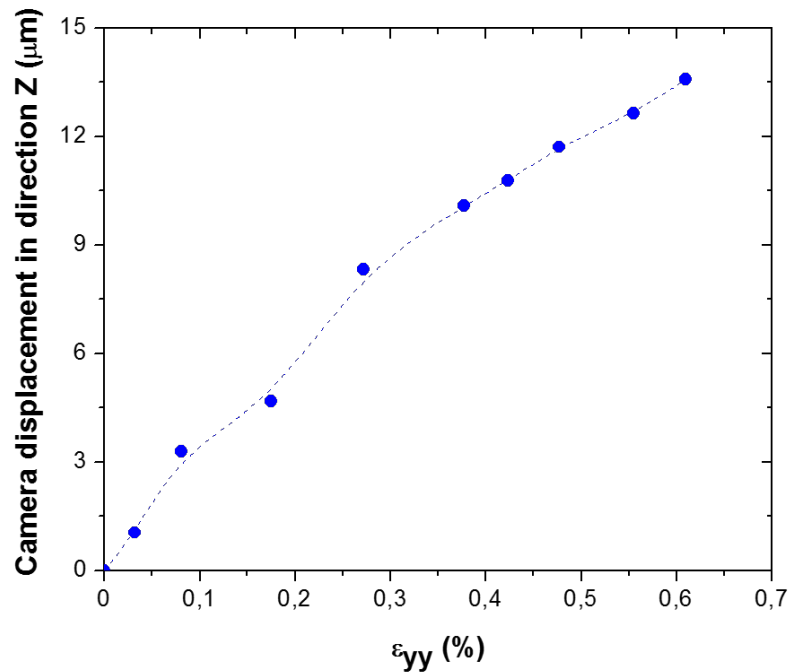


Figure 3.12 – The auto-focus positioning of the camera during a compression assay (sample AC8). It illustrates the large out-of-plane motions and the importance of the auto-focus system.

thickness under a compression stress of 0.6% creates a motion about $1\mu\text{m}$, explaining only a very small part of the camera displacement. Imperfect sample geometry or more likely nonparallel crossheads are likely to induce this large displacement.

3.2.2 Influence of the Humidity

Influence of the humidity on the elastic modulus

In order to study the influence of the relative humidity on the elastic modulus, three relative humidities (55%, 75% and 90%) were selected, while the temperature was kept constant. The

compression and DIC parameters were mentioned the same as before (Sec. 3.2.1). The same ten samples (AC1 to AC10) were used in this study. For each humidity, the elastic modulus was measured both from load and unload parts of the stress-strain curve: all the curves can be found in the appendix.B. For each sample, the measured elastic modulus under different humidities were normalized by the maximum value of the sample (see Fig. 3.13). The lower relative humidity (around 50%) was not very dry (although it correspond to a very dry room). And the water immersed sample was not tested here. The variability of the measurement is likely due to the deviation of the linear fit for load and unload parts. The humidity has no clear influence on the modulus. The elastic modulus of human dentin was then determined to be 18.7GPa with a standard deviation of 3.7GPa at 25°C.

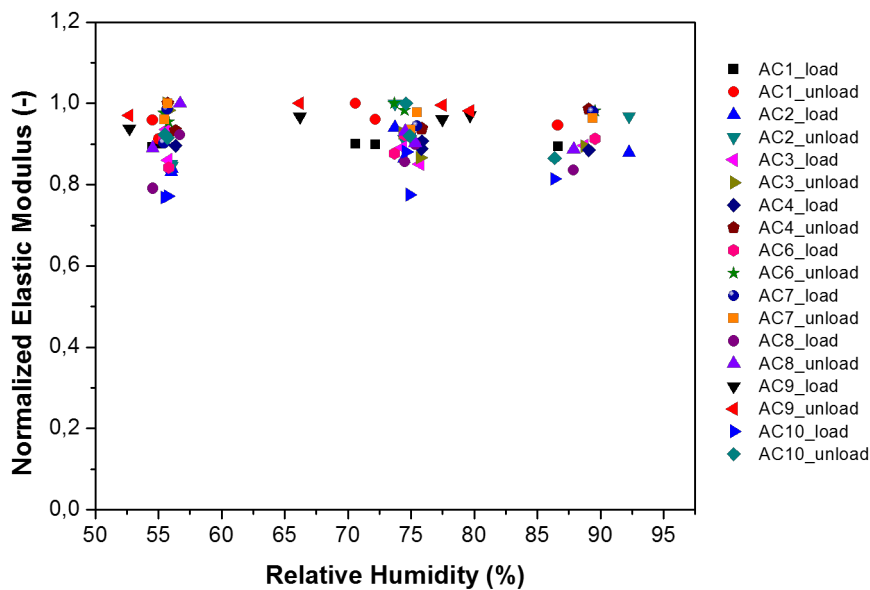


Figure 3.13 – Influence of relative humidity on the normalized elastic modulus for all specimens.

Dilatation due to humidity

After a change of relative humidity, and before the compression test, we observed a dilatation of the dentin. We quantified this effect on not-loaded samples and on loaded samples (constant stress of 35.72 ± 0.38 MPa). The relative humidity inside the environmental cham-

ber was increased from 55% to 90% and then decreased from 90% to 55%. At each selected humidity, the sample had been kept stable for at least 30 minutes in order to let the sample reach the equilibrium. After such waiting time, the strain was no longer changing with time.

Fig. 3.14 shows the strain variation for sample AC1 when we varied the humidity environments, without any applied stress. The ϵ_{xx} and ϵ_{yy} followed humidity variation immediately, whereas ϵ_{xy} did not varied, as expected.

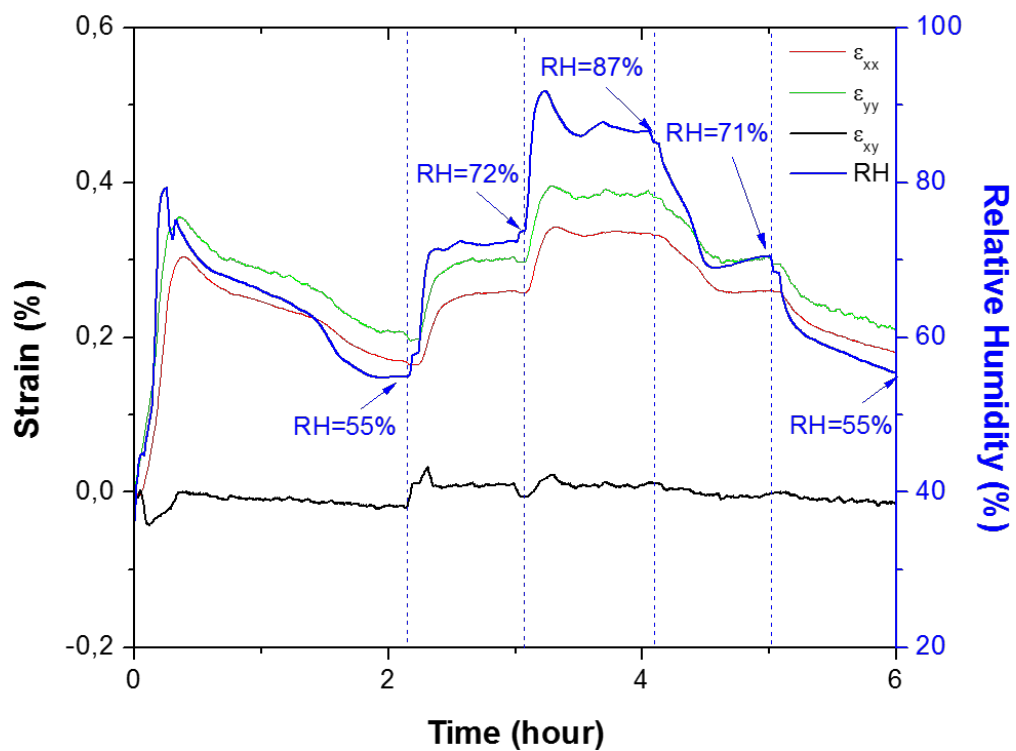


Figure 3.14 – Free dilatation of human dentin sample (AC1) as a function of time for different imposed relative humidities. The selected humidities are written on the figure. The strains in X and Y direction (ϵ_{xx} and ϵ_{yy}) follow the relative humidity, whereas the shear strain ϵ_{xy} does not vary.

A linear relationship was found for ϵ_{xx} and ϵ_{yy} strains with the relative humidity (see Fig. 3.15). Dentin humidity dilatation coefficient is then between 3×10^{-5} and 7×10^{-5} . The average values are 5.3×10^{-5} (SD:1.0) for ϵ_{xx} and 5.7×10^{-5} (SD:0.6) for ϵ_{yy} . The results were summarized in Table 3.5 and all the curves can be found in the appendix.C.

Table 3.5 – Humidity dilatation coefficients of ten dentin samples

Sample	$C_{\epsilon_{xx}}$	$C_{\epsilon_{yy}}$	$C_{\epsilon_{xy}}$
	RH ⁻¹ (S.D.)	RH ⁻¹ (S.D.)	RH ⁻¹ (S.D.)
AC1	7×10^{-5} (6×10^{-4})	6×10^{-5} (4×10^{-4})	2×10^{-6} (3×10^{-4})
AC2	5×10^{-5} (5×10^{-4})	5×10^{-5} (8×10^{-4})	8×10^{-7} (2×10^{-4})
AC3	6×10^{-5} (9×10^{-4})	6×10^{-5} (3×10^{-4})	2×10^{-6} (1×10^{-4})
AC4	3×10^{-5} (1×10^{-4})	5×10^{-5} (6×10^{-5})	3×10^{-6} (7×10^{-4})
AC5	6×10^{-5} (3×10^{-4})	7×10^{-5} (4×10^{-4})	4×10^{-6} (1×10^{-4})
AC6	5×10^{-5} (9×10^{-4})	6×10^{-5} (5×10^{-4})	-8×10^{-6} (4×10^{-4})
AC7	6×10^{-5} (5×10^{-4})	5×10^{-5} (6×10^{-4})	7×10^{-6} (3×10^{-4})
AC8	5×10^{-5} (4×10^{-4})	6×10^{-5} (3×10^{-4})	-6×10^{-6} (5×10^{-4})
AC9	5×10^{-5} (6×10^{-4})	5×10^{-5} (5×10^{-4})	4×10^{-6} (1×10^{-4})
AC10	5×10^{-5} (3×10^{-5})	6×10^{-5} (4×10^{-4})	-1×10^{-6} (3×10^{-4})
Mean	5.3×10^{-5} (1.0)	5.7×10^{-5} (0.6)	7.8×10^{-7} (4.6×10^{-6})

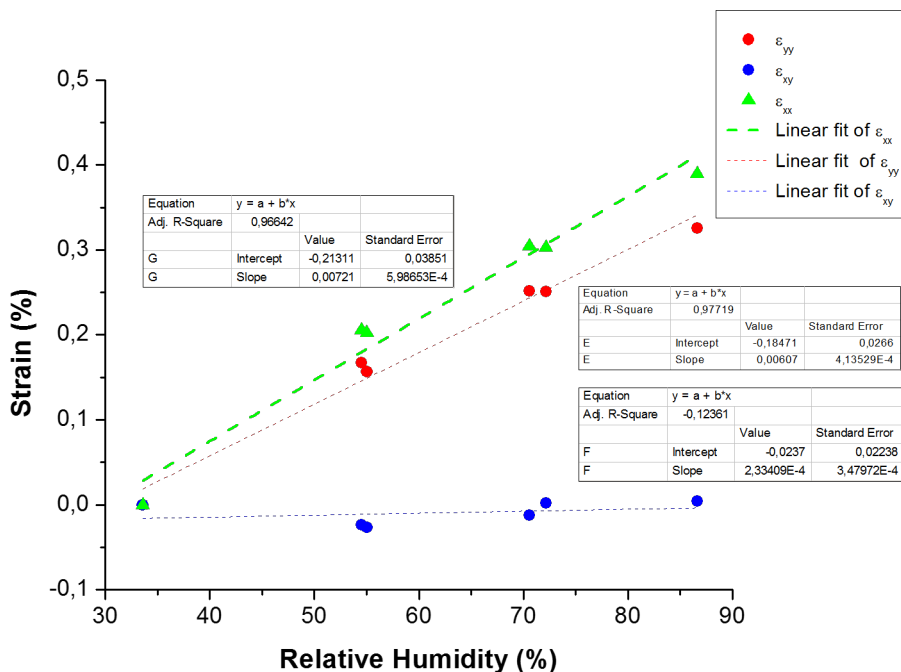


Figure 3.15 – Strain evolution with relative humidity (no stress was applied) for sample AC1.

When a constant stress (around 36MPa) was applied, the humidity dilatation coefficient slightly increase to a level of 1×10^{-4} as shown in Fig. 3.16. The figure was normalized by removing the pre-stresses for both ϵ_{xx} and ϵ_{yy} .

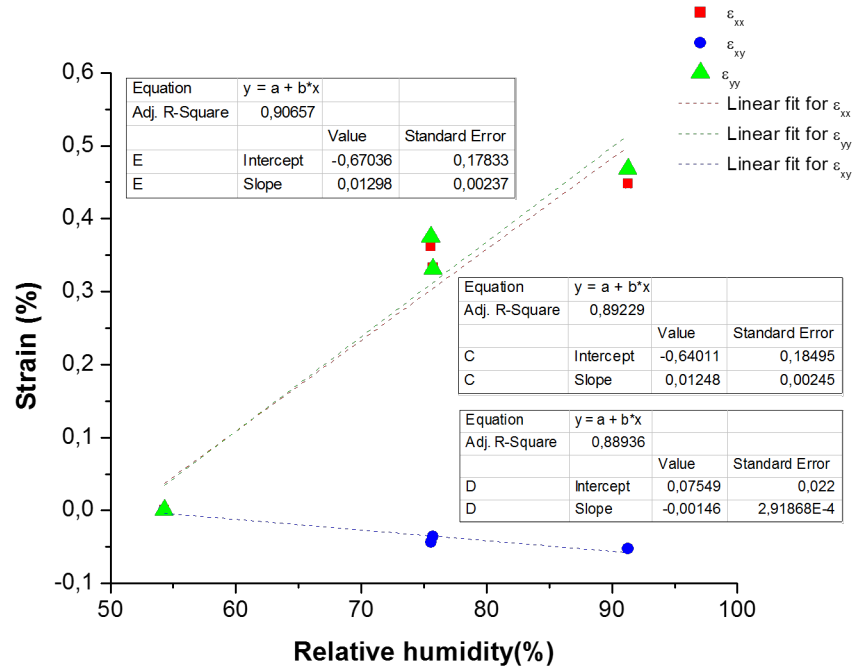


Figure 3.16 – Strain evolution with the relative humidity for a sample under a compressive stress (around 36MPa) for sample AC1.

With the hypothesis of linear isotropic elasticity, the effect of relative humidity can be introduced in the constitutive law through similar approach to the one for thermal expansion:

$$\boldsymbol{\sigma} = \lambda Tr(\boldsymbol{\epsilon})\mathbf{I} + 2\mu\boldsymbol{\epsilon} - 3K\alpha_H\Delta H\mathbf{I} \quad (3.1)$$

where $\boldsymbol{\sigma}$ is the stress tensor, $\boldsymbol{\epsilon}$ is the strain tensor, λ and μ are the Lamé parameters, K is the bulk modulus, α_H is the coefficient of hydric dilatation, ΔH is the variation in relative humidity and \mathbf{I} is the identity tensor.

Without applied stress, the stress and strain tensors can be written as:

$$\boldsymbol{\sigma} = \mathbf{0}; \quad \boldsymbol{\epsilon} = \epsilon_0\mathbf{I} \quad (3.2)$$

Then, the dilatation strain ϵ_0 is:

$$\epsilon_0 = \frac{3K}{3\lambda + 2\mu} \alpha_H \Delta H \quad (3.3)$$

With a constant applied stress σ_{zz} , the stress and strain tensors become:

$$\boldsymbol{\sigma} = \sigma_{zz} \mathbf{e}_z \otimes \mathbf{e}_z; \quad \boldsymbol{\epsilon} = \epsilon_{xx} \mathbf{I} - \epsilon_{xx} \mathbf{e}_z \otimes \mathbf{e}_z + \epsilon_{zz} \mathbf{e}_z \otimes \mathbf{e}_z \quad (3.4)$$

It should be noted that $\sigma_{zz} < 0$ and $\epsilon_{zz} < 0$, and $|\epsilon_{xx}| < |\epsilon_{zz}|$ due to the applied compressive stress. Through eq. (3.1), we obtain:

$$\sigma_{zz} = \lambda(2\epsilon_{xx} + \epsilon_{zz}) + 2\mu\epsilon_{zz} - 3K\alpha_H\Delta H \quad (3.5)$$

$$0 = \lambda(2\epsilon_{xx} + \epsilon_{zz}) + 2\mu\epsilon_{xx} - 3K\alpha_H\Delta H \quad (3.6)$$

Then, ϵ_{zz} can be written as:

$$\epsilon_{zz} = \epsilon_{xx} + \frac{\sigma_{zz}}{2\mu} \quad (3.7)$$

The deformation ϵ_{11} is then:

$$\epsilon_{xx} = \left(\frac{3K}{3\lambda + 2\mu} \right) \alpha_H \Delta H - \frac{\lambda \sigma_{zz}}{2\mu(3\lambda + 2\mu)} \quad (3.8)$$

Comparing eq. (3.8) with eq. (3.3), it turns out that the slope coefficient of the strain as a function of the relative humidity should be the same no matter a stress was applied or not. The small differences we found may be caused by the friction effects between the sample and the compression setup.

Forien et al. [2016] have shown that the water-assisted functional coupling effect inside dentin sample lead to a compressive strain due to a possible dehydration process after a mild heating treatment. From "wet" state to "dry" state, the dentin sample would have a compressive strain of 0.3% [Forien et al., 2016], which meets the magnitude of the values reported

here. A possible reason could be the porous structure of the dentin. When the relative humidity of the external environment exceeded the water content inside the dentin, the water would infiltrate into the sample and induce a dilatation effect. While the situation turns to the reverse state, the water inside the dentin may be flowing outwards. These variations with humidity can explain the variations on the quality of the bonding between restorative materials and dentin [Burrow et al., 1995; Plasmans et al., 1996, 1994; Saraiva et al., 2015].

Dentin is regarded as an heterogeneous and hierarchical biological hard tissue. The importance of its anisotropy is still under debate [Kinney et al., 2003]. The similarities of the dilatation in the two directions brings additional understanding: dentin should be considered as an isotropic material at this scale. However, at much smaller scales, the tubular orientation and the fine porous structure (as observed by CLSM in chapter 2) is likely to create anisotropy.

3.2.3 Influence of the temperature

Similarly to what was done with humidity, our setup allows to investigate the dentin thermal dilatation. Relative humidity was kept stable (around 57%) during the whole experiment to avoid the dilatations due to humidity. Fig. 3.17 shows a measurement of the temperature dilatation. Reference materials such as Invar alloy (IA), Al and Al_2O_3 were used to verify the validity of the integrated systems for thermal dilatation measurement. The resulting thermal dilatation coefficients for IA, Al and Al_2O_3 are $4 \times 10^{-6} (SD : 2.2)$, $2.5 \times 10^{-5} (SD : 2.5)$ and $1.3 \times 10^{-5} (SD : 1.2) K^{-1}$, respectively, which are in accordance with the expected values (Invar: $1.2 \times 10^{-6} K^{-1}$ [Davis, 2001], Al: $2.3 \times 10^{-5} K^{-1}$ [Touloukian et al., 1974] and Al_2O_3 : $8.1 \times 10^{-6} K^{-1}$ [Touloukian, 1966]). Surprisingly, dentin shows a negative thermal dilatation coefficient. The surface of the dentin specimen contracted due to the water loss when the temperature increased.

The same ten dentin samples (AC1 to AC10) were tested: the results are summarized in Fig. 3.18. Dentin is contracting, with both ϵ_{xx} and ϵ_{yy} negative, when the temperature increase. The deformation ϵ_{xy} remains almost zero as expected. The distribution of the thermal

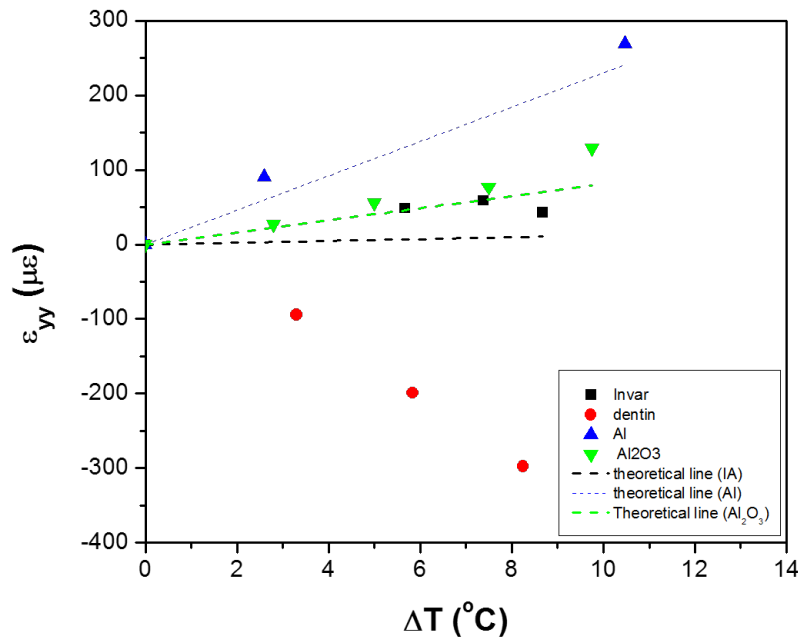


Figure 3.17 – Strain induced by a variation of temperatures for different materials. The dash lines are the expected response for Invar (IA), Al and Al₂O₃.

dilatation coefficients for each sample is plotted on Fig. 3.19. The average thermal dilatation coefficients for ϵ_{xx} and ϵ_{yy} were $-4.0(5.0) \times 10^{-5} K^{-1}$ and $-4.7(2.6) \times 10^{-5} K^{-1}$.

Thermal contraction is likely to be relayed to the change in water content. Decrease in the water content in the fibrils leads to a contraction of the fibrils, inducing a compressive stress in the surrounding hydroxyapatite crystals [Forien et al., 2016]. Temperature can change the water content inside the collagen fibril. An increase of temperature decreases the room for water in the fibril, leading to a contraction. A scheme of such a procedure is presented on Fig. 3.20. This may explain our negative thermal expansion coefficient.

Positive thermal expansion coefficients were reported [Hengchang et al., 1989; Kishen & Asundi, 2001], but without a careful control of the humidity. A negative expansion was observed on the whole human tooth by a standard thermal expansion experiment [Kishen & Asundi, 2001].

Without considering the natural negative expansion behavior of the human dentin, the

3.2. In-situ Compression Test within the setup

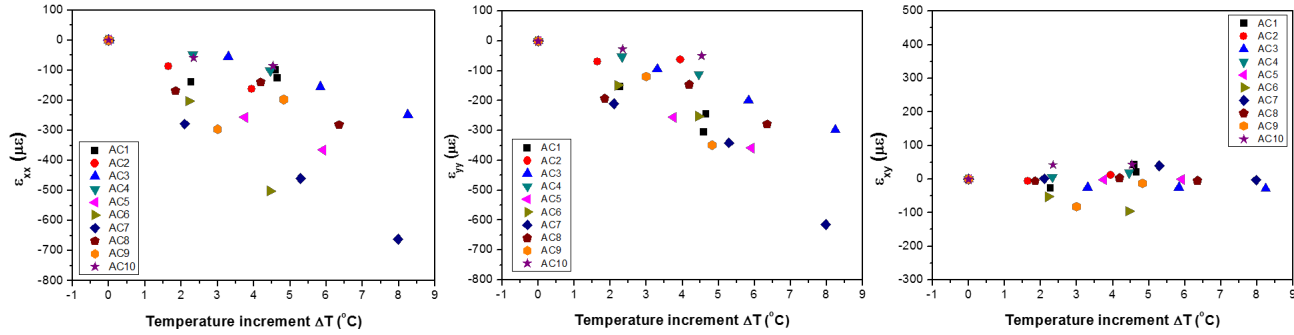


Figure 3.18 – Measured deformations (ϵ_{xx} , ϵ_{yy} and ϵ_{xy}) for the ten dentin samples during an increase of the temperature at fixed humidity.

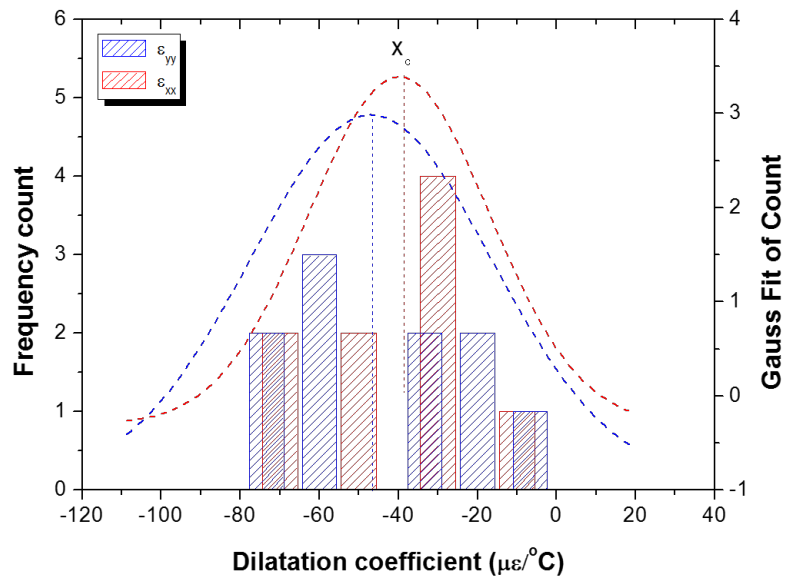


Figure 3.19 – Distribution of the dilatation coefficients for our ten samples. A Gaussian fitting (dashed line) was used to obtain the mean value and the standard deviation. The averages are indicated by the dotted vertical lines.

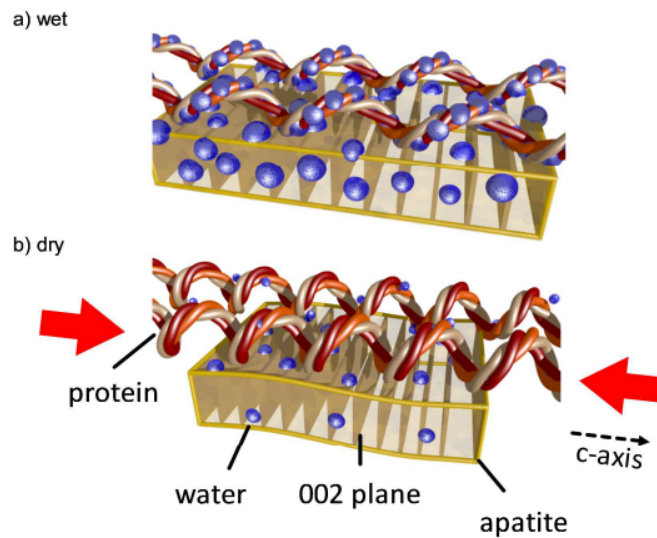


Figure 3.20 – Illustration of the compression mechanism in drying dentin, (a) in the fully hydrated state, the mineral and collagen phases are saturated by water. The collagen is at the maximum swollen state. (b) After dehydration, much of the surface-bound water is lost and the collagen molecules contract, compressing the mineral particles due to their strong binding with the shrinking collagen (Image from [Forien et al., 2016]).

mismatch between the restorative materials and the dentin would lead to a pre-stress and strain state. Due to the long-term variation of the external environmental conditions, such mismatch may lead to a fatigue failure [Brown et al., 1972]. The observed negative expansion behavior of human dentin sample here may provide substantial suggestions for the improvement of the new restoration materials or dental restoration procedures.

3.3 Resonant Ultrasound Spectroscopy

Resonant Ultrasound Spectroscopy (RUS) is a promising, alternative method to measure the elastic properties of the dentin. A significant advantage of RUS is that it gives all the elastic constants in one experiment. RUS is based on the measurement of the vibrational eigenmodes of the specimen. The determination of the elastic constants requests an inverse problem, which can be easily solved only for very well defined geometries (parallelepiped or spheres) of the sample. In this section, the principle of the RUS is briefly presented. Next, we present the RUS measurements of the elastic constants of our ten dentin samples. The mea-

surements and analysis were conducted by Dr. Xiran CAI at the LIB (Laboratoire d'Imagerie Biomédicale) of University Paris VI. The results from RUS were then compared with the *in-situ* compression results.

3.3.1 Principle of RUS

This part is inspired from the works of [Bernard et al. \[2014\]](#) and [Leisure & Willis \[1997\]](#). The Resonant Ultrasound Spectroscopy (RUS) contains two processes: the forward and inverse processes. The forward process provides the natural frequencies if the elastic tensor is given. The inverse process searches for the elastic components when the resonant frequencies are measured. Through a fitting process between the measured and the model predicted frequencies, the elastic constants can be determined.

Forward process

The natural resonant frequencies can be calculated from a given regular shape of a solid. The solutions for a freely vibrating elastic body are the stationary points of the Lagrangian L which can be expressed as follow [[Bernard et al., 2014](#)]:

$$L = \frac{1}{2} \int_V (\rho\omega^2 u_i^2 - C_{ijkl} \epsilon_{ij} \epsilon_{kl}) dV \quad (3.9)$$

where V and ρ are the specimen volume and mass density, C_{ijkl} is the stiffness tensor, u_i is the i th component of the displacement field, and ϵ_{ij} is the strain tensor. The displacement field components are expanded as finite sums of known basis functions through the Rayleigh-Ritz method as:

$$u_i = a_{i\alpha} \Phi_\alpha \quad (3.10)$$

where $a_{i\alpha}$ are the expansion coefficients and Φ_α are the basis functions. The Φ_α are selected depending on the shape of the sample. For parallelepipeds, the basis functions Φ_α are often selected as the Legendre polynomials [[Leisure & Willis, 1997](#)]. Substituting the expansion

formula into the Lagrangian will lead to a more compact format:

$$L = \frac{1}{2}((\rho\omega^2)\mathbf{a}^T \mathbf{M}\mathbf{a} - \mathbf{a}^T \mathbf{\Gamma}\mathbf{a}) \quad (3.11)$$

where \mathbf{a} is the vector containing the expansion coefficients, \mathbf{M} and $\mathbf{\Gamma}$ denote the mass and stiffness matrices of the vibration problem. By setting $\delta L = 0$, the formula turns to a generalized eigenvalue equation:

$$\mathbf{\Gamma}\mathbf{a} = \rho\omega^2 \mathbf{M}\mathbf{a} \quad (3.12)$$

where the eigenvalues are $\lambda = \rho\omega^2$ and the eigenvectors, \mathbf{a} , are the expansion coefficients. Thus, if the stiffness tensor and density are given, the resonant frequencies of an elastic solid can be calculated.

Inverse process

The elastic components of the elastic tensor are generally determined through an optimization process in which the stiffness constants are adjusted until the best fitting between the measured and predicted frequencies spectroscopy. By solving this inverse problem, the elastic components are determined. The cost function is defined and minimized as follow [Bernard et al., 2014]:

$$F = \sum_{i=1}^n \left(\frac{f_n^{meas.} - f_n^{pred.}(C_{ij})}{f_n^{meas.}} \right)^2 \quad (3.13)$$

Measurement of the resonant frequencies

A typical RUS setup (developed in Laboratoire d'Imagerie Biomédicale of UPMC Paris VI) is used to measure the vibrational eigenvalues of the dentin parallelepipeds. The sample was placed between a pair of transducers (V154RM, Panametrics, Waltham, MA) as shown in Fig. 3.21. A range of frequency is swept to active the resonant response of the specimen. When the frequency of the driving transducer reaches one of the resonant frequencies of the sample, a peak will appear in the spectroscopy diagram. When the enough spectrum is recorded, the elastic constants can be deduced following through the forward and inverse

processes.

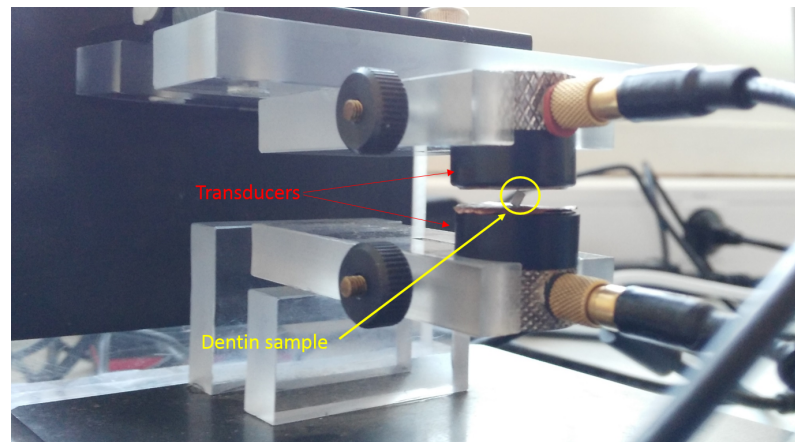


Figure 3.21 – Photo of a typical RUS setup (Laboratoire d’Imagerie Biomédicale, UPMC Paris 6)

3.3.2 Results of RUS

The same ten samples used in section 3.2 were tested using RUS experiment. The resonant frequencies of vibration were measured between 0.5 and 1.4MHz. As reviewed in chapter 1, dentin can be assumed as a transverse isotropic material. Thus, only five independent elastic parameters (see sec. 1.2.1) need to be determined. The results were summarized in Table 3.6.

The geometry of the sample is extremely important in RUS characterization: it is a key assumption for the inverse problem. Thus, an irregular geometry will certainly lead to a wrong estimate of the mechanical parameters. The measured density of dentin is 2.12 (SD:0.04) mg/mm³, which shows only little deviation so we don’t have large variation in global porosity. The direction 3 is the longitudinal direction of the samples. The elastic constants in hydrated dentin exhibited nearly isotropy characteristics: the measured E_1 and E_3 are 23.01 GPa (SD:1.69 GPa) and 23.32 GPa (SD:1.83 GPa) respectively. However, a pronounced anisotropy observed in the Poisson’s ratio: $\nu_{12} = 0.47$ (SD:0.05) and $\nu_{31} = 0.30$ (SD:0.02). These values are in accordance with the literature [Kinney et al., 2004], in which a slightly transverse isotropic characteristics is found. In their work, E_1 and E_3 are found to be 25.0

Table 3.6 – RUS measurements of the elastic coefficient for our ten dentin samples.

Sample	Dimension (mm)	Mass (mg)	Density (mg/mm ³)	E_1 (GPa)	E_3 (GPa)	G_{13} (GPa)	ν_{12}	ν_{31}
AC1	0.95 × 1.16 × 3.05	6.86	2.04	23.21	24.46	7.95	0.46	0.30
AC2	0.77 × 0.66 × 3.06	3.35	2.18	24.29	25.94	8.28	0.47	0.30
AC3	0.65 × 0.79 × 2.58	2.83	2.13	23.44	24.53	8.02	0.46	0.31
AC4	1.00 × 0.88 × 1.99	3.66	2.10	22.45	23.90	7.79	0.44	0.32
AC5	1.36 × 1.28 × 2.88	10.56	2.10	22.17	20.67	7.89	0.41	0.32
AC6	1.05 × 1.07 × 2.19	5.30	2.16	22.76	21.05	7.94	0.43	0.31
AC7	1.10 × 0.78 × 2.47	4.51	2.12	24.56	23.23	8.63	0.42	0.30
AC8	0.95 × 1.14 × 2.14	4.83	2.10	21.95	24.34	7.24	0.51	0.30
AC9	1.42 × 1.40 × 2.02	8.56	2.12	25.58	21.55	8.64	0.48	0.27
AC10	1.00 × 0.90 × 3.03	5.86	2.15	19.90	24.69	6.33	0.57	0.29
Mean			2.12	23.01	23.32	7.86	0.47	0.30
S.D.			0.04	1.69	1.83	0.72	0.05	0.02

and 23.2GPa, receptively. G_{13} was found to be 9.4GPa. Poisson's ratio were found to be 0.45 and 0.29 for ν_{12} and ν_{31} .

The comparison of the mechanical parameters between RUS and compression is shown in Fig. 3.22 where we plotted RUS modulus versus compression modulus. Modulus from RUS were always larger than those obtained by the compression test, and always in the same range, contrary to the ones obtained in compression. The maximum values of the elastic modulus obtained from both techniques are almost the same (around 25GPa). A possible explanation of this discrepancy may be the micro-cracks inside the sample, which may decrease the value measured by the compression test. RUS method is less sensitive to the micro-cracks, since the RUS is based on the measurement of a part of spectrum associated with deformations at the sample scale [Leisure & Willis, 1997]. What's more, the elastic moduli may be affected by distinct strain rates due to dentin's viscoelasticity as reported by Jantarat et al. [2002]. The strain rate used in compression test was around $5 \times 10^{-4} s^{-1}$ which may be seen as a statical measurement, whereas, the RUS should be treated as a dynamic one. Poisson's ratio from the two techniques are comparable. They are always in the same range around 0.3 for the longitudinal direction.

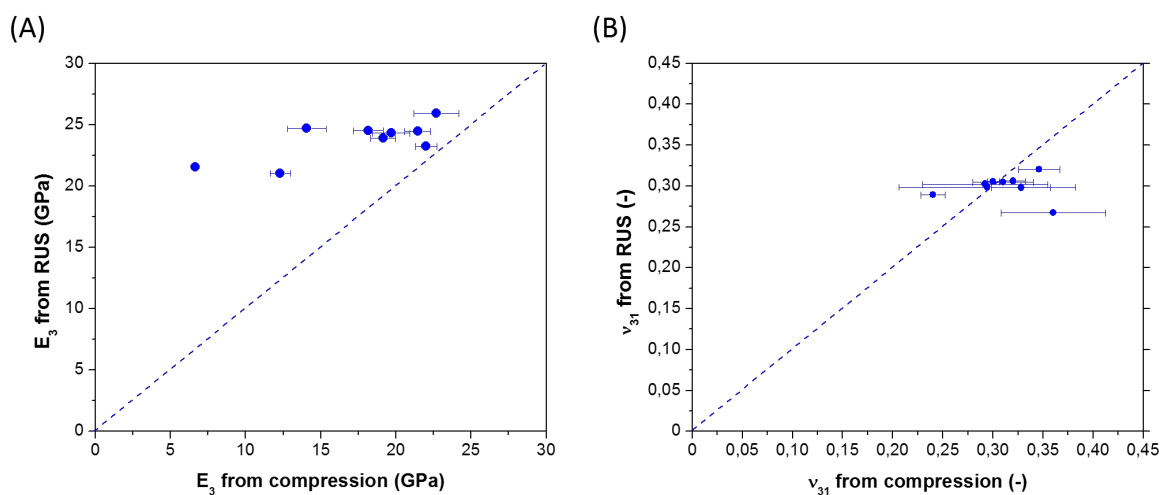


Figure 3.22 – Comparison between RUS and compression. (A) E_3 from RUS versus E_3 from compression; (B) ν_{31} from RUS versus E_3 from compression. Error bars represent the standard error of the five repeated tests in compression.

3.4 Summary of Meso-scale Mechanical Characterization of Human Dentin

An integrated system was developed to control simultaneously the humidity and the temperature of the environment around a compression device, equipped for real-time DIC strain measurement. Noise errors were quantified in the range of a few tenth of $\mu\epsilon$.

Compression tests on human dentin were conducted within this system. The elastic modulus of human dentin at meso-scale was determined to be 16.7GPa with a standard deviation of 5.1GPa. the Poisson's ratio was found to be 0.31. No strong influence of humidity and temperature was observed on this modulus.

The dilatation behavior of human dentin with the relative humidity was explored: an increase of the relative humidity induces a significant isotropic dilatation of the dentin. Thermal effects were investigated the same way. Surprisingly, we observed a contraction of the sample when the temperature increased. This uncommon behavior is likely to be related to a modification of the water molecules around the collagen fibrils in the dentin.

Other methods were tested to measure the meso-scale mechanical properties: RUS and three point bending tests (see Appendix.D). The RUS method provides all the elastic constants in one single test. The results show that the elastic moduli of human dentin present slight transverse isotropic characteristics ($E_1 = 23.01$ and $E_3 = 23.32$) and strong anisotropy in the Poisson's ratio ($\nu_{12} = 0.47$ and $\nu_{31} = 0.30$) with little variation between our samples. However, the obtained results are comparable with the compression results, but which are more sensitive to the micro-defects.

MICRO-SCALE MECHANICAL CHARACTERIZATION

The macroscopic mechanical properties of human dentin have been measured by *in-situ* compression tests in the previous chapter. However, these properties were not linked to the micro-structure of the samples. For biomedical applications, or for fine modeling, it is of interest to relate a micro-structure as observed for example in part to the macroscopic properties. This requests obviously a fine knowledge of the properties of each component of the dentin. In this chapter, the mechanical properties of dentin components (peritubular dentin and intertubular dentin) were characterized by nanoindentation. We also gave some consideration to the dentin viscoelastic behavior.

4.1 Nanoindentation for peri and intertubular dentin

4.1.1 Sample preparation

Nanoindentation was used to measure the local moduli of peri- and inter-tubular dentin on the same ten samples used for the compression part. The surfaces to be tested were carefully

re-polished through a classical process (1200, 2000, 4000 SiC papers until $1\mu m$ suspending diamond cloth polishing) to clean the surface. Between each step, the sample was cleaned in an ultrasonic bath to remove the debris.

4.1.2 Indentation Parameters

More than 100 indents arranged as a matrix were applied to each sample. The indentation was controlled under depth mode. An indentation depth of $200nm$ was used for each test with a strain rate of $0.05s^{-1}$. After the loading phase, the indenter had a holding period of 10s. Then, the sample was unloaded at the same strain rate. Both CSM mode and unload mode were used to determine the elastic moduli (see chapter 1). During the analysis process, the Poisson's ratio was assumed as 0.3, based on our macroscopic measurements. Poisson's ratio of the bone collagen was measured as 0.35 [Currey, 1964], while a Poisson's ratio of 0.25 was used for peritubular dentin in the micro-mechanical model of Qin & Swain [2004]. Therefore, a Poisson's ratio of 0.3 sounds a reasonable assumption.

4.1.3 Atomic Force Microscope observation

Traditional observation tools like optical microscope didn't resolve the indents, due to their small sizes. Thus, Atomic Force Microscope (AFM) was used to observe the locations of the indents in all the samples.

Principle of AFM observation

The AFM is widely used to image the micro-structure of biological samples. The general principle of AFM is based on the interaction forces (van der Waals forces, electrostatic and etc.) between the specimen and a tip on a cantilever (see Fig. 4.1). The cantilever is installed on a piezoelectric scanner which gives a three dimensional control of position with a high precision. The force between the sample and the tip is quantified by the cantilever deflection

with a piconewton sensitivity. The deflection of the cantilever is determined by the movement of a laser beam reflecting on it as illustrated in Fig. 4.1 [El Kirat et al., 2010].

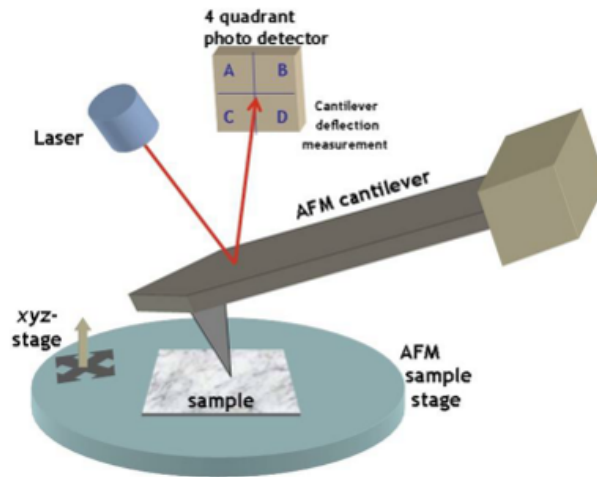


Figure 4.1 – Illustration of the typical atomic force microscope (AFM) setup. The deflection of a micro-fabricated cantilever with a sharp tip is measured by reflecting a laser beam off the backside of the cantilever while it is scanning over the surface of the sample (Image from [Goddard Iii et al., 2007]).

Different modes are possible. We used the classical contact mode in air. The topography of the surface is measured by the feedback signal required to keep a constant force on the cantilever. The tip is firmly in contact with the surface of the sample as shown in Fig. 4.2. We

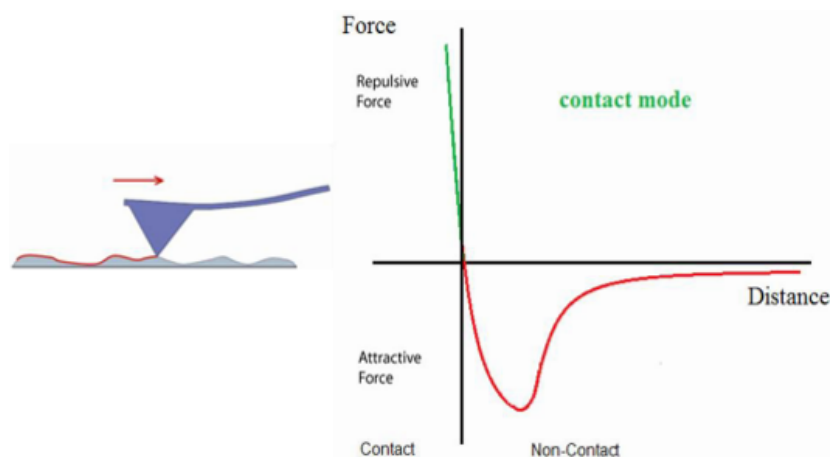


Figure 4.2 – Illustration of the contact mode principle [Jaramillo Isaza, 2014]. The tip is pushed on the surface (in the region of repulsive forces (in green on the force - displacement curve). The vertical position of the scanner is adjusted so that the force is kept constant.

use the AFM (Bruker Corp. USA in LMS at Ecole Polytechnique) with a nitride cantilever

($f_0 = 70\text{KHz}$ and $k = 0.4\text{N/m}$) with a silicon tip.

Results of AFM observation

Fig. 4.3 shows an AFM image of a dentin sample (AC6). The locations of the indents from nanoindentation are well visible. We consider that the indentation probed peritubular or intertubular dentin according the center location of the indents. The highlight image on the right of Fig. 4.3 shows two indents. The top one is located inside the area between peritubular dentin and intertubular dentin, while the bottom one is located in the intertubular dentin.

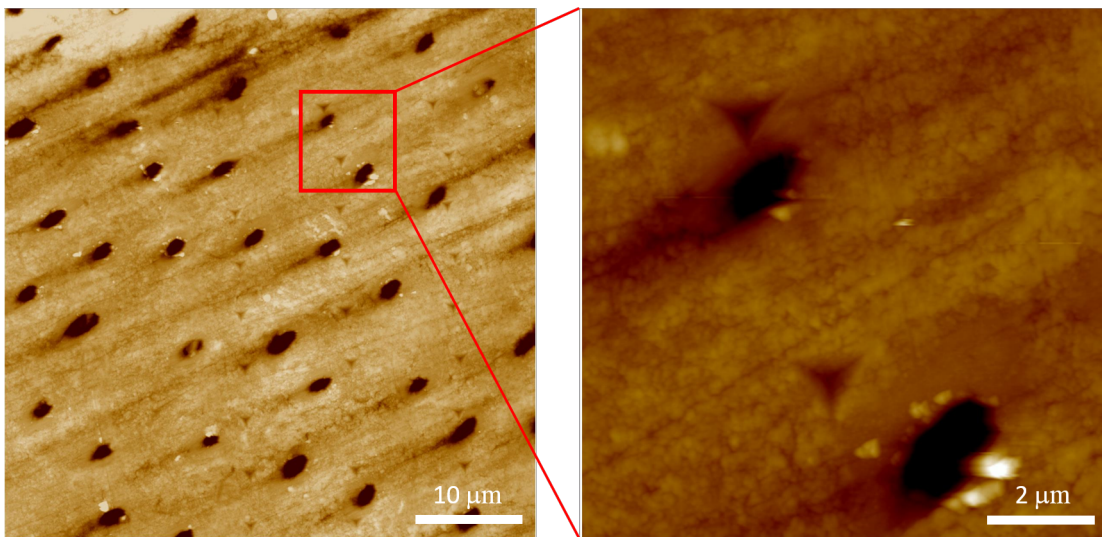


Figure 4.3 – AFM image fo sample AC6 used to find the locations of the indents on the surface of dentin sample. The highlight image on the right show a indent located inside the area between peritubular dentin and intertubular dentin (top one) and an indent (bottom) located in the intertubular dentin.

4.1.4 Results of nanoindentation

Typical force-displacement curves for peritubular and intertubular dentin are shown in Fig. 4.4. The loading is associated to an exponential nonlinear loading behavior due to the elastic and plastic response of dentin. The beginning of the unloading part is linear, associated with the elastic response. We extracted the elastic modulus by both CSM and unload methods (see sec. 1.3.2).

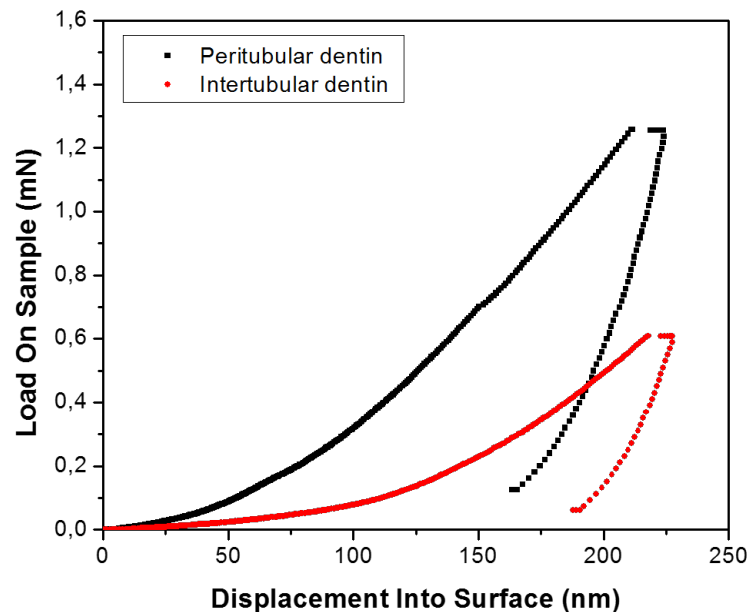


Figure 4.4 – Typical load and displacement curves from nanoindentation tests on peri and intertubular dentins

The elastic modulus and hardness obtained by the CSM method for peri and intertubular dentin are shown in Fig. 4.5 and Fig. 4.6 (same experiments as Fig. 4.4). The values quickly reach a stable value when the indenter penetrates the sample. These limit values were considered as the measure of the modulus and hardness. As expected, peritubular dentin has larger elastic modulus and hardness than intertubular dentin.

The resulting elastic modulus and hardness from more than 100 indentation tests were attributed to peritubular or intertubular dentin using the AFM observations. All the results were plotted into a histogram, which showed two groups (see Fig. 4.7 and Fig. 4.8). These groups correspond to peri and intertubular dentin components.

The elastic modulus from both methods (CSM and unload) of the two components of dentin are summarized in Table 4.1. Intertubular dentin has average modulus of 16.2GPa (SD:5.52GPa) and 16.1GPa (SD:4.1GPa) for CSM and unload methods respectively. Peritubular dentin has average modulus of 26.7GPa (SD:3.4GPa) and 25.1GPa (SD:3.0GPa).

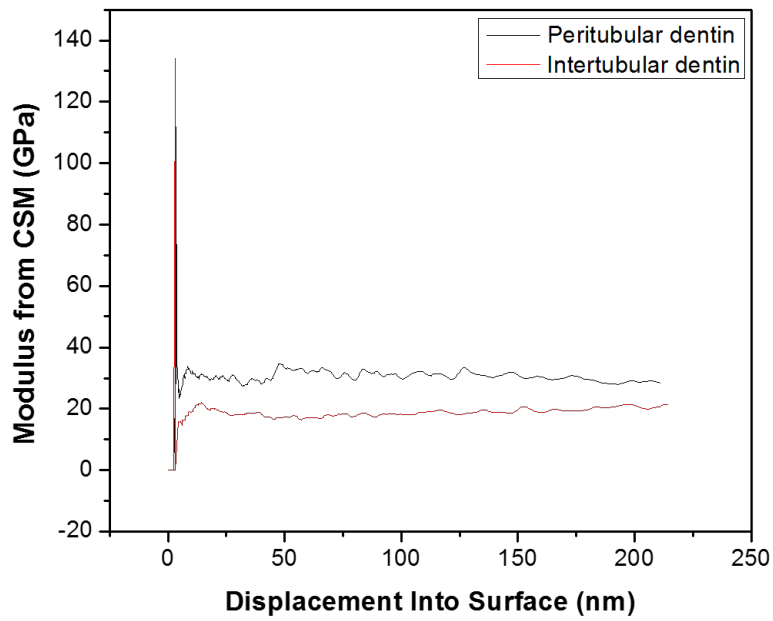


Figure 4.5 – CSM elastic modulus obtained for peri and intertubular dentins from the same experiment as Fig. 4.4.

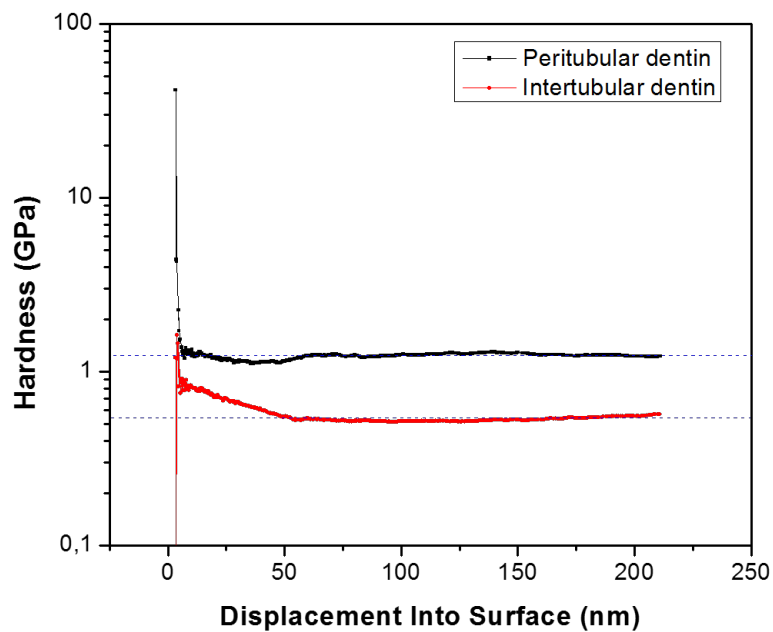


Figure 4.6 – CSM hardness for peri and intertubular dentins, from the same experiment as Fig. 4.4.

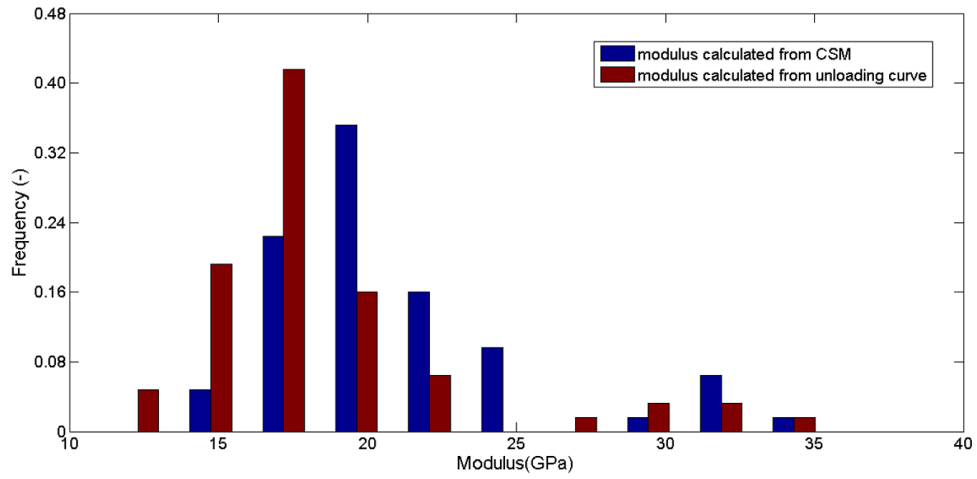


Figure 4.7 – Typical histogram of elastic modulus from nanoindentation tests (sample AC8)

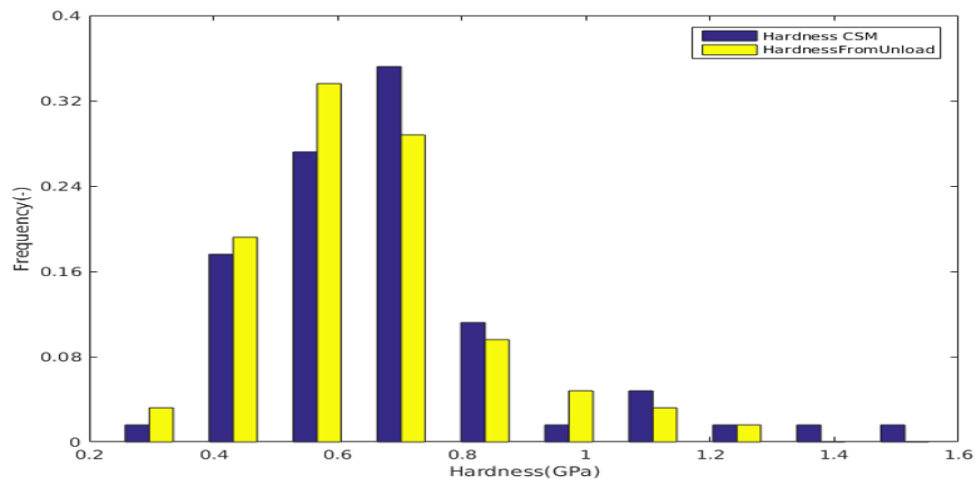


Figure 4.8 – Typical histogram of hardness from nanoindentation tests (sample AC8)

The results are in agreement with the literature [Kinney et al., 2003]. According to Oliver & Pharr [2004], CSM method allows to avoid some of the complicating effects of time-dependent plasticity and thermal drift, and thus it may provide a better estimate of the elastic parameter. One of the main drawback of the indentation is the lack of knowledge on the Poisson's ratio, which had to be guessed.

The locations were verified by AFM. The surface ratios for each component of dentin of the samples were estimated from the ratio of the indentation tests for each component among the number of all the tests. For example, the value of the number of indents located in the tubules (seen in AFM image) divided the total test number gives the tubules surface ratio. The surface ratios for each sample were summarized in Table 4.2. The average values for tubules, peritubular dentin and intertubular dentin were found to be 5.2%, 10.1% and 84.6%. These values match with the ESEM observations (see chapter 2). The mixture rule was applied to predict the macro-scale effective properties. The average value of elastic modulus was found to be 16.4GPa. The modulus obtained from mechanical tests was 17.3GPa (SD:5.0GPa), thus in good agreement. However, the values from RUS measurement showed clearly over estimation with an average value of 23.2GPa.

Generally, data of nanoindentation were analyzed the elastic half-space assumption. The contact between the indenter and the sample is then considered be elastic, and the sample is treated as an infinite half-space medium [Oliver & Pharr, 1992]. However, the indentation locations for the peritubular dentin are near the tubules (pores) or at the transition from peritubular dentin to intertubular dentin. The stress and deformation field may then be influenced by the surrounding structure [Chen & Vlassak, 2001] in an uncontrolled fashion. Besides, the Poisson's ratio was assumed as 0.3, which may bring roughly 20% uncertainty for the measurements.

Table 4.1 – Results of average elastic moduli for peri and intertubular dentin

Sample	E_i from CSM (GPa)	E_i from unload (GPa)	E_p from CSM (GPa)	E_p from unload (GPa)	Comments
AC1	16.6 (3.3)	15.5 (3.0)	28.5 (4.6)	26.2 (4.6)	
AC2	9.4 (1.6)	9.0 (1.5)	22.03	21.03	Locations not found
AC3	8.1 (1.1)	9.4 (1.1)	12.9 (1.8)	12.7 (0.7)	Locations not found
AC4	9.2 (2.1)	11.0 (1.9)	20.9 (1.4)	20.5 (2.3)	Locations not found
AC6	22.0 (2.6)	20.1 (2.3)	27.8 (2.5)	25.0 (2.2)	
AC7	22.1 (2.5)	18.6 (5.6)	28.8 (1.6)	26.2 (2.6)	
AC8	19.7 (2.5)	17.2 (2.5)	31.7 (1.9)	30.5 (2.6)	
AC9	21.9 (1.7)	19.7 (1.7)	28.5 (2.0)	26.7 (1.6)	
AC10	16.6 (1.7)	14.3 (2.4)	25.3 (2.5)	24.3 (4.7)	
Mean (S.D.)	16.2 (5.5)	16.1 (4.1)	26.7 (3.4)	25.1 (3.0)	Except AC2-AC4

Notes: the indents of AC2-AC4 couldn't be found in AFM image. The indents might be too shallow.

Table 4.2 – Comparison of the moduli obtained using microscopic measures (homogenized with the mixture rule), using macroscopic compression test and using RUS measurement.

Sample	R_t (%)	R_p (%)	R_i (%)	E from mixture rule (GPa)	E from compression (GPa)	E_g from RUS(GPa)	Comments
AC1	4.8 (2.8)	22.4 (3.5)	72.8 (3.8)	18.5	21.4 (0.9)	24.5	fraction by ESEM
AC2	4.9 (2.0)	13.2(6.0)	82.0 (7.9)	10.6	22.7 (1.5)	25.9	fraction by ESEM
AC3	2.3 (0.2)	9.1 (0.6)	88.7 (0.7)	8.4	18.1 (1.0)	24.5	fraction by ESEM
AC4	4.5 (0.4)	8.3 (1.3)	87.2 (1.5)	9.7	19.1 (0.8)	23.9	fraction by ESEM
AC6	5.7	6.2	88.1	21.1	12.3 (0.7)	21.1	
AC7	5.3	6.1	88.6	21.3	22.0 (0.7)	23.2	
AC8	5.1 (0.8)	10.7 (1.7)	84.2 (2.4)	20.0	19.7 (1.2)	24.3	fraction by ESEM
AC9	4.3	8.7	87.0	21.5	6.6 (0.1)	21.6	
AC10	6.3	6.8	86.9	16.1	14.1 (1.3)	24.7	
Mean (S.D.)	5.2 (0.7)	10.1 (6)	84.6 (6)	16.4 (5.1)	17.3 (5.0)	23.2 (1.6)	

Notes: ratio of tubular and peritubular dentin for AC6, AC7, AC9, AC10 were deduced from the indentation results

4.1.5 Summary of nanoindentation experiments

Elastic modulus for both components of dentin (peritubular and intertubular dentin) was determined by nanoindentation. Two methods (CSM and unload) were used. The locations of the indents were determined by AFM observations. The resulting elastic moduli of the peri and intertubular dentin were determined as 16.2GPa and 26.7GPa for CSM measurements, and as 16.1GPa and 25.1GPa, for unloading method. The surface ratios of each dentin component was estimated from the indentation test associated with location observation by AFM. The average values for tubules, peritubular dentin and intertubular dentin were found to be 5.2%, 10.1% and 84.6%, comparable with the values obtained from the ESEM observations. The mixture rule was then used to predict the meso-scale effective properties, which are found to be in the range of the ones determined by compression tests.

4.2 Viscoelastic behavior

Fifty creep tests were conducted in order to estimate the viscoelastic behavior. The indentation was done in load control mode. The maximum load was set as 0.4mN, with a loading rate of 0.08mN/s. The holding period was set at 20s. Then, the sample was unloaded. Typical loading-unloading consist and the resulting load-displacement curve are shown in Fig. 4.9.

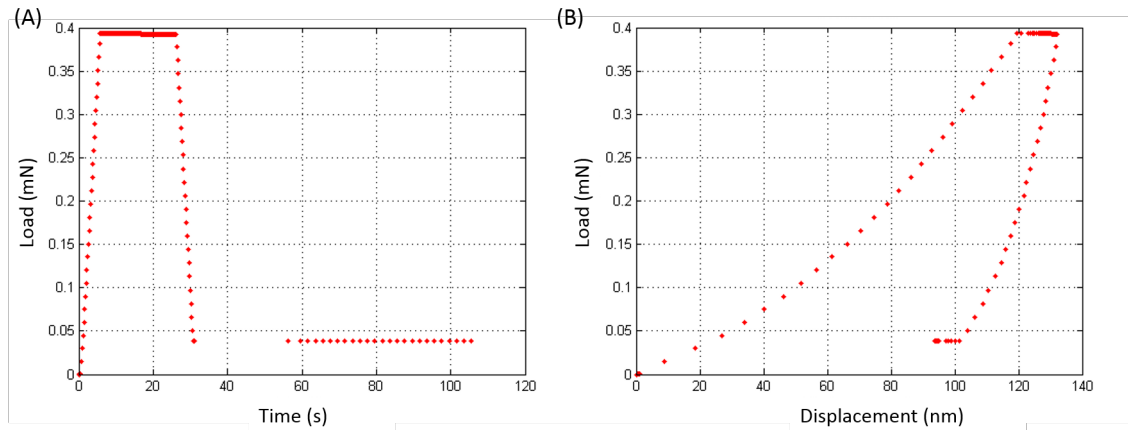


Figure 4.9 – Typical load history and load-displacement curves to estimate the viscoelastic behavior of dentin. (A) Load history, (B) Load-displacement curve.

During the holding process, the displacement showed a significant creep behavior: the displacement increased in a nonlinear way with time (see Fig. 4.10).

Using a four-element spring-dashpot model (the Burger model see Fig. 4.10), the displacement of a conical indenter can be described as [Fischer-Cripps, 2004]:

$$h^2(t) = \frac{\pi}{2} P_0 \cot \alpha \left[\frac{1}{E_1^*} + \frac{1}{E_2^*} (1 - e^{-tE_2^*/\eta_1}) + \frac{1}{\eta_2} t \right]$$

where E_i^* is the combination of the elastic modulus and Poisson's ratio of the material i (1 being the sample, 2 being the indenter): it can be written as $E^* = E/(1 - \nu^2)$. η_i is the viscosity term that quantifies the time-dependent property of the material. P_0 is the load and α is a geometrical angle ($\alpha = 70.3$ for Berkovich indenter).

The fitting parameters of the Burger model are summarized in Table 4.3. Compared with

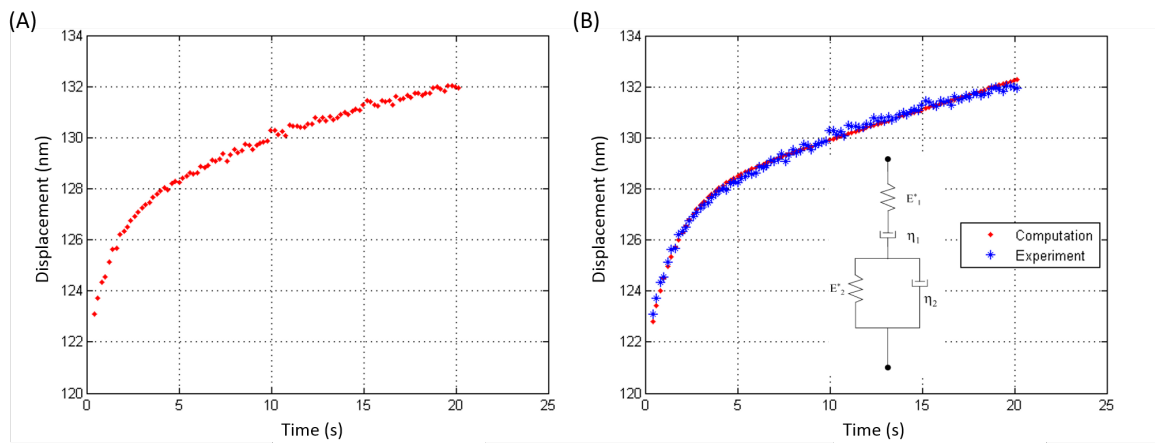


Figure 4.10 – (A) Creep behavior of dentin component. (B) Comparison between the experimental creep behavior and the simulation curve based on a four-element combined spring-dashpot model.

classical visco-elastic materials like polymer, dentin has smaller time-dependent properties. Two or three spring-dashpot elements models were also attempted to model the creep behavior, but led to a less accurate fit [Fischer-Cripps, 2004]. Since the Burger model enabled also to capture the immediate elastic response, we considered that it was a better choice. The elastic response measured here is comparable with our previous results from compression and RUS, as expected. The creep time constant (η_1/E_2) was found to be around 2s, which is of the same magnitude as the one reported for human cortical bone [Wu et al., 2009; Isaksson et al., 2010].

Table 4.3 – Average fitting parameters for Burger model. Mean and SD are obtained by comparing the 50 tests.

	E_1 (GPa)	E_2 (GPa)	η_1 (GPa.s)	η_2 (GPa.s)
Dentin	21.04 (6.78)	189.52 (66.57)	364.30 (139.55)	5305.82 (1994.15)

4.2.1 Strain rate sensitivity

Fifty indentation tests were done to access the strain-rate sensitivity for both peri and intertubular dentins. The indent strain rate ($\dot{\epsilon}$) was defined as the indenter displacement velocity divided by the indentation depth ($\dot{\epsilon} = \frac{dh}{dt} \frac{1}{h(t)}$) [Fischer-Cripps & Nicholson, 2004; Song et al.,

2009]. Three strain rates were chosen ranged from 1×10^{-4} to 0.1 s^{-1} . As shown in Fig. 4.11, the elastic modulus of both components did not vary with the strain rate, although a little tendency to increase was observed for intertubular dentin, maybe due to the lower mineral fraction.

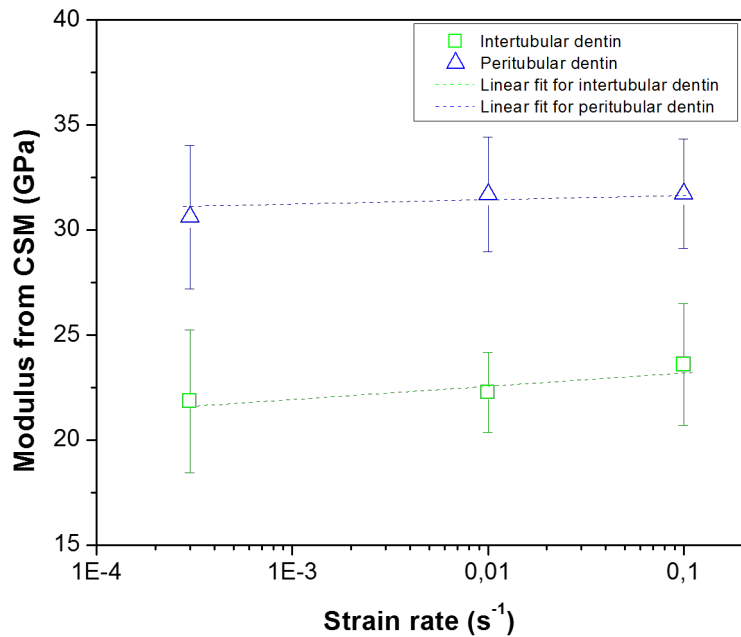


Figure 4.11 – Strain-rate sensitivity for peri and intertubular dentins.

4.3 Summary of micro-scale mechanical characterization

The micro-scale elastic modulus for both peri and intertubular dentins were measured by nanoindentation tests. The indentation behavior of both components (peri and intertubular dentin) shows typical nonlinear behavior for loading process caused by the simultaneous contributions of elastic and plastic deformations. At the beginning of the unload, the elastic recovery of the indentation leads a linear response from which the elastic modulus can be

deduced, assuming a given Poisson's ratio.

The extremely limited indentation depth (200nm) makes difficult of the localization of the indents, so AFM imaging are performed. Both dynamic CSM method and the unload method exhibit the same trend for the elastic moduli in the two dentin components. Peritubular dentin has higher elastic modulus (26.7GPa with a standard deviation of 3.1GPa) than intertubular dentin (16.2GPa with a standard deviation of 5.5GPa). Associated with the ratio of each components, mixture law provided an estimation for the macro-scale elastic modulus, comparable with our previous compression results.

Creep behavior of the dentin was also evaluated and modeled by a four elements Burger model. The parameters from the creep model indicates that dentin has a more elastic than viscous behavior. Limited strain rate dependency was found in the range from 0.0003 to $0.1 s^{-1}$.

CONCLUSION AND PERSPECTIVES

Dentin is an inhomogeneous, hierarchical biological material. From a structural point of view, it is a three-phase porous material made of a mixture of mineral crystals, collagen fibers and water. These structures are hierarchically organized, and determine its mechanical properties at all scales. We investigated the multi-scale mechanical behavior of human dentin. In this chapter, a conclusion is summarizing all our results. Then, some preliminary results are used as a perspective. Knowledge of intact dentin's geometrical structures and mechanical properties is essential to understand the effects of the restorative dental procedures.

5.1 Conclusion

Several techniques (Micro-CT, Light optical microscope, confocal microscope, ESEM, FIB-SEM and etc.) were used to observed the dentin structure. None of the techniques is optimal: each has its own advantages and drawbacks. Combined protocols provide more possibilities of more detailed observations.

For the mechanical test, an integrated system was developed which control simultaneously the humidity and the temperature of the environment around a compression setup, while being

equipped to measure accurately the strain through real-time DIC. Noise error of the system limited in the level of $\mu\varepsilon$, mostly thanks to the auto-focus function. Compression tests on human dentin were conducted within this system. The elastic modulus of human dentin at macro-scale was determined to be 16.7GPa with a standard deviation of 5.1GPa, and the Poisson's ratio was found to be 0.31. The dilatation due to relative humidity change was investigated, showing a strong effect of the humidity. Surprisingly, a negative temperature expansion response was found. However, the elastic moduli are little influenced by the relative humidity or temperature. Knowledge of the dentin behavior influenced by the external conditions may provide substantial suggestions for the improvement of dental restoration procedures.

Other approaches were tested (RUS and integrated three point bending test in the appendix) for the macroscopic mechanical characterization. RUS assay provides all the elastic coefficient within one single test. The results show that the elastic moduli of human dentin present slight transverse isotropic characteristics ($E_1 = 23.01\text{GPa}$ and $E_3 = 23.32\text{GPa}$) and strongly anisotropic Poisson's ratio ($\nu_{12} = 0.47$ and $\nu_{31} = 0.30$). However, the obtained results are comparable with the compression tests, in which the determination of elastic modulus is likely to be more sensitive to the micro-drawbacks (ex. crack).

The micro-scale elastic properties of peri and intertubular dentins were measured by nanoindentation tests. The elastic moduli were determined by both CSM and unloading methods, with coherent results. They show two different populations, which were attributed to inter- and peritubular dentin. The location of each indent was determined on AFM images. Peritubular dentin has a higher elastic modulus (26.7GPa with a standard deviation of 3.1GPa) than intertubular dentin (16.2GPa with a standard deviation of 5.5GPa). Using the ratio of each components, the mixture law provided an estimation for the macro-scale elastic modulus, comparable with our compression results on the same samples.

Creep behavior of the dentin was also measured and modeled by a Burger model. It appears that dentin is finally mostly elastic. Limited strain rate dependency was found in the test (strain

rate ranging from 0.0003 to $0.1s^{-1}$).

In this work, a morphological and mechanical study of the dentin tissue has been performed. Four observation techniques (*mu*CT, optical microscope, ESEM and confocal microscope) have been used and compared. Particularly, 3D visualization of dentin porous tissue was firstly achieved by confocal microscopy in the area near DEJ. Tubules show a more complex tree structure than the Y-shaped deduced from 2D observations. More realistic modeling considering the complex porous structure may be realized with the help of confocal microscopy. Some preliminary results are presented in the perspective. Besides, the surprising dilatation behavior of human dentin due to relative humidity was also observed in this work. This knowledge may provide substantial suggestions in order to improve the dentin restoration process.

5.2 Perspectives

5.2.1 Microscale observations and mechanical characterization by AFM

Nanoindentation has the drawback of a lack of immediate possibility of the localization of the indents. Blind indentation tests will lead large number of undesirable assays. The AFM has the ability to *in-situ* image the components of peri and intertubular dentin, but also to measure the mechanical elastic modulus. A commercial method like *PeakForce Quantitative Nanoscale Mechanical Characterization (QNM) mode* in the AFM could lead to such a measurements. Preliminary results carried on porcine dentin are presented in [Fig. 5.1](#).

The elastic modulus of each component is obtained by averaging the values of each components (see [Fig. 5.2](#)). In this preliminary assay on porcine dentin, the average modulus of peri and intertubular dentin were found to be 20.4GPa and 16.4GPa, respectively. Further tests should be continued to human dentin and the external environment should be controlled.

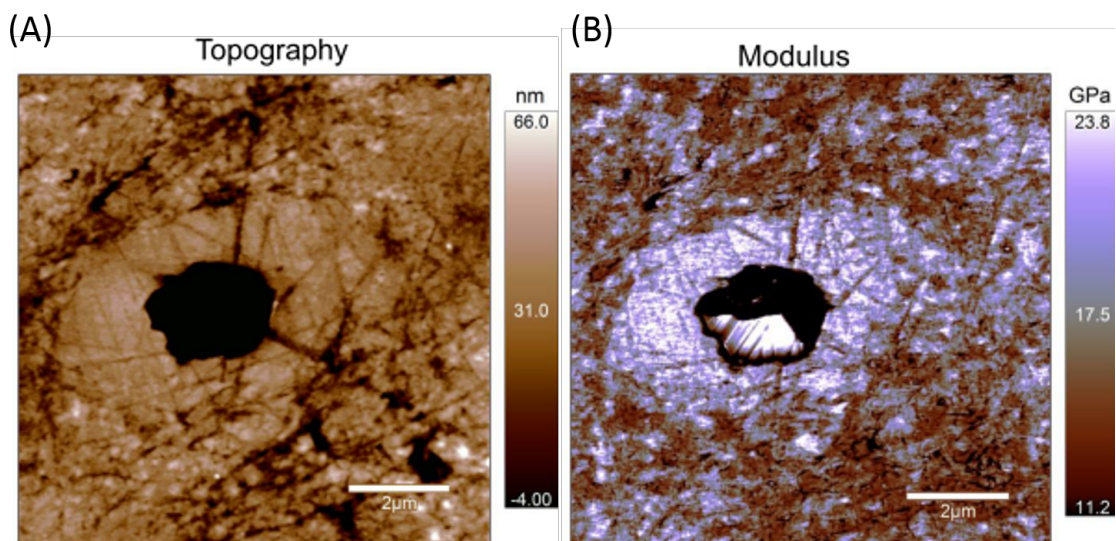


Figure 5.1 – Two AFM images with different modes on porcine dentin. (A) Topography image under contact mode; (B) Modulus map under PeakForce QNM mode.

One drawback is the difficulty to have really quantitative measures of the moduli by AFM: it requests a very careful calibration of the properties of the probe, and even this is not always sufficient to have more than the order of magnitude of the moduli. But still, comparison between different components remains accurate.

5.2.2 3D visualization with FIB-SEM

In SEM, imaging improved detectors like circular backscatter detector (CBS), allow to see with a high resolution all the components of the dentin, but only on the surface (see Fig. 5.3). The peri and intertubular dentins have a significant difference. This could be an interesting tool for microstructure observations.

Furthermore, with the use of focused ion beam (FIB), the sample can be etched layer by layer. Then, the resulting images can be stacked together to recreate the 3D micro-structure. Due to the high resolution of the FIB (several nanometers) and the SEM, the acquired 3D structure will have much more details than those obtained from other techniques (such as confocal microscopy). An example of a created mesh based on a FIB-SEM stack is shown

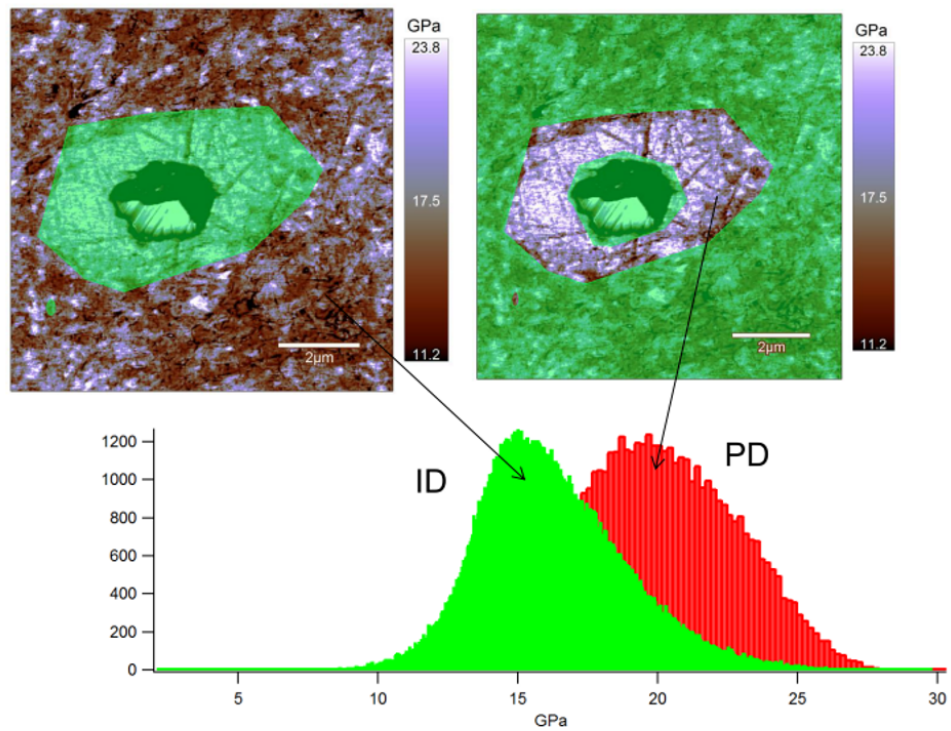


Figure 5.2 – Mechanical map measurement, used to define the peri and intertubular dentin modulus.

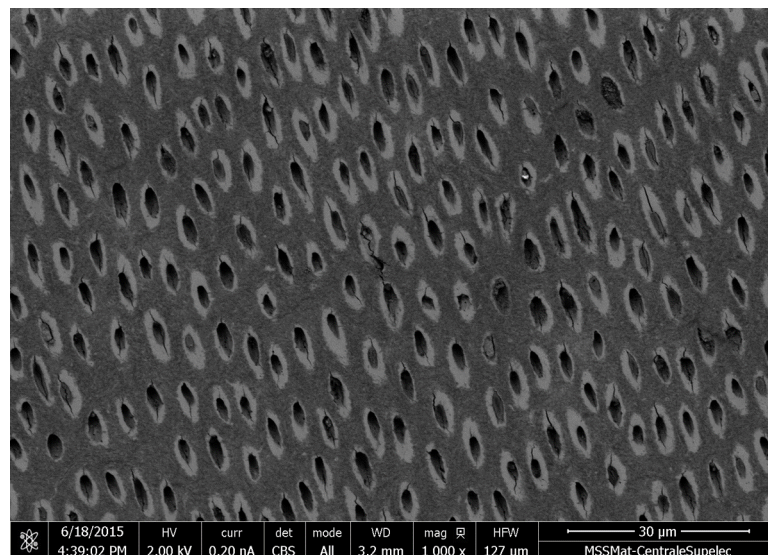


Figure 5.3 – SEM Image with CBS detector of human dentin. The three components of dentin (tubules, peri and tubular dentin) can be easily identified.

in Fig. 5.4. However, a longer scanning time is needed to observe a sufficient volume. For example, more than 72 hours would be need for a volume dimension of $80 \times 80 \times 20 \mu m^3$.

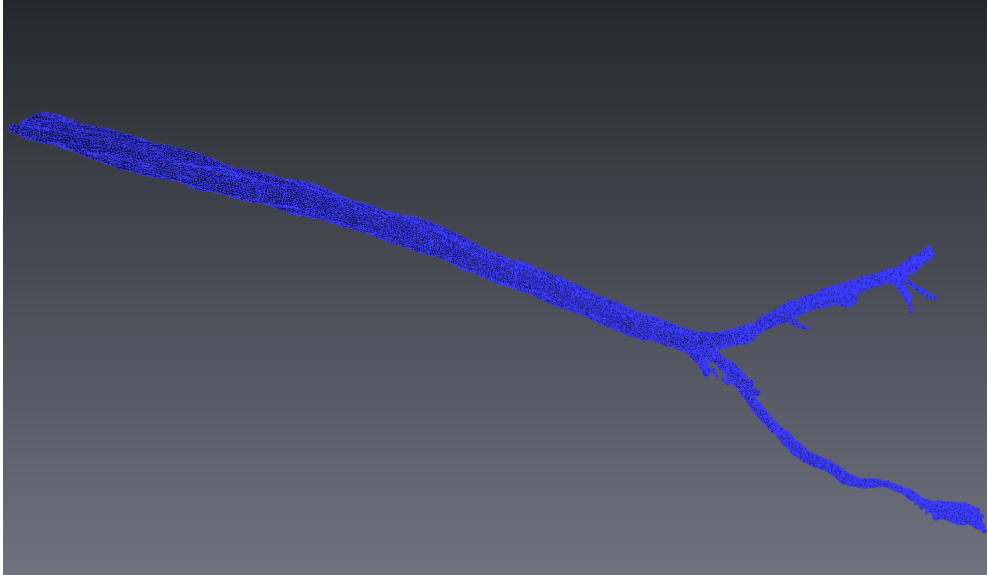


Figure 5.4 – A finite element model of the tubules near DEJ based on FIB-SEM observations.

5.2.3 FEM modeling

The porous structures of dentin are very small, which bring the difficulty for their 3D visualization. They have also a much complex organization than the usual picture of hollow cylinders surrounded by cylindrical inclusions embedded in a soft matrix. An implicit model based on confocal microscope images could be used as a valid first trial to develop a robust multi-scale model of dentin. Several critical points have to be kept in mind, among which we found the following ones.

RVE determination

In the theory of composite materials, the representative volume element (RVE) is the smallest volume over which a measurement can be made that will yield a value representative of the whole [Hill, 1963]. For the volumes that are smaller than the RVE, a representative property

cannot be defined. The RVE of dentin can be determined from porosity and elastic modulus based on 3D image stack constructions taken from the confocal microscope.

An implicit model was built using confocal microscope within the area of mantle dentin (as in [Sec. 2.4](#)). An image volume of $387.07\mu\text{m} \times 325.08\mu\text{m} \times 35.7\mu\text{m}$ was used to build the 3D finite element model. The image resolution is around $189\text{nm} \times 189\text{nm} \times 350\text{nm}$, sufficient to measure the geometry of tubules larger than $2 - 3\mu\text{m}$. Based on the grey level of each pixel in the images obtained from the confocal microscope, an implicit model can be constructed considering both the peritubular dentin and intertubular dentin components.

[Fig. 5.5](#) shows an example of the construction of the implicit model. The confocal images were stacked together to recreate the 3D structure. Based on the binary image, the material properties of both peritubular dentin and intertubular dentin can be set considering the grid data of the image. The diameter of the peritubular dentin was assumed to be $3.2\mu\text{m}$ for all the branches. A 3D and plan modulus map shows the bundles of hollow tubules (modulus for tubules was set as 100Pa) surrounded by the peritubular dentin inclusions. The matrix part is the intertubular dentin. The mechanical parameters used in the implicit model were listed in [Table 5.1](#).

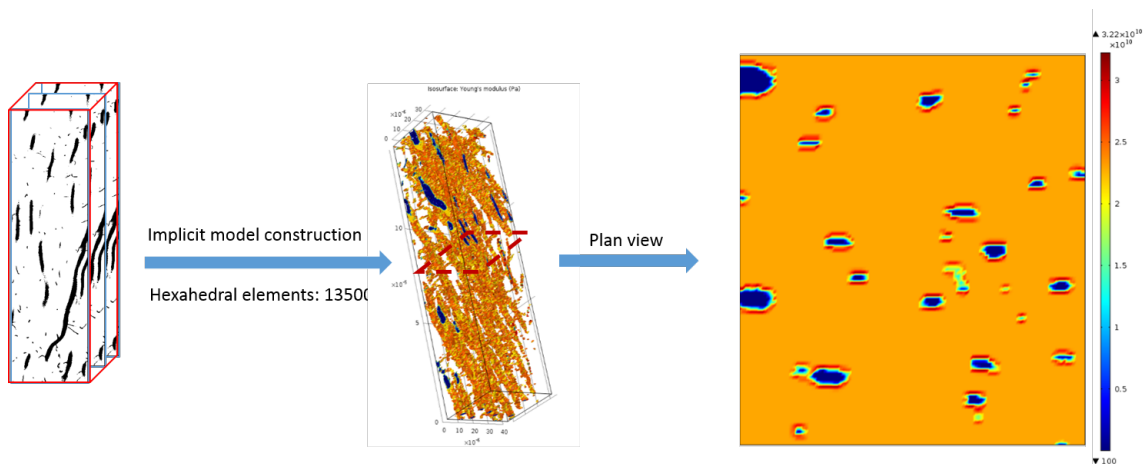


Figure 5.5 – An example of the construction of the implicit model, starting from the confocal images (left), in which the two components of peri and intertubular dentin are considered simultaneously.

A RVE was determined by looking at the porosity and the apparent modulus in a series

Table 5.1 – Parameters used in the implicit model

Parameters	Implicit model	Reference
D_p	$3.2 \mu m$	$1.27-3.95 \mu m$ [Dutra-Correa et al., 2007]
E_p	32.3 GPa	30-42 GPa [Williams et al., 2015]
E_i	22.9 GPa	15-23 GPa [Kinney et al., 2003]
Mesh	Hexahedron(7514 – 55539)	-

Note: D_p means peritubular dentin diameter

of increasing volumes (see Fig. 5.6): results are shown in Fig. 5.7. With the increase of the tested volume, the apparent modulus follows well the porosity. A RVE was determined as a volume of $4100 \mu m^3$ for a porosity around $5 \pm 0.6\%$. The apparent modulus for a RVE of dentin was found at 21.83 ± 0.16 GPa. The Voigt boundary has an average modulus of 22.63 GPa.

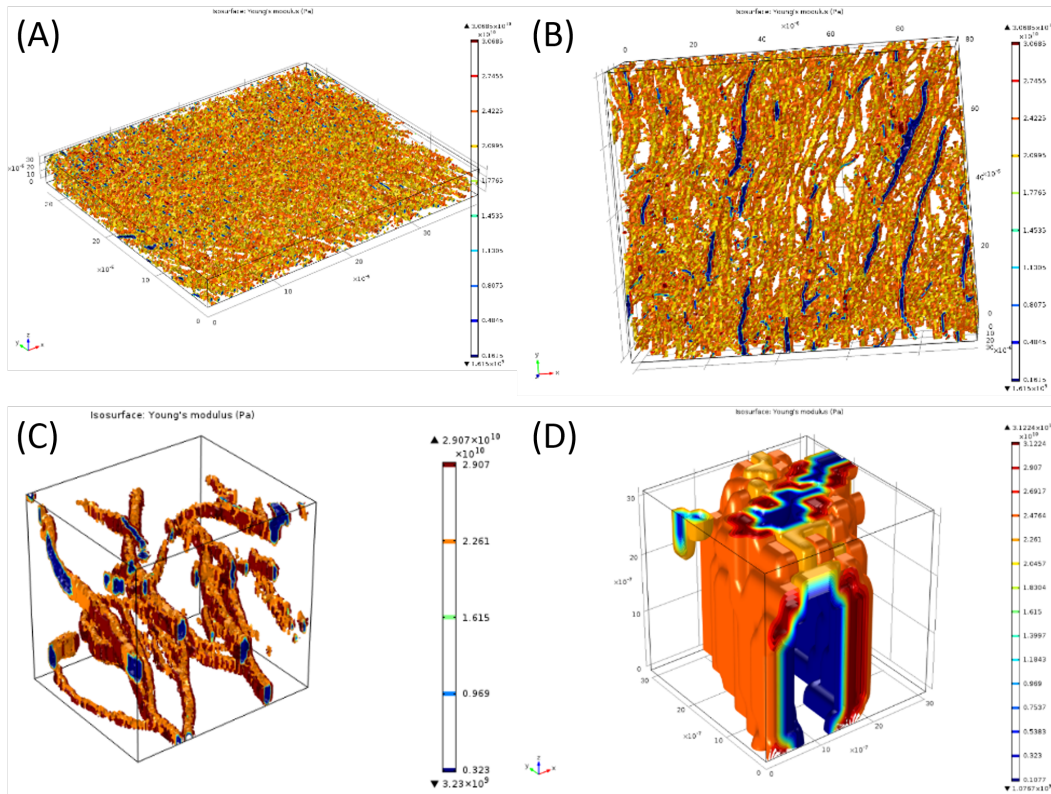


Figure 5.6 – Typical modulus plot for different selected volumes. (A) $387 \mu m \times 387 \mu m \times 36 \mu m$ (B) $96 \mu m \times 81 \mu m \times 36 \mu m$ (C) $24 \mu m \times 20 \mu m \times 24 \mu m$ (D) $3 \mu m \times 3 \mu m \times 3 \mu m$.

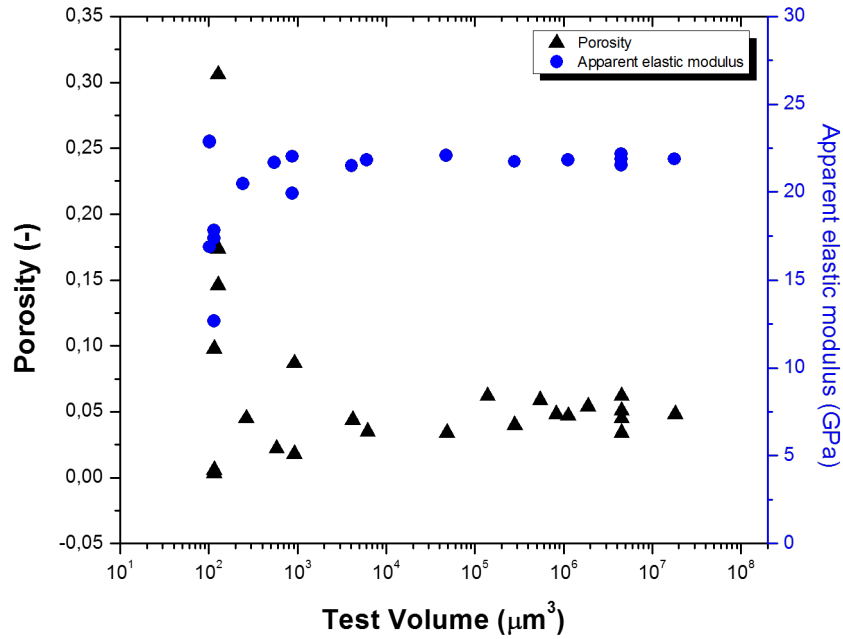


Figure 5.7 – Porosity and apparent modulus evolution with the tested volume. Below RVE, the dispersion increased dramatically

A comparison between the experimental and numerical results is shown on [Table 5.2](#): the implicit model gives an apparent modulus close to the experimental results. Preliminary results show then the possibility to model dentin based on confocal microscope images. Further work would be to combine the experimental results and simulation results for one sample. It would also be interesting to study the other regions of the dentin, different from the DEJ surroundings, to have an idea of the heterogeneities inside dentin.

Table 5.2 – Comparison between numerical and experimental results.

	E_{exp} (GPa)	E_{num}	RVE (μm^3)	RVE porosity
Dentin	21.23 (1.91)	21.83 (0.16)	4076	0.050 (0.006)

* Note: 1. E_{exp} means modulus from experiments and E_{num} means the modulus from implicit model.

2. The value inside bracket means the standard deviation.

3. Simulation without humidity condition.

Effect of the tubules geometry

As mentioned in the chapter 2, the 3D visualization of tubules shows that they have a complex shape rather than a simple hollow cylinder. The associate peritubular dentin has to follow the same shape. Thus, an interesting issue arises: is the apparent modulus influenced by the geometry of the tubules or not. Some preliminary finite element analysis is presented hereafter. Tubule shape is approximated by a sinus near the DEJ area. The amplitude and the period were measured from 5 isolated tubules on 3D confocal images. The average amplitude was $1.25\mu m$ (S.D. $0.71\mu m$). The mean period was $32.12\mu m$ (S.D. $9.27\mu m$). Based on these average values, three tubule shapes were considered.

A. Geometry constructions

We first assume a sinus function for the tubule shape. It is written as:

$$F(x) = 1.25\sin(0.2x) \quad (5.1)$$

The second geometry assumes a helix function, which is described as:

$$x(t) = 1.25\sin(0.2t) \quad (5.2)$$

$$y(t) = 1.25\cos(0.2t) \quad (5.3)$$

$$z(t) = t \quad (5.4)$$

In third we considered a two sinus function with mirror symmetric orientations following two equations for the two tubules:

$$F_1(x) = 1.25\sin(0.2x) \quad (5.5)$$

$$F_2(x) = -1.25\sin(0.2x) + 6.5 \quad (5.6)$$

The used parameters are listed in [Table 5.3](#), and the model are shown in [Fig. 5.8](#).

A FEM mesh was created with quadratic tetrahedrons. Peritubular and intertubular dentin were described as linear isotropic materials with a Young's modulus of 32 GPa and 22 GPa

Table 5.3 – Geometrical parameters used for the finite element model

Parameters	Used	Reference
D_t	$1.9 \mu m$	$0.8 - 2.5 \mu m$
$d_{interval}$	$6.5 \mu m$	$5.5 - 8.4 \mu m$
D_p	$3.2 \mu m$	$1.27 - 3.95 \mu m$
E_p	32.3 GPa	$30 - 42 \text{ GPa}$
E_i	22.9 GPa	$15 - 23 \text{ GPa}$

D_t, D_p : diameters of tubules and peritubular dentin; $d_{interval}$: distance between the tubules;

E_p, E_i : elastic modulus of peri and intertubular dentin;

References used are from [Garberoglio & Brännström, 1976; Marshall et al., 1997; Williams et al., 2015].

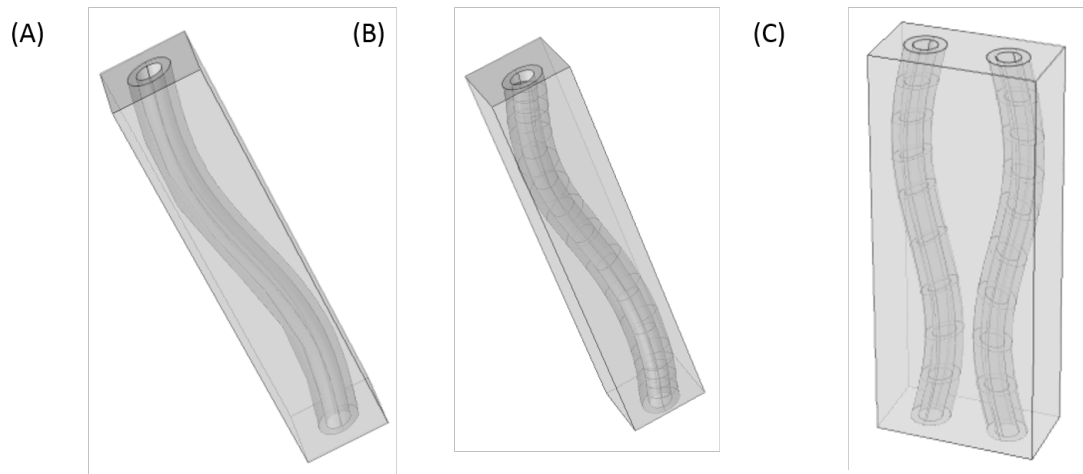


Figure 5.8 – Geometries used for the FEM model of three kinds of tubule shapes. (A) Sinusoidal tubule; (B) helical shape geometry; (C) Two symmetrical sinusoidal shape.

respectively, and a Poisson's ratio of 0.3. Top and bottom surfaces were subjected a compression: their vertical displacements were imposed (0 at the bottom ($\mathbf{n} \cdot \mathbf{u} = 0$), $-1 \mu m$ on the top $w = -1 \mu m$), while the transverse displacements remained free. Inner surfaces of the tubules were free. Two boundary conditions were tested respectively: free boundary conditions (BC1) on the whole domain and free boundary conditions combined with periodic boundary conditions ($u(x + L) = u(x)$) imposed on the lateral surfaces of the domain (BC2). For BC1, the equations were written as:

$$\int v dS = 0 \quad (5.7)$$

$$\int u dS = 0 \quad (5.8)$$

$$\int (xv - uy) dS = 0 \quad (5.9)$$

where \mathbf{u} is the displacement vector, which can be described as: $\mathbf{u} = ue_x + ve_y + we_z$ (with (e_x, e_y, e_z) : an orthonormal basis) and x, y and z are independent space variables.

B. Results

The obtained apparent moduli from the FEM simulations are listed in the [Table 5.4](#). With the compression boundary condition (BC1), the geometry of tubules had almost no influence for the apparent modulus. The periodic boundary condition (BC2) leads to an increase of the apparent moduli with respect to the boundary condition BC1. The geometry has little influence apart from the two mirror shape sinusoidal tubules which showed a lower apparent modulus. This indicates that there should be a strong influence of the interactions between the tubules. Thus, further model focusing on the interaction between the tubules should be investigated.

To conclude, in this perspective part, we have presented few complementary experimental technique that seems promising: AFM and FIB-SEM. We also presented a first attempt to model the mechanical behavior of the dentinal tissue based on CLSM imaging that leads to interesting perspectives. One may notice that the thermal behavior should also be investigated

Table 5.4 – Apparent moduli obtained from FEM simulations with different tubule shapes and boundary conditions.

Tubules geometry	E_{app} with BC1 (GPa)	E_{app} with BC2 (GPa)
Cylinder	22.52	29.35
Sinus	22.40	29.26
Helix	22.31	29.11
Two mirror sinus	22.46	24.42

BC1: free boundary condition; BC2: periodic boundary condition.

and compared with our experimental results. A multi-scale morphological and mechanical study of the dentinal tissue has been led here and open a lot of promising experimental and numerical perspectives.

BIBLIOGRAPHY

- Abramowitz, M., & Davidson, M. (2007). Introduction to microscopy. *Molecular Expressions*, (pp. 08–22). Cited on page(s) 42.
- Allais, L., Bornert, M., Bretheau, T., & Caldemaison, D. (1994). Experimental characterization of the local strain field in a heterogeneous elastoplastic material. *Acta Metallurgica et materialia*, 42, 3865–3880. Cited on page(s) 27, 31, 32.
- Anderson, D. (1956). Measurement of stress in mastication. *J Dent Res*, 35, 664–670. Cited on page(s) 22.
- Angker, L., Nockolds, C., Swain, M. V., & Kilpatrick, N. (2004). Correlating the mechanical properties to the mineral content of carious dentine—a comparative study using an ultra-micro indentation system (umis) and sem-bse signals. *Archives of Oral Biology*, 49, 369–378. Cited on page(s) 23, 24, 26.
- Arola, D., & Reprogl, R. (2005). Effects of aging on the mechanical behavior of human dentin. *Biomaterials*, 26, 4051–4061. Cited on page(s) 21.
- Arola, D. D., & Reprogl, R. K. (2006). Tubule orientation and the fatigue strength of human dentin. *Biomaterials*, 27, 2131–2140. Cited on page(s) 21.
- Avery, J. K., & Steele, P. F. (2006). *Essentials of oral histology and embryology: a clinical approach*. Mosby. Cited on page(s) 13, 14, 16.
- Balooch, G., Marshall, G., Marshall, S., Warren, O., Asif, S. S., & Balooch, M. (2004). Evaluation of a new modulus mapping technique to investigate microstructural features of human teeth. *Journal of biomechanics*, 37, 1223–1232. Cited on page(s) 24, 26, 49.

Bibliography

- Bastawros, A., Bart-Smith, H., & Evans, A. (2000). Experimental analysis of deformation mechanisms in a closed-cell aluminum alloy foam. *Journal of the Mechanics and Physics of Solids*, *48*, 301–322. Cited on page(s) 27.
- Berkovitz, B. K., Holland, G. R., & Moxham, B. J. (2009). *Oral anatomy, histology and embryology*. Mosby. Cited on page(s) 9.
- Bernard, S., Grimal, Q., & Laugier, P. (2014). Resonant ultrasound spectroscopy for viscoelastic characterization of anisotropic attenuative solid materials. *The Journal of the Acoustical Society of America*, *135*, 2601–2613. Cited on page(s) 85, 86.
- Bertassoni, L. E., Stankoska, K., & Swain, M. V. (2012). Insights into the structure and composition of the peritubular dentin organic matrix and the lamina limitans. *Micron*, *43*, 229–236. Cited on page(s) 49.
- Bonfield, W., & Datta, P. (1974). Young's modulus of compact bone. *Journal of biomechanics*, *7*, 147–149. Cited on page(s) 164.
- Bornert, M., Brémand, F., Doumalin, P., Dupré, J.-C., Fazzini, M., Grédiac, M., Hild, F., Mistou, S., Molimard, J., Orteu, J.-J. et al. (2009). Assessment of digital image correlation measurement errors: methodology and results. *Experimental mechanics*, *49*, 353–370. Cited on page(s) 27, 32.
- Boskey, A. L. (2007). Mineralization of bones and teeth. *Elements*, *3*, 385–391. Cited on page(s) 11.
- Boushell, L. W., & Sturdevant, J. R. (2014). Clinical significance of dental anatomy, histology, physiology, and occlusion. *Sturdevant's Art & Science of Operative Dentistry*, (pp. 1–40). Cited on page(s) 7, 8, 9, 12, 15.
- Bowen, R., & Rodriguez, M. S. (1962). Tensile strength and modulus of elasticity of tooth structure and several restorative materials. *The Journal of the American Dental Association*, *64*, 378–387. Cited on page(s) 18, 21, 166, 167.
- Boyde, A., Ali, N., & Jones, S. (1984). Resorption of dentine by isolated osteoclasts in vitro. *British dental journal*, *156*, 216–220. Cited on page(s) 10.

- Brännström, M., & Garberoglio, R. (1972). The dentinal tubules and the odontoblast processes a scanning electron microscopic study. *Acta Odontologica*, *30*, 291–311. Cited on page(s) 8.
- Brown, W., Jacobs, H., & Thompson, R. (1972). Thermal fatigue in teeth. *Journal of dental research*, *51*, 461–467. Cited on page(s) 84.
- Burrow, M., Taniguchi, Y., Nikaido, T., Satoh, M., Inai, N., Tagami, J., & Takatsu, T. (1995). Influence of temperature and relative humidity on early bond strengths to dentine. *Journal of dentistry*, *23*, 41–45. Cited on page(s) 22, 59, 81.
- Carter, D. R., & Hayes, W. C. (1977). The compressive behavior of bone as a two-phase porous structure. *The Journal of Bone & Joint Surgery*, *59*, 954–962. Cited on page(s) 167.
- Cate-Ten, A. (1998). Oral histology: development, structure, and function. Cited on page(s) 4, 5.
- Chen, X., & Vlassak, J. J. (2001). Numerical study on the measurement of thin film mechanical properties by means of nanoindentation. *Journal of Materials Research*, *16*, 2974–2982. Cited on page(s) 98.
- Chien, H.-L., Chiu, P.-J., Huang, B.-W., & Kuang, J.-H. (2012). Young's moduli of human tooth measured using micro-indentation tests. *Life Science Journal*, *9*, 172–177. Cited on page(s) 23.
- Choi, S., & Shah, S. (1997). Measurement of deformations on concrete subjected to compression using image correlation. *Experimental Mechanics*, *37*, 307–313. Cited on page(s) 67.
- Chu, T., Ranson, W., & Sutton, M. (1985). Applications of digital-image-correlation techniques to experimental mechanics. *Experimental mechanics*, *25*, 232–244. Cited on page(s) 27.
- Craig, R., & Peyton, F. (1958). Elastic and mechanical properties of human dentin. *J dent Res*, *37*, 710–718. Cited on page(s) 18, 21.
- Currey, J. D. (1964). Three analogies to explain the mechanical properties of bone. *Biorheology*, *2*, 1–10. Cited on page(s) 92.
- Davis, J. R. (2001). *Alloying: understanding the basics*. ASM international. Cited on page(s) 81.
- Davis, J. R. (2004). *Tensile testing*. ASM international. Cited on page(s) 62.

Bibliography

- Donald, A. M. (2003). The use of environmental scanning electron microscopy for imaging wet and insulating materials. *Nature materials*, 2, 511–516. Cited on page(s) 43.
- Dougherty, R., & Kunzelmann, K.-H. (2007). Computing local thickness of 3d structures with imagej. *Microscopy and Microanalysis*, 13, 1678–1679. Cited on page(s) 50.
- Doumalin, P. (2000). *Microextensometrie locale par correlation d'images numeriques application aux etudes micromecaniques par microscopie electronique a balayage*. Ph.D. thesis. Cited on page(s) 28, 29.
- Doumalin, P., & Bornert, M. (2000). Micromechanical applications of digital image correlation techniques. In *Interferometry in Speckle Light* (pp. 67–74). Springer. Cited on page(s) 27.
- Dourda, A., Moule, A., & Young, W. (1994). A morphometric analysis of the cross-sectional area of dentine occupied by dentinal tubules in human third molar teeth. *International endodontic journal*, 27, 184–189. Cited on page(s) 8.
- Dutra-Correa, M., Anauate-Netto, C., & Arana-Chavez, V. E. (2007). Density and diameter of dentinal tubules in etched and non-etched bovine dentine examined by scanning electron microscopy. *archives of oral biology*, 52, 850–855. Cited on page(s) 114.
- El Kirat, K., Morandat, S., & Dufrière, Y. F. (2010). Nanoscale analysis of supported lipid bilayers using atomic force microscopy. *Biochimica et Biophysica Acta (BBA)-Biomembranes*, 1798, 750–765. Cited on page(s) 93.
- El Mowafy, O., & Watts, D. (1986). Fracture toughness of human dentin. *Journal of dental research*, 65, 677–681. Cited on page(s) 20.
- Eltit, F., Ebacher, V., & Wang, R. (2013). Inelastic deformation and microcracking process in human dentin. *Journal of structural biology*, 183, 141–148. Cited on page(s) 21, 157, 158, 160, 163, 166.
- Fehrenbach, M. J., & Popowics, T. (2015). *Illustrated dental embryology, histology, and anatomy*. Elsevier Health Sciences. Cited on page(s) 5.
- Fischer-Cripps, A. (2004). A simple phenomenological approach to nanoindentation creep. *Materials Science and Engineering: A*, 385, 74–82. Cited on page(s) 102, 103.

- Fischer-Cripps, A., & Nicholson, D. (2004). Nanoindentation. mechanical engineering series. *Applied Mechanics Reviews*, 57, 12. Cited on page(s) 103.
- Forien, J.-B., Fleck, C., Cloetens, P., Duda, G. N., Fratzi, P., Zolotoyabko, E., & Zaslansky, P. (2015). Compressive residual strains in mineral nanoparticles as a possible origin of enhanced crack resistance in human tooth dentin. *Nano letters*, . Cited on page(s) 10, 11.
- Forien, J.-B., Zizak, I., Fleck, C., Petersen, A., Fratzi, P., Zolotoyabko, E., & Zaslansky, P. (2016). Water-mediated collagen and mineral nanoparticle interactions guide functional deformation of human tooth dentin. *Chemistry of Materials*, 28, 3416–3427. Cited on page(s) 60, 80, 82, 84.
- Garberoglio, R., & Brännström, M. (1976). Scanning electron microscopic investigation of human dentinal tubules. *Archives of Oral Biology*, 21, 355–362. Cited on page(s) 8, 117, 167.
- Gaucher, E., Robelin, C., Matray, J., Negrel, G., Gros, Y., Heitz, J., Vinsot, A., Rebours, H., Casagagnabere, A., & Bouchet, A. (2004). Andra underground research laboratory: interpretation of the mineralogical and geochemical data acquired in the callovian–oxfordian formation by investigative drilling. *Physics and Chemistry of the Earth, Parts A/B/C*, 29, 55–77. Cited on page(s) 61.
- Gaye, A. (2015). *Analyse multiéchelle des mécanismes de déformation du sel gemme par mesures de champs surfaciques et volumiques*. Ph.D. thesis Paris Est. Cited on page(s) 30.
- Germaneau, A. (2007). *Developpement de techniques de mesure dans le volume, photoélasticimétrie 3D par découpage optique et corrélation volumique par tomographie optique et rayons X: application à l'étude des effets mécaniques 3D dans les structures et les biomatériaux*. Ph.D. thesis Poitiers. Cited on page(s) 30.
- Goddard Iii, W. A., Brenner, D., Lyshevski, S. E., & Iafrate, G. J. (2007). *Handbook of nanoscience, engineering, and technology*. CRC press. Cited on page(s) 93.
- Gotliv, B.-A., & Veis, A. (2007). Peritubular dentin, a vertebrate apatitic mineralized tissue without collagen: role of a phospholipid-proteolipid complex. *Calcified tissue international*, 81, 191–205. Cited on page(s) 10.

- Grimal, Q., Raum, K., Gerisch, A., & Laugier, P. (2011). A determination of the minimum sizes of representative volume elements for the prediction of cortical bone elastic properties. *Biomechanics and modeling in mechanobiology*, *10*, 925–937. Cited on page(s) 25.
- Han, C.-F., Wu, B.-H., Chung, C.-J., Chuang, S.-F., Li, W.-L., & Lin, J.-F. (2012). Stress–strain analysis for evaluating the effect of the orientation of dentin tubules on their mechanical properties and deformation behavior. *Journal of the mechanical behavior of biomedical materials*, *12*, 1–8. Cited on page(s) 24, 26.
- Hand, A. R., & Frank, M. E. (2014). *Fundamentals of Oral Histology and Physiology*. John Wiley & Sons. Cited on page(s) 13.
- Heintzmann, R., & Ficz, G. (2006). Breaking the resolution limit in light microscopy. *Briefings in functional genomics & proteomics*, *5*, 289–301. Cited on page(s) 42.
- Hengchang, X., Wenyi, L., & Tong, W. (1989). Measurement of thermal expansion coefficient of human teeth. *Australian dental journal*, *34*, 530–535. Cited on page(s) 59, 82.
- Hild, F., & Roux, S. (2008). Correliq4: A software for finite element displacement field measurements by digital image correlation. *Rapport interne LMT Cachan*, 269. Cited on page(s) 161.
- Hildebrand, T., & Rüegsegger, P. (1997). A new method for the model-independent assessment of thickness in three-dimensional images. *Journal of microscopy*, *185*, 67–75. Cited on page(s) 50.
- Hill, R. (1963). Elastic properties of reinforced solids: some theoretical principles. *Journal of the Mechanics and Physics of Solids*, *11*, 357–372. Cited on page(s) 112.
- Huang, G. T. (2009). Pulp and dentin tissue engineering and regeneration: current progress. *Regenerative medicine*, *4*, 697–707. Cited on page(s) 11.
- Imbeni, V., Kruzic, J., Marshall, G., Marshall, S., & Ritchie, R. (2005). The dentin–enamel junction and the fracture of human teeth. *Nature materials*, *4*, 229–232. Cited on page(s) 23, 26, 49.
- Imbeni, V., Nalla, R., Bosi, C., Kinney, J., & Ritchie, R. (2003). In vitro fracture toughness of human dentin. *Journal of Biomedical Materials Research Part A*, *66*, 1–9. Cited on page(s) 20.

- Inada, H., Kakibayashi, H., Isakozawa, S., Hashimoto, T., Yaguchi, T., & Nakamura, K. (2009). Hitachi's development of cold-field emission scanning transmission electron microscopes. *Advances in Imaging and Electron Physics*, *159*, 123–186. Cited on page(s) 43.
- Isaksson, H., Nagao, S., MaŁkiewicz, M., Julkunen, P., Nowak, R., & Jurvelin, J. S. (2010). Precision of nanoindentation protocols for measurement of viscoelasticity in cortical and trabecular bone. *Journal of biomechanics*, *43*, 2410–2417. Cited on page(s) 103.
- Jantarat, J., Palamara, J. E., Lindner, C., & Messer, H. H. (2002). Time-dependent properties of human root dentin. *Dental materials*, *18*, 486–493. Cited on page(s) 19, 20, 72, 89, 165.
- Jaramillo Isaza, S. (2014). *Characterization of the mechanical and morphological properties of cortical bones by nanoindentation and Atomic Force Microscopy*. Ph.D. thesis Compiègne. Cited on page(s) 93.
- Johnson, C., Heiss, M., Kolar, L., & Luksha, L. (1998). Biology of the human dentition. *Illinois University, Chicago College of Dentistry*, . Cited on page(s) 5.
- Ketterl, W. (1961). The dentine in permanent human teeth. *Stoma*, *14*, 79–96. Cited on page(s) 8.
- Ketterl, W. (1983). Age-induced changes in the teeth and their attachment apparatus. *International dental journal*, *33*, 262–271. Cited on page(s) 14.
- Kinney, J., Balooch, M., Marshall, G., & Marshall, S. (1999). A micromechanics model of the elastic properties of human dentine. *Archives of oral Biology*, *44*, 813–822. Cited on page(s) 24, 26.
- Kinney, J., Balooch, M., Marshall, S., Marshall, G., & Weihs, T. (1996). Hardness and young's modulus of human peritubular and intertubular dentine. *Archives of Oral Biology*, *41*, 9–13. Cited on page(s) 23, 26, 167.
- Kinney, J., Gladden, J., Marshall, G. e. a., Marshall, S., So, J. H., & Maynard, J. (2004). Resonant ultrasound spectroscopy measurements of the elastic constants of human dentin. *Journal of biomechanics*, *37*, 437–441. Cited on page(s) 18, 20, 21, 87.

- Kinney, J., Marshall, S., & Marshall, G. (2003). The mechanical properties of human dentin: a critical review and re-evaluation of the dental literature. *Critical Reviews in Oral Biology & Medicine*, *14*, 13–29. Cited on page(s) [10](#), [18](#), [60](#), [81](#), [98](#), [114](#).
- Kinney, J., Pople, J., Marshall, G., & Marshall, S. (2001). Collagen orientation and crystallite size in human dentin: a small angle x-ray scattering study. *Calcified Tissue International*, *69*, 31–37. Cited on page(s) [10](#).
- Kishen, A., & Asundi, A. (2001). Investigations of thermal property gradients in the human dentine. *Journal of biomedical materials research*, *55*, 121–130. Cited on page(s) [59](#), [60](#), [82](#).
- Landis, W. J., & Silver, F. H. (2002). The structure and function of normally mineralizing avian tendons. *Comparative Biochemistry and Physiology Part A: Molecular & Integrative Physiology*, *133*, 1135–1157. Cited on page(s) [10](#).
- Lange, R., & Pfeiffer, P. (2009). Clinical evaluation of ceramic inlays compared to composite restorations. *Operative dentistry*, *34*, 263–272. Cited on page(s) [16](#).
- Langer, M. (2008). *Phase retrieval in the Fresnel region for hard X-ray tomography*. Ph.D. thesis Villeurbanne, INSA. Cited on page(s) [39](#).
- Lees, S., & Rollins, F. (1972). Anisotropy in hard dental tissues. *Journal of biomechanics*, *5*, 557–566. Cited on page(s) [18](#), [20](#), [21](#).
- LEIBA, R. (2014). Resonant ultrasound spectroscopy for arbitrarily shaped samples using finite element method and levenberg-marquart algorithm. *Proceedings of Acoustical Engineering Projects, 2014*, 26. Cited on page(s) .
- Leisure, R. G., & Willis, F. (1997). Resonant ultrasound spectroscopy. *Journal of Physics: Condensed Matter*, *9*, 6001. Cited on page(s) [85](#), [89](#).
- Li, X., & Bhushan, B. (2002). A review of nanoindentation continuous stiffness measurement technique and its applications. *Materials characterization*, *48*, 11–36. Cited on page(s) [34](#), [35](#).
- Lu, H., Vendroux, G., & Knauss, W. (1997). Surface deformation measurements of a cylindrical specimen by digital image correlation. *Experimental Mechanics*, *37*, 433–439. Cited on page(s) [27](#).

- Marshall, G., Balooch, M., Gallagher, R., Gansky, S., & Marshall, S. (2001). Mechanical properties of the dentinoenamel junction: Afm studies of nanohardness, elastic modulus, and fracture. *Journal of biomedical materials research*, *54*, 87–95. Cited on page(s) 24, 26, 49.
- Marshall, G. W., Marshall, S. J., Kinney, J. H., & Balooch, M. (1997). The dentin substrate: structure and properties related to bonding. *Journal of dentistry*, *25*, 441–458. Cited on page(s) 7, 8, 10, 21, 46, 117, 166, 167, 168.
- Marshall Jr, G. W. (1993). Dentin: Microstructure and characterization. *Quintessence International*, *24*. Cited on page(s) .
- McElhaney, J. H. (1966). Dynamic response of bone and muscle tissue. *Journal of applied physiology*, *21*, 1231–1236. Cited on page(s) 165.
- McGowan, D. M., Ambur, D. R., Hanna, T. G., & McNeill, S. R. (2001). Evaluating the compressive response of notched composite panels using full-field displacements. *Journal of aircraft*, *38*, 122–129. Cited on page(s) 27.
- Minsky, M. (1988). Memoir on inventing the confocal scanning microscope. *Scanning*, *10*, 128–138. Cited on page(s) 48.
- Mjör, I., & Nordahl, I. (1996). The density and branching of dentinal tubules in human teeth. *Archives of Oral Biology*, *41*, 401–412. Cited on page(s) 7, 8, 49, 52.
- Mjor, I. A., & Pindborg, J. J. (1973). *Histology of the human tooth*. Munksgaard. Cited on page(s) 8, 49, 52, 54.
- Nakabayashi, N., Kojima, K., & Masuhara, E. (1982). The promotion of adhesion by the infiltration of monomers into tooth substrates. *Journal of biomedical materials research*, *16*, 265–273. Cited on page(s) 5.
- Nalla, R., Imbeni, V., Kinney, J., Staninec, M., Marshall, S., & Ritchie, R. (2003). In vitro fatigue behavior of human dentin with implications for life prediction. *Journal of Biomedical Materials Research Part A*, *66*, 10–20. Cited on page(s) 22.

Bibliography

- Nalla, R., Porter, A., Daraio, C., Minor, A., Radmilovic, V., Stach, E., Tomsia, A., & Ritchie, R. (2005). Ultrastructural examination of dentin using focused ion-beam cross-sectioning and transmission electron microscopy. *Micron*, *36*, 672–680. Cited on page(s) 49.
- Nanci, A. (2008). Ten cate's oral histology: development, structure, and function. *St. Louis: Mosby Elsevier*, . Cited on page(s) 14.
- Nasse, M. J., Woehl, J. C., & Huant, S. (2007). High-resolution mapping of the three-dimensional point spread function in the near-focus region of a confocal microscope. *Applied physics letters*, *90*, 031106. Cited on page(s) 48.
- Neumann, H., & DrSalvo, N. (1957). Compression of teeth under, the load of chewing. *Journal of dental research*, *36*, 286–290. Cited on page(s) 21.
- Odegard, G., Clancy, T., & Gates, T. (2005). Modeling of the mechanical properties of nanoparticle/polymer composites. *Polymer*, *46*, 553–562. Cited on page(s) 34.
- Oliver, W. C., & Pharr, G. M. (1992). An improved technique for determining hardness and elastic modulus using load and displacement sensing indentation experiments. *Journal of materials research*, *7*, 1564–1583. Cited on page(s) 33, 34, 98.
- Oliver, W. C., & Pharr, G. M. (2004). Measurement of hardness and elastic modulus by instrumented indentation: Advances in understanding and refinements to methodology. *Journal of materials research*, *19*, 3–20. Cited on page(s) 34, 35, 36, 98.
- Palamara, J., Wilson, P., Thomas, C., & Messer, H. (2000). A new imaging technique for measuring the surface strains applied to dentine. *Journal of dentistry*, *28*, 141–146. Cited on page(s) 18, 19, 21, 166, 167.
- Pallesen, U., & Qvist, V. (2003). Composite resin fillings and inlays. an 11-year evaluation. *Clinical oral investigations*, *7*, 71–79. Cited on page(s) 5, 16.
- Pashley, D. H. (1989). Dentin: a dynamic substrate—a review. *Scanning microscopy*, *3*, 161–74. Cited on page(s) 8, 54, 55.

- Pawley, J., & Masters, B. R. (1996). Handbook of biological confocal microscopy. *Optical Engineering*, 35, 2765–2766. Cited on page(s) 47.
- Peters, W., & Ranson, W. (1982). Digital imaging techniques in experimental stress analysis. *Optical engineering*, 21, 213427–213427. Cited on page(s) 27.
- Peyton, F., Mahler, D., & Hershenov, B. (1952). Physical properties of dentin. *Journal of dental Research*, (pp. 366–70). Cited on page(s) 18, 21, 72.
- Pidaparti, R., Chandran, A., Takano, Y., & Turner, C. (1996). Bone mineral lies mainly outside collagen fibrils: predictions of a composite model for osternal bone. *Journal of biomechanics*, 29, 909–916. Cited on page(s) 10.
- Plasmans, P., Creugers, N., Hermsen, R., & Vrijhoef, M. (1994). Intraoral humidity during operative procedures. *Journal of dentistry*, 22, 89–91. Cited on page(s) 81.
- Plasmans, P., Creugers, N., Hermsen, R., & Vrijhoef, M. (1996). The influence of absolute humidity on shear bond adhesion. *Journal of dentistry*, 24, 425–428. Cited on page(s) 22, 59, 81.
- Plasmans, P., Reukers, E., Vollenbrock-Kuipers, L., & Vollenbrock, H. (1993). Air humidity: a detrimental factor in dentine adhesion. *Journal of dentistry*, 21, 228–233. Cited on page(s) 22, 59.
- Preibisch, S., Saalfeld, S., & Tomancak, P. (2009). Globally optimal stitching of tiled 3d microscopic image acquisitions. *Bioinformatics*, 25, 1463–1465. Cited on page(s) 45.
- Qin, Q.-H., & Swain, M. V. (2004). A micro-mechanics model of dentin mechanical properties. *Bio-materials*, 25, 5081–5090. Cited on page(s) 92.
- Rees, J., Jacobsen, P., & Hickman, J. (1994). The elastic modulus of dentine determined by static and dynamic methods. *Clinical materials*, 17, 11–15. Cited on page(s) 19, 21, 157, 158, 162, 166.
- Renson, C., & Braden, M. (1975). Experimental determination of the rigidity modulus, poisson's ratio and elastic limit in shear of human dentine. *Archives of oral biology*, 20, 43–IN5. Cited on page(s) 21.
- Roosen-Runge, E. C. (1976). Histology: A text and atlas. *Human Pathology*, 7, 485. Cited on page(s) 5.

Bibliography

- Ryou, H., Amin, N., Ross, A., Eidelman, N., Wang, D., Romberg, E., & Arola, D. (2011). Contributions of microstructure and chemical composition to the mechanical properties of dentin. *Journal of Materials Science: Materials in Medicine*, 22, 1127–1135. Cited on page(s) 19, 20.
- Ryou, H., Romberg, E., Pashley, D. H., Tay, F. R., & Arola, D. (2012). Nanoscopic dynamic mechanical properties of intertubular and peritubular dentin. *Journal of the mechanical behavior of biomedical materials*, 7, 3–16. Cited on page(s) 24, 26.
- Sano, H., Ciucchi, B., Matthews, W., & Pashley, D. (1994). Tensile properties of mineralized and demineralized human and bovine dentin. *Journal of Dental Research*, 73, 1205–1211. Cited on page(s) 18, 21, 166, 167.
- Saraiva, L. O., Aguiar, T. R., Costa, L., Cavalcanti, A. N., Giannini, M., & Mathias, P. (2015). Influence of intraoral temperature and relative humidity on the dentin bond strength: an in situ study. *Journal of Esthetic and Restorative Dentistry*, 27, 92–99. Cited on page(s) 81.
- Schilke, R., Lisson, J. A., Bauß, O., & Geurtsen, W. (2000). Comparison of the number and diameter of dentinal tubules in human and bovine dentine by scanning electron microscopic investigation. *Archives of Oral Biology*, 45, 355–361. Cited on page(s) 8.
- Schmid, B., Schindelin, J., Cardona, A., Longair, M., & Heisenberg, M. (2010). A high-level 3d visualization api for java and imagej. *BMC bioinformatics*, 11, 1. Cited on page(s) 50.
- Schreier, H. W., Braasch, J. R., & Sutton, M. A. (2000). Systematic errors in digital image correlation caused by intensity interpolation. *Optical engineering*, 39, 2915–2921. Cited on page(s) 27, 67.
- Scott, N., & Symons, N. (1967). *Introduction to dental anatomy*.: Churchill livingstone. Cited on page(s) 10.
- Semwogerere, D., & Weeks, E. R. (2005). Confocal microscopy. *Encyclopedia of Biomaterials and Biomedical Engineering*, (pp. 1–10). Cited on page(s) 48.
- Song, J.-M., Shen, Y.-L., Su, C.-W., Lai, Y.-S., & Chiu, Y.-T. (2009). Strain rate dependence on nanoindentation responses of interfacial intermetallic compounds in electronic solder joints with cu and ag substrates. *Materials transactions*, 50, 1231–1234. Cited on page(s) 103.

- Stanford, J. W., Weigel, K. V., Paffenbarger, G. C., & Sweeney, W. (1960). Compressive properties of hard tooth tissues and some restorative materials. *The Journal of the American Dental Association*, 60, 746–756. Cited on page(s) 18.
- Stappert, C. F., Att, W., Gerds, T., & Strub, J. R. (2006). Fracture resistance of different partial-coverage ceramic molar restorations: An in vitro investigation. *The Journal of the American Dental Association*, 137, 514–522. Cited on page(s) 15.
- Sutton, M. A., Chao, Y.-J., & Lyons, J. S. (1993). Computer vision methods for surface deformation measurements in fracture mechanics. *AM SOC MECH ENG APPL MECH DIV AMD, ASME, NEW YORK, NY,(USA), 1993,, 176*, 203–217. Cited on page(s) 27.
- Sutton, M. A., Orteu, J. J., & Schreier, H. (2009). *Image correlation for shape, motion and deformation measurements: basic concepts, theory and applications*. Springer Science & Business Media. Cited on page(s) 27.
- Sztefek, P., Vanleene, M., Olsson, R., Collinson, R., Pitsillides, A. A., & Shefelbine, S. (2010). Using digital image correlation to determine bone surface strains during loading and after adaptation of the mouse tibia. *Journal of biomechanics*, 43, 599–605. Cited on page(s) 27.
- Tong, W. (1997). Detection of plastic deformation patterns in a binary aluminum alloy. *Experimental Mechanics*, 37, 452–459. Cited on page(s) 27.
- den Toonder, J., Ramone, Y., Van Dijken, A., Beijer, J., & Zhang, G. (2005). Viscoelastic characterization of low-dielectric constant silk films using nanoindentation in combination with finite element modeling. *Journal of Electronic Packaging*, 127, 276–285. Cited on page(s) 33.
- Touloukian, Y. S. (1966). *Thermophysical Properties of High Temperature Solid Materials. Volume 4. Oxides and Their Solutions and Mixtures. Part I. Simple Oxygen Compounds and Their Mixtures*. Technical Report DTIC Document. Cited on page(s) 81.
- Touloukian, Y. S., Powell, R., Ho, C., & Nicolaou, M. (1974). *Thermophysical Properties of Matter- The TPRC Data Series. Volume 10. Thermal Diffusivity*. Technical Report DTIC Document. Cited on page(s) 81.

Bibliography

- TRONSTAD, L. (1973). Ultrastructural observations on human coronal dentin. *European Journal of Oral Sciences*, 81, 101–111. Cited on page(s) 8.
- Trowbridge, H. O. (2003). Pulp biology: progress during the past 25 years. *Australian Endodontic Journal*, 29, 5–12. Cited on page(s) 15.
- Van Nieuwenhuysen, J.-P., D'Hoore, W., Carvalho, J., & Qvist, V. (2003). Long-term evaluation of extensive restorations in permanent teeth. *Journal of dentistry*, 31, 395–405. Cited on page(s) 16.
- Vennat, E. (2009). Etude numérique et expérimentale de l'infiltration de la dentine déminéralisée en surface par des résines composites. *These de doctorat, École Centrale Paris, France*, . Cited on page(s) 10, 17.
- Vennat, E., Bogicevic, C., Fleureau, J.-M., & Degrange, M. (2009). Demineralized dentin 3d porosity and pore size distribution using mercury porosimetry. *dental materials*, 25, 729–735. Cited on page(s) 55.
- Verhulp, E., van Rietbergen, B., & Huiskes, R. (2004). A three-dimensional digital image correlation technique for strain measurements in microstructures. *Journal of biomechanics*, 37, 1313–1320. Cited on page(s) 27.
- Walker, M. P., Haj-Ali, R., Wang, Y., Hunziker, D., & Williams, K. B. (2006). Influence of environmental conditions on dental composite flexural properties. *Dental materials*, 22, 1002–1007. Cited on page(s) 22.
- Wang, L. (2012). *Micromechanical experimental investigation and modelling of strain and damage of argillaceous rocks under combined hydric and mechanical loads*. Ph.D. thesis Ecole Polytechnique X. Cited on page(s) 32.
- Wang, L., Bornert, M., Héripré, E., Chanchole, S., & Tanguy, A. (2014). Full-field measurements on low-strained geomaterials using environmental scanning electron microscopy and digital image correlation: Improved imaging conditions. *Strain*, 50, 370–380. Cited on page(s) 67.
- Wang, R., & Weiner, S. (1997). Strain–structure relations in human teeth using moiré fringes. *Journal of biomechanics*, 31, 135–141. Cited on page(s) 49.

- Wang, W., Roubier, N., Puel, G., Allain, J.-M., Infante, I. C., Attal, J.-P., & Vennat, E. (2015). A new method combining finite element analysis and digital image correlation to assess macroscopic mechanical properties of dentin. *Materials*, 8, 535–550. Cited on page(s) 6, 60.
- Wang, Y., Sutton, M., Bruck, H., & Schreier, H. (2009). Quantitative error assessment in pattern matching: effects of intensity pattern noise, interpolation, strain and image contrast on motion measurements. *Strain*, 45, 160–178. Cited on page(s) 27.
- Waters, N. (1979). Some mechanical and physical properties of teeth. In *Symposia of the Society for Experimental Biology* (pp. 99–135). volume 34. Cited on page(s) 59, 60.
- Wattrisse, B., Chrysochoos, A., Muracciole, J.-M., & Némoz-Gaillard, M. (2001). Analysis of strain localization during tensile tests by digital image correlation. *Experimental Mechanics*, 41, 29–39. Cited on page(s) 27.
- Weiner, S., Veis, A., Beniash, E., Arad, T., Dillon, J. W., Sabsay, B., & Siddiqui, F. (1999). Peritubular dentin formation: crystal organization and the macromolecular constituents in human teeth. *Journal of structural biology*, 126, 27–41. Cited on page(s) 10.
- Williams, C., Wu, Y., & Bowers, D. F. (2015). Imagej analysis of dentin tubule distribution in human teeth. *Tissue and Cell*, 47, 343–348. Cited on page(s) 8, 114, 117.
- Wu, Z., Baker, T., Ovaert, T., & Niebur, G. (2009). Viscoelastic properties of human cortical bone tissue depend on gender. In *Annual conference of the Orthopaedic Research Society. Las Vegas, USA*. Cited on page(s) 103.
- Yang, D., Bornert, M., Chanchole, S., Gharbi, H., Valli, P., & Gatmiri, B. (2012). Dependence of elastic properties of argillaceous rocks on moisture content investigated with optical full-field strain measurement techniques. *International Journal of Rock Mechanics and Mining Sciences*, 53, 45–55. Cited on page(s) 61.
- Young, B., Woodford, P., & O'Dowd, G. (2013). *Wheater's functional histology: a text and colour atlas*. Elsevier Health Sciences. Cited on page(s) 5, 6.
- Zaytsev, D., & Panfilov, P. (2014). Deformation behavior of human enamel and dentin–enamel junction under compression. *Materials Science and Engineering: C*, 34, 15–21. Cited on page(s) 19, 21.

Bibliography

- Zhang, D., & Arola, D. D. (2004). Applications of digital image correlation to biological tissues. *Journal of Biomedical Optics*, 9, 691–699. Cited on page(s) 27, 60.
- Zhang, D., Zhang, X., & Cheng, G. (1999). Compression strain measurement by digital speckle correlation. *Experimental mechanics*, 39, 62–65. Cited on page(s) 27.
- Zhao, W., & Jin, G. (1996). An experimental study on measurement of poisson's ratio with digital correlation method. *Journal of applied polymer science*, 60, 1083–1088. Cited on page(s) 27.
- Ziskind, D., Fleischer, S., Zhang, K., Cohen, S. R., & Wagner, H. D. (2010). A novel experimental method for the local mechanical testing of human coronal dentin. *dental materials*, 26, 179–184. Cited on page(s) 24, 25, 26.
- Ziskind, D., Hasday, M., Cohen, S. R., & Wagner, H. D. (2011). Young's modulus of peritubular and intertubular human dentin by nano-indentation tests. *Journal of structural biology*, 174, 23–30. Cited on page(s) 23, 26, 167.
- Zuiderveld, K. (1994). Contrast limited adaptive histogram equalization. In *Graphics gems IV* (pp. 474–485). Academic Press Professional, Inc. Cited on page(s) 44.

Appendices

ESEM OBSERVATIONS

The Stitching Images

The surfaces were observed by ESEM (Quanta 600, FEI Co., America) under back scattering electron (BSE) mode image by image. Then, a stitching process was applied by an open source software *Fiji*. The chamber pressure is set at 266Pa . The temperature is set at 5°C resulting a relative humidity of 30%. The electron beam voltage is set at 10kV. Working distance is 10mm. Due to the limitation of beam aperture of the ESEM, the maximum field of view of ESEM here is $340\mu\text{m}$. Before the capture action, all the parameters (contrast, brightness and etc.) were well adjusted in order to keep good image quality. Each image was captured in 10min with a high resolution of 2048×1768 pixels resulting a dimension of $0.17\mu\text{m}$ for each pixel. As shown in [Fig. A.1](#) and [Fig. A.2](#), the surfaces of the sample AC1 were observed.

Repetitive Tests for the Distribution of Area Fraction

Four repetitive tests (sample AC2 to AC4) were carried out in order to have the statical results for the area fraction distributions of the dentin components. The samples were all taken from a third molar of human tooth obtained from the faculty of dentistry of Paris Descartes University. [Fig. A.3](#) to [Fig. A.6](#) show the distribution of the fraction area for each component of dentin from pulp cavity to DEJ for 4 repetitive tests.

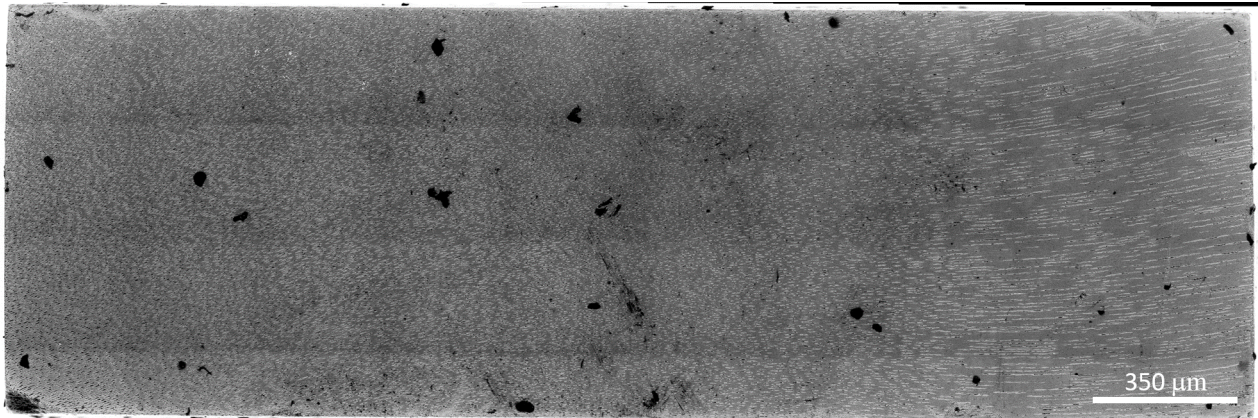


Figure A.1 – The surface (face 4) of the dentin parallelepiped (sample AC1) extended from root dentin to crown dentin stitched by the BSE images. A image stitching process was applied using the software *Fiji*.

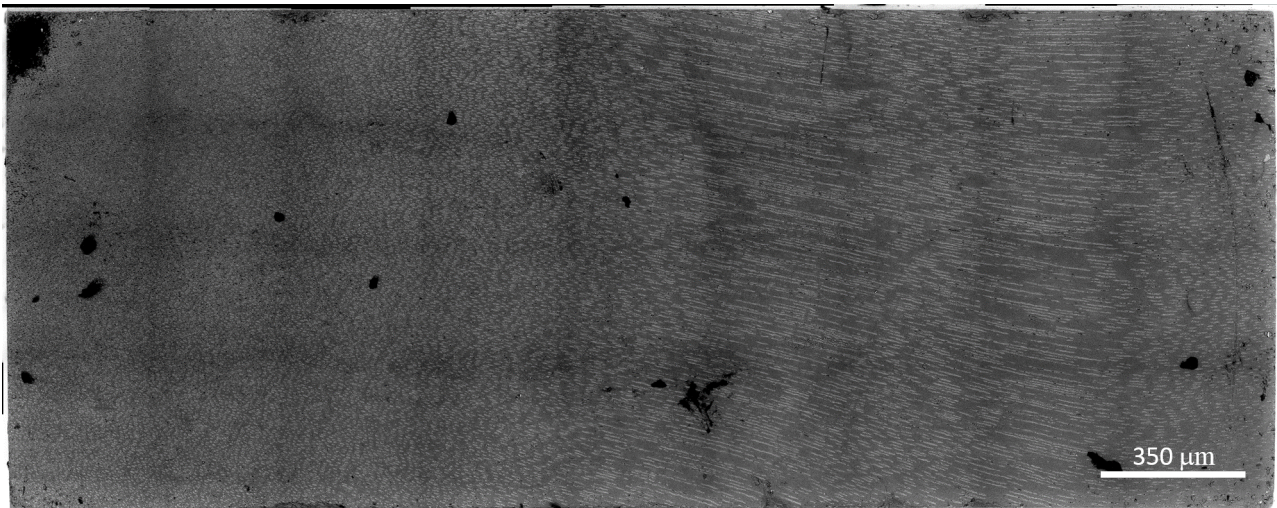


Figure A.2 – The surface (face 5) of the dentin parallelepiped (sample AC1) extended from root dentin to crown dentin stitched by the BSE images. A image stitching process was applied using the software *Fiji*.

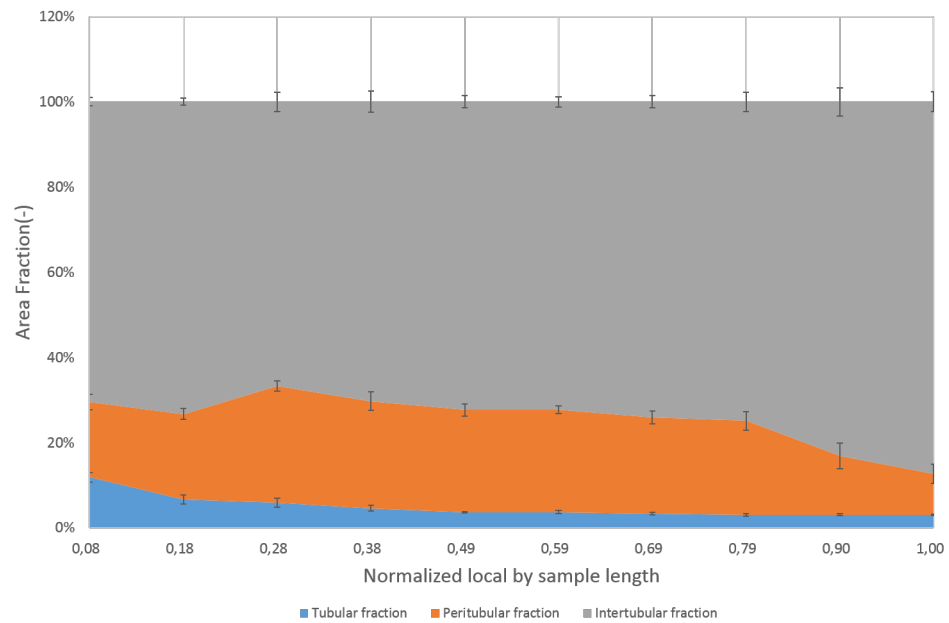


Figure A.3 – Distribution of the area fraction on the surface of the dentin parallelepiped (sample.AC2) extended from root dentin to crown dentin.

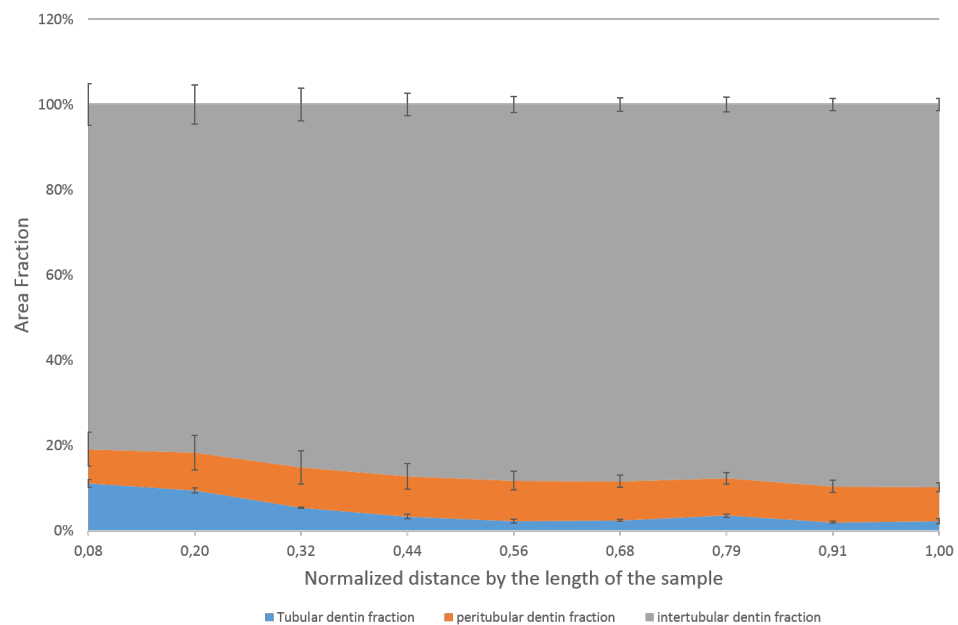


Figure A.4 – Distribution of the area fraction on the surface of the dentin parallelepiped (sample.AC3) extended from root dentin to crown dentin.

Appendix A. ESEM observations

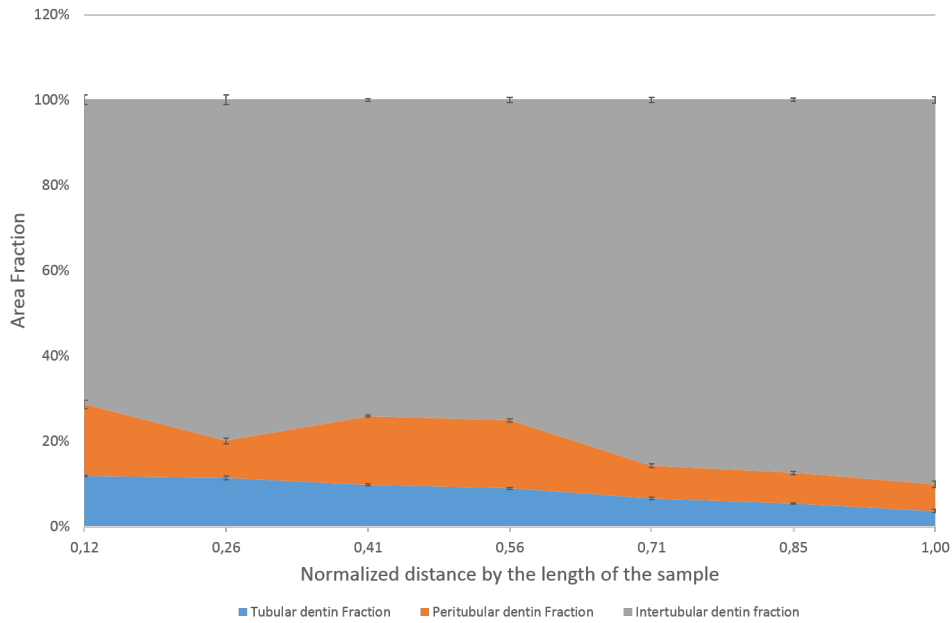


Figure A.5 – Distribution of the area fraction on the surface of the dentin parallelepiped (sample.AC4) extended from root dentin to crown dentin.

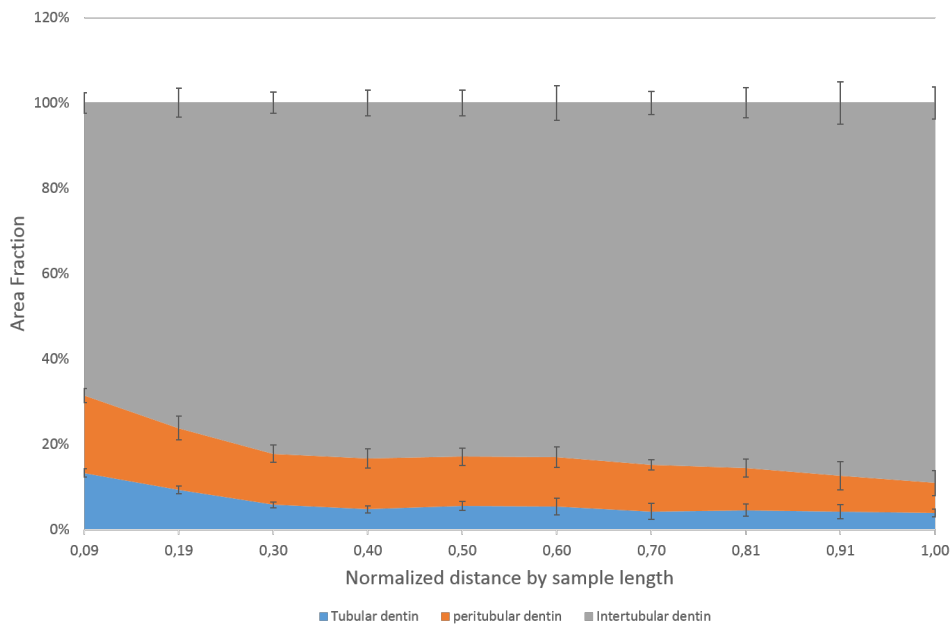


Figure A.6 – Distribution of the area fraction on the surface of the dentin parallelepiped (sample.AC5) extended from root dentin to crown dentin.

DENTIN COMPRESSION TESTS

Typical stress and strain curves of all the compression tests (Samples: AC1 to AC10) were shown from Fig. B.1 to Fig. B.8. The test results were summarized in Table B.1 and Table B.2. The elastic modulus as a function of the relative humidity was also plotted as shown in Fig. B.9.

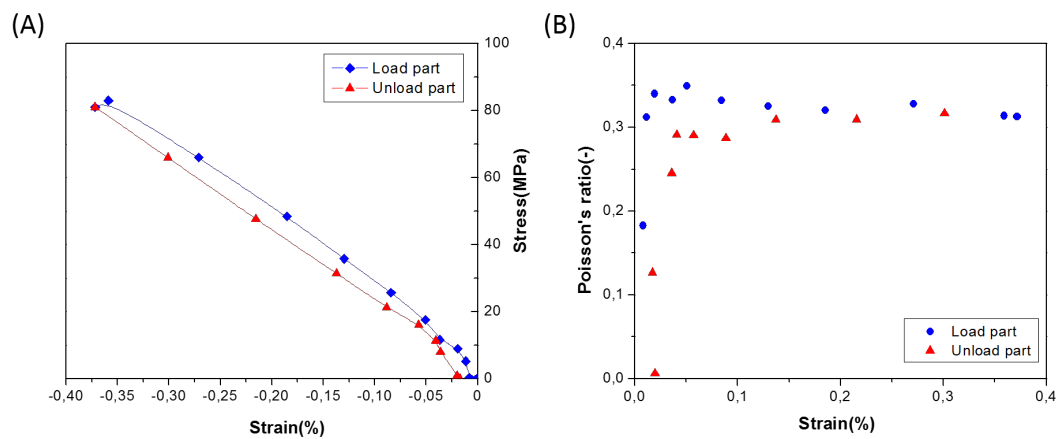


Figure B.1 – Stress-strain curve (A) and the Poisson ratio distribution (B) in the compression test of the dentin sample AC1

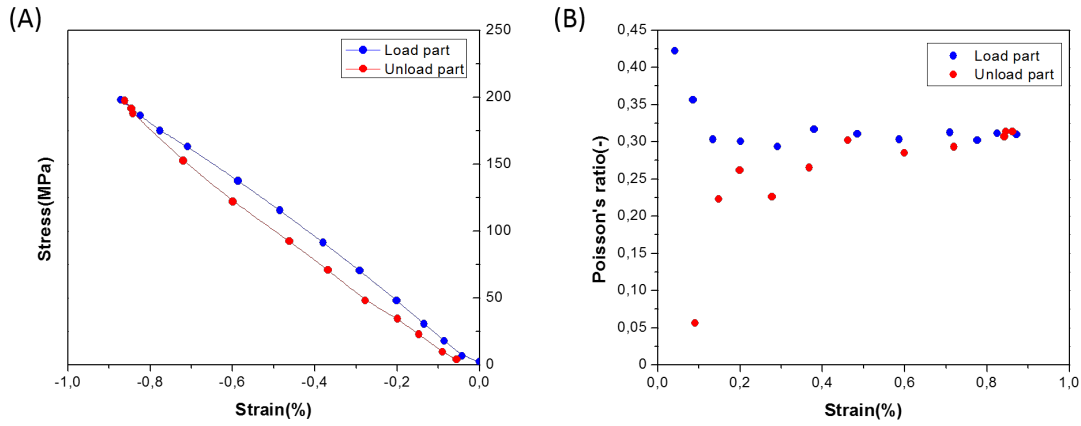


Figure B.2 – Stress-strain curve (A) and the Poisson ratio distribution (B) in the compression test of the dentin sample AC2

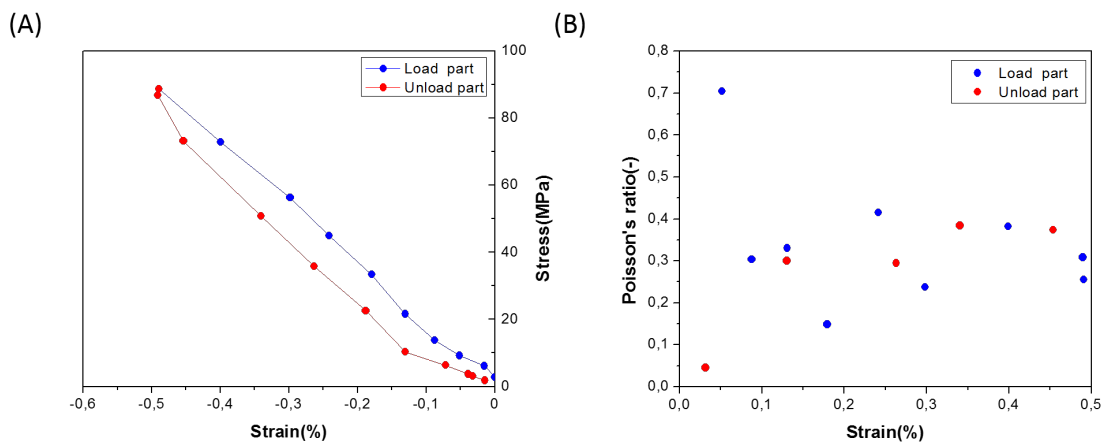


Figure B.3 – Stress-strain curve (A) and the Poisson ratio distribution (B) in the compression test of the dentin sample AC3

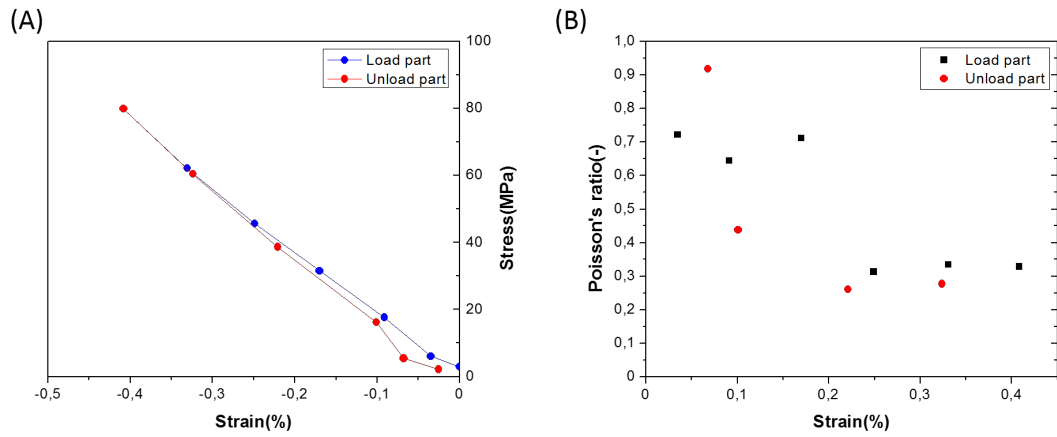


Figure B.4 – Stress-strain curve (A) and the Poisson ratio distribution (B) in the compression test of the dentin sample AC4

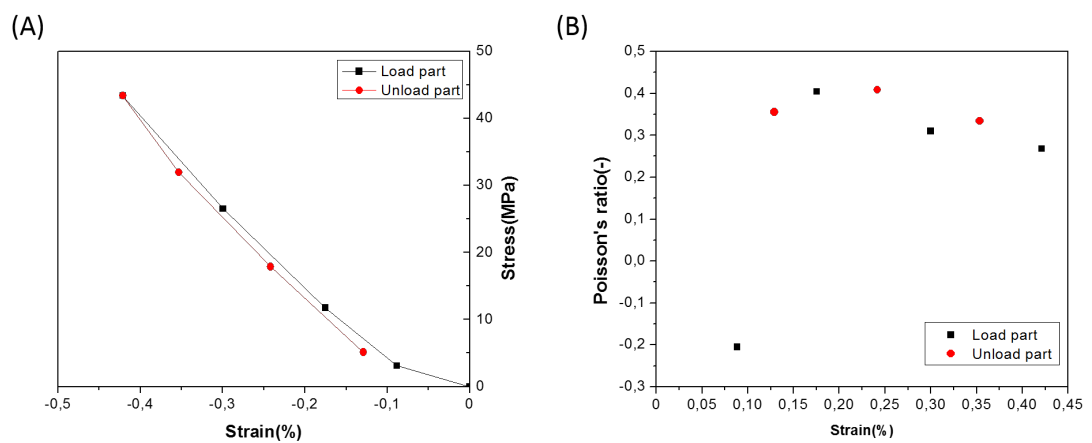


Figure B.5 – Stress-strain curve (A) and the Poisson ratio distribution (B) in the compression test of the dentin sample AC6

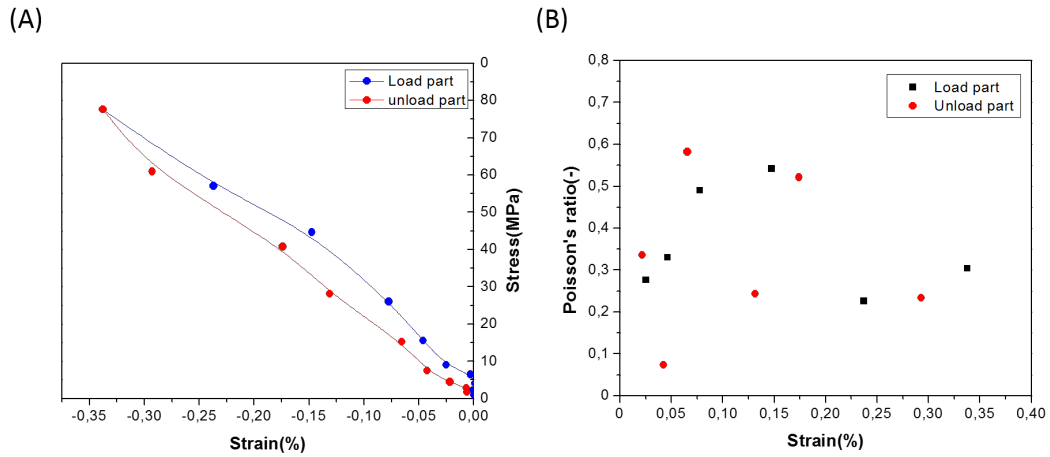


Figure B.6 – Stress-strain curve (A) and the Poisson ratio distribution (B) in the compression test of the dentin sample AC7

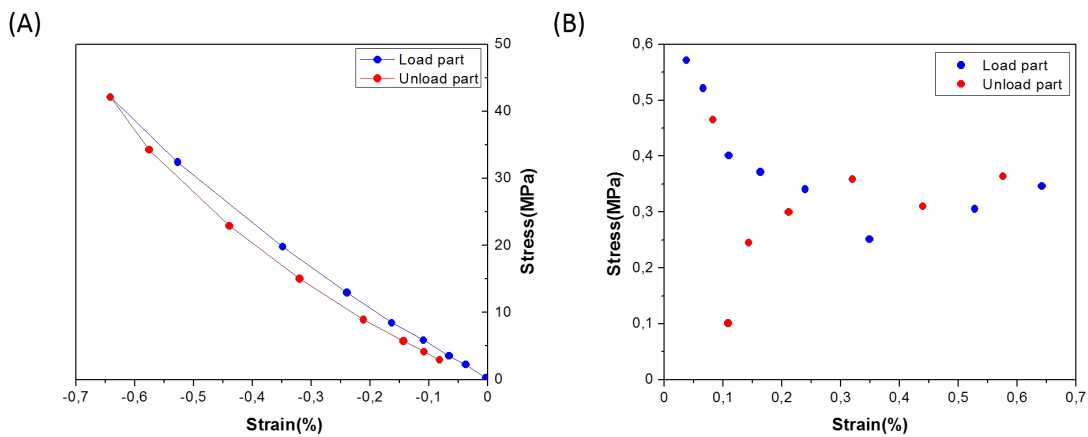


Figure B.7 – Stress-strain curve (A) and the Poisson ratio distribution (B) in the compression test of the dentin sample AC9

Table B.1 – Summary of the compression results for all the humidities: Part 1

Sample	Relative Humidity (%)	Temperature (°C)	Modulus deduced from load (GPa)	Modulus deduced from unload (GPa)	Poisson's ratio (-)
AC1	55.02 (0.10)	29.60 (0.18)	20.86	21.11	0.31 (0.02)
	72.17 (0.21)	29.57 (0.21)	20.81	22.23	0.31 (0.02)
	86.63 (0.19)	30.02 (0.18)	20.69	21.90	0.31 (0.02)
	70.59 (0.16)	29.91 (0.19)	20.85	23.14	0.31 (0.03)
	54.52 (0.16)	29.95 (0.23)	20.67	22.19	0.31 (0.02)
AC2	56.00 (0.06)	24.30 (0.20)	21.11	21.60	0.29 (0.01)
	74.44 (0.15)	25.78 (0.20)	21.95	23.31	0.31 (0.02)
	92.27 (0.29)	26.65 (0.17)	22.33	24.59	0.30 (0.02)
	73.71 (0.22)	26.72 (0.19)	23.89	25.39	0.28 (0.06)
	56.05 (0.06)	26.72 (0.17)	21.34	21.50	0.29 (0.03)
AC3	55.62 (0.11)	25.72 (0.28)	18.66	19.93	0.31 (0.05)
	75.70 (0.14)	25.98 (0.20)	16.95	17.27	0.34 (0.02)
	88.74 (0.21)	26.23 (0.24)	17.85	17.83	0.33 (0.06)
	74.34 (0.16)	26.55 (0.15)	17.76	18.48	0.30 (0.09)
	55.76 (0.06)	26.72 (0.22)	17.15	19.61	0.32 (0.06)
AC4	55.72 (0.07)	25.94 (0.18)	18.88	20.61	0.36 (0.10)
	75.85 (0.12)	26.24 (0.20)	18.69	19.35	0.35 (0.14)
	89.09 (0.11)	26.67 (0.14)	18.24	20.33	0.38 (0.06)
	75.82 (0.15)	26.79 (0.18)	18.30	19.31	0.34 (0.16)
	56.33 (0.07)	26.85 (0.20)	18.46	19.24	0.30 (0.12)

Table B.2 – Summary of the compression results for all the humidities: Part 2

Sample	Relative Humidity (%)	Temperature (°C)	Modulus deduced from load (GPa)	Modulus deduced from unload (GPa)	Poisson's ratio (-)
AC6	54.80 (0.05)	26.83 (0.28)	11.07	12.55	0.21 (0.06)
	74.48 (0.17)	28.29 (0.24)	12.13	12.92	0.33 (0.06)
	89.56 (0.23)	29.47 (0.27)	12.00	12.89	0.24 (0.05)
AC7	73.68 (0.20)	30.13 (0.18)	11.52	13.14	0.34 (0.13)
	55.42 (0.10)	30.36 (0.16)	11.97	12.82	0.38 (0.05)
	55.70 (0.07)	26.85 (0.11)	22.66	22.99	0.21 (0.05)
AC8	75.70 (0.17)	27.12 (0.19)	21.71	22.49	0.25 (0.07)
	89.42 (0.16)	27.16 (0.20)	22.51	22.15	0.35 (0.12)
	74.97 (0.12)	27.13 (0.15)	21.25	21.50	0.39 (0.07)
	55.45 (0.08)	27.34 (0.19)	20.74	22.08	0.26 (0.11)
	54.53 (0.09)	30.20 (0.24)	17.46	19.66	0.31 (0.02)
AC9	75.34 (0.33)	28.52 (0.21)	19.84	19.92	0.38 (0.09)
	87.88 (0.17)	30.10 (0.15)	18.46	19.59	0.35 (0.04)
	74.51 (0.17)	30.13 (0.25)	18.91	20.55	0.32 (0.07)
	56.68 (0.10)	27.02 (0.18)	20.37	22.07	0.29 (0.13)
	52.67 (0.08)	30.66 (0.20)	6.71	6.63	0.33 (0.09)
AC10	66.19 (0.12)	30.82 (0.24)	6.58	6.80	0.34 (0.08)
	79.67 (0.30)	30.42 (0.20)	6.60	6.67	0.31 (0.07)
	77.48 (0.22)	31.07 (0.22)	6.54	6.77	0.33 (0.07)
AC10	55.48 (0.09)	25.97 (0.20)	12.56	14.91	0.28 (0.03)
	74.87 (0.18)	26.07 (0.22)	12.62	14.98	0.25 (0.05)
	86.36 (0.21)	26.77 (0.15)	13.26	14.09	0.23 (0.04)
	74.58 (0.18)	27.04 (0.23)	14.35	16.28	0.22 (0.05)
	55.71 (0.09)	27.33 (0.17)	12.56	14.91	0.26 (0.03)

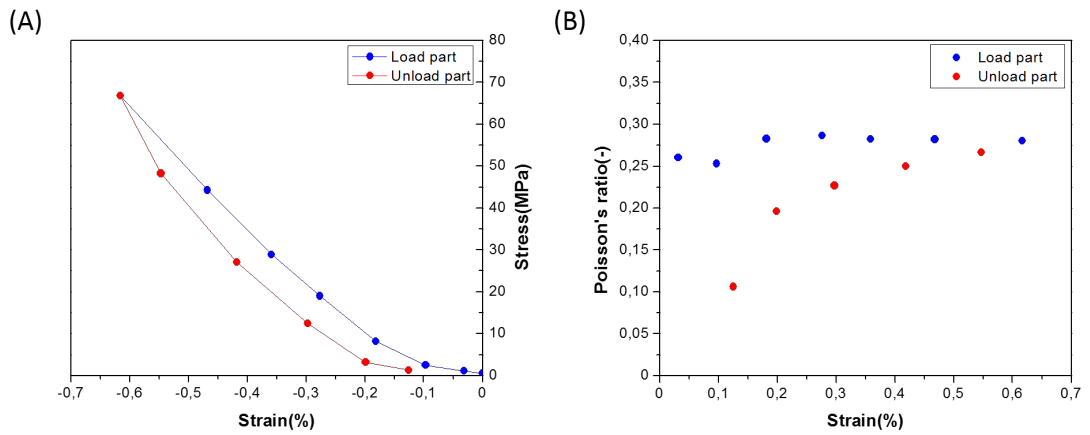


Figure B.8 – Stress-strain curve (A) and the Poisson ratio distribution (B) in the compression test of the dentin sample AC10

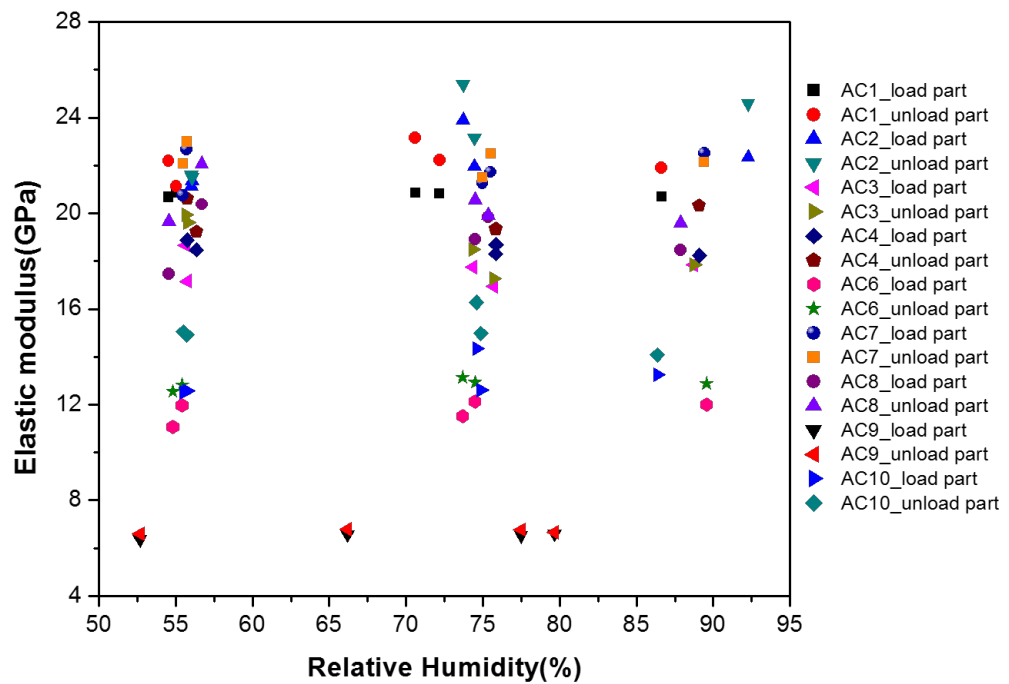


Figure B.9 – The influence of the humidity to the elastic modulus for sample AC1 to AC10. The modulus was deduced both from the load and unload part of the stress-strain curve.

HUMIDITY DILATATION RESULTS

The results of the free dilatation for human dentin (sample AC2 to AC10) were presented from Fig. C.1 to Fig. C.9.

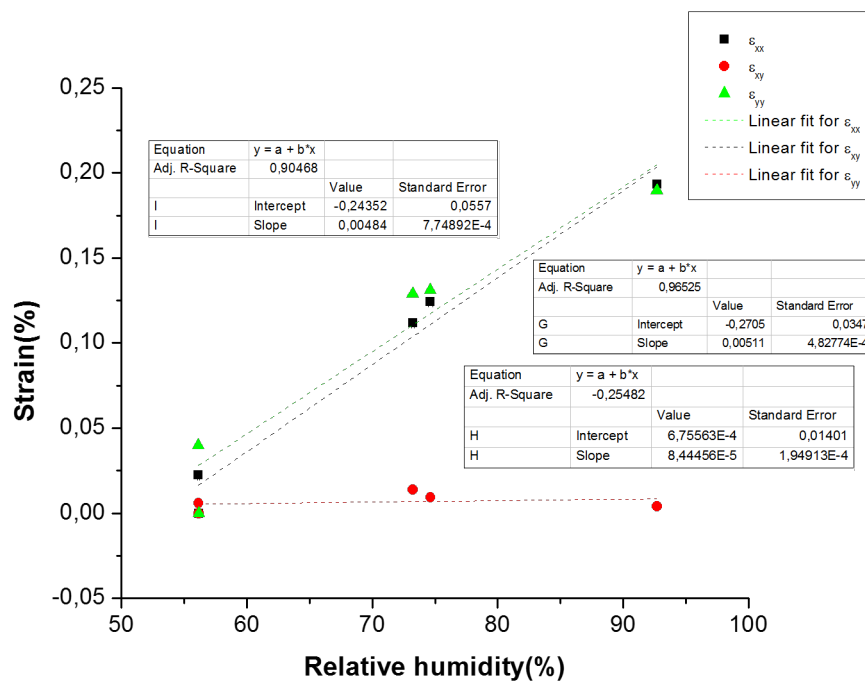


Figure C.1 – Free dilatation coefficient of human dentin as a function of relative humidity for sample AC2

Appendix C. Humidity Dilatation Results

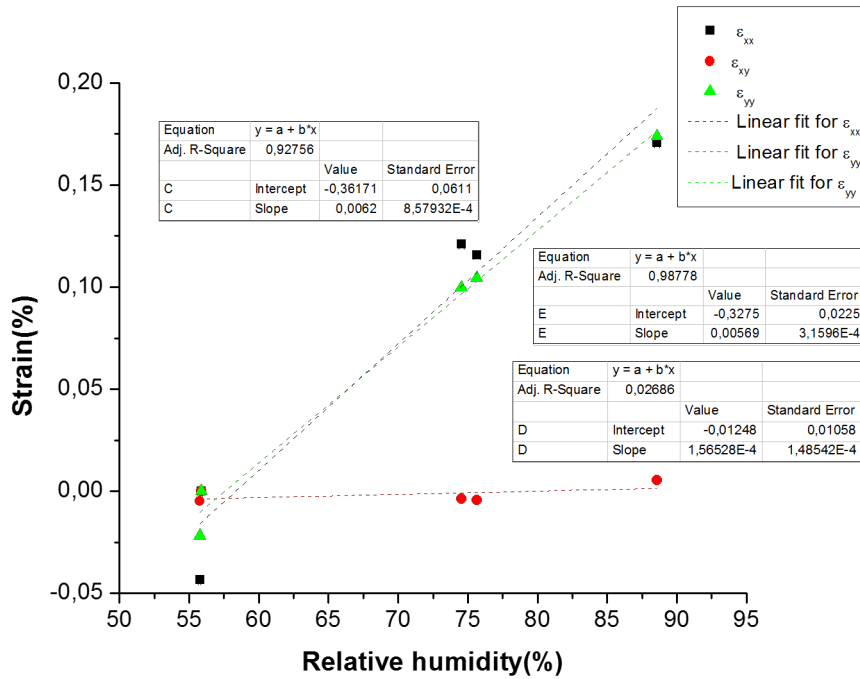


Figure C.2 – Free dilatation coefficient of human dentin as a function of relative humidity for sample AC3

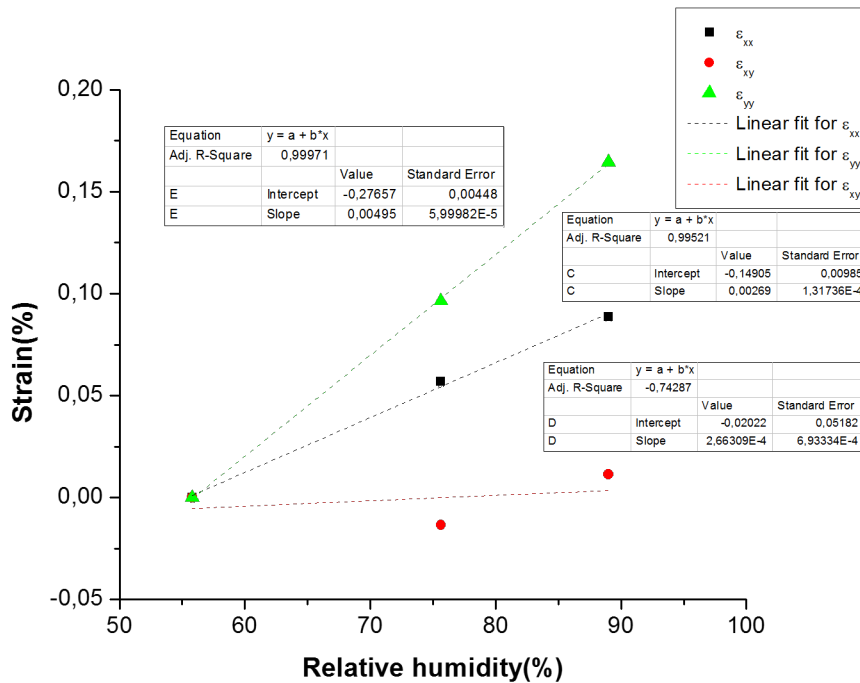


Figure C.3 – Free dilatation coefficient of human dentin as a function of relative humidity for sample AC4

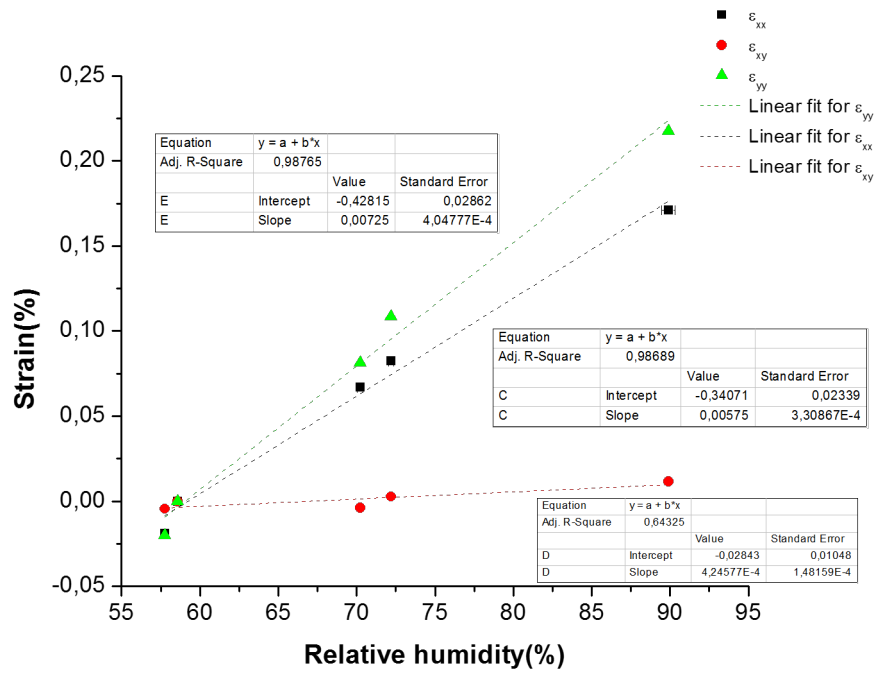


Figure C.4 – Free dilatation coefficient of human dentin as a function of relative humidity for sample AC5

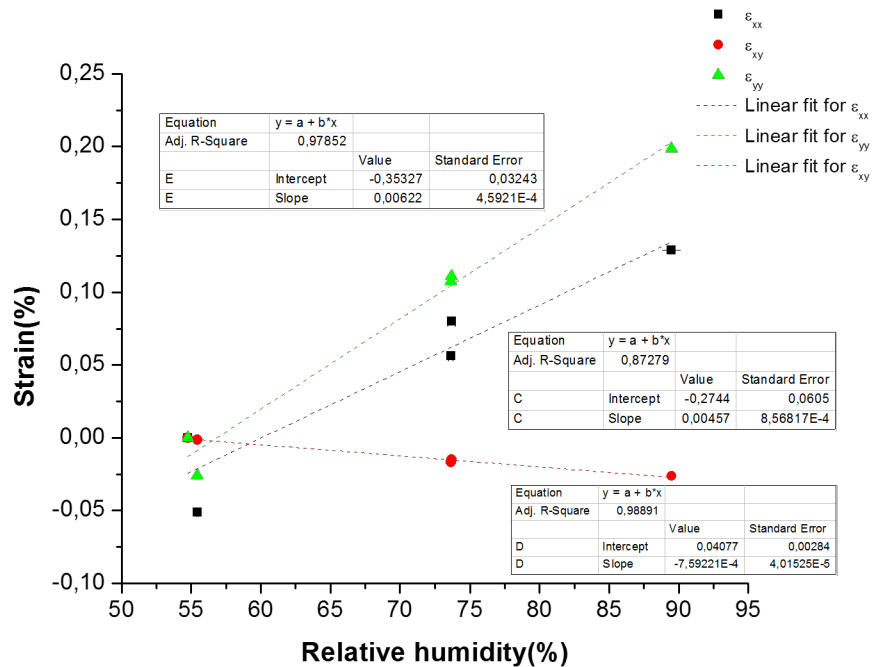


Figure C.5 – Free dilatation coefficient of human dentin as a function of relative humidity for sample AC6

Appendix C. Humidity Dilatation Results

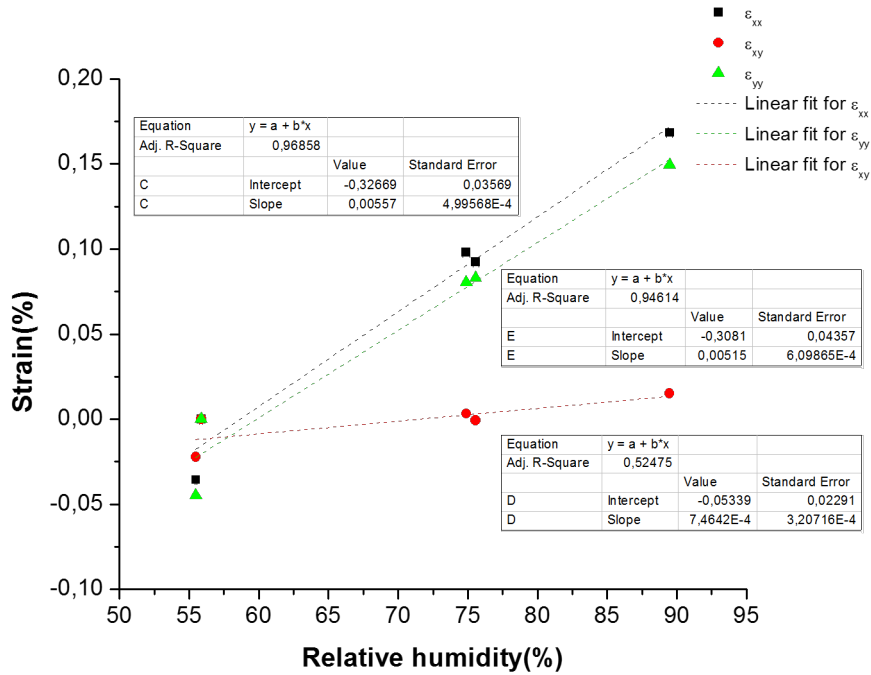


Figure C.6 – Free dilatation coefficient of human dentin as a function of relative humidity for sample AC7

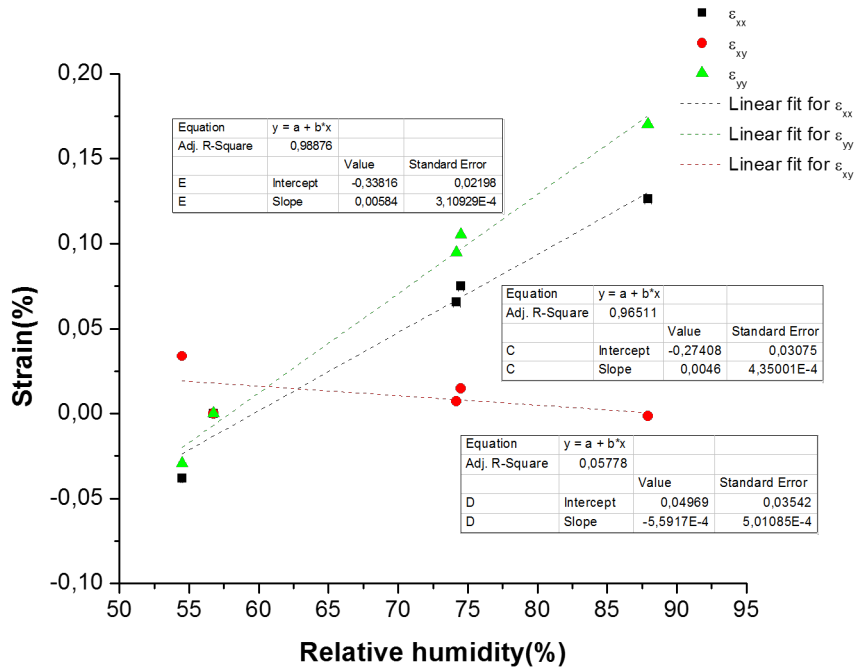


Figure C.7 – Free dilatation coefficient of human dentin as a function of relative humidity for sample AC8

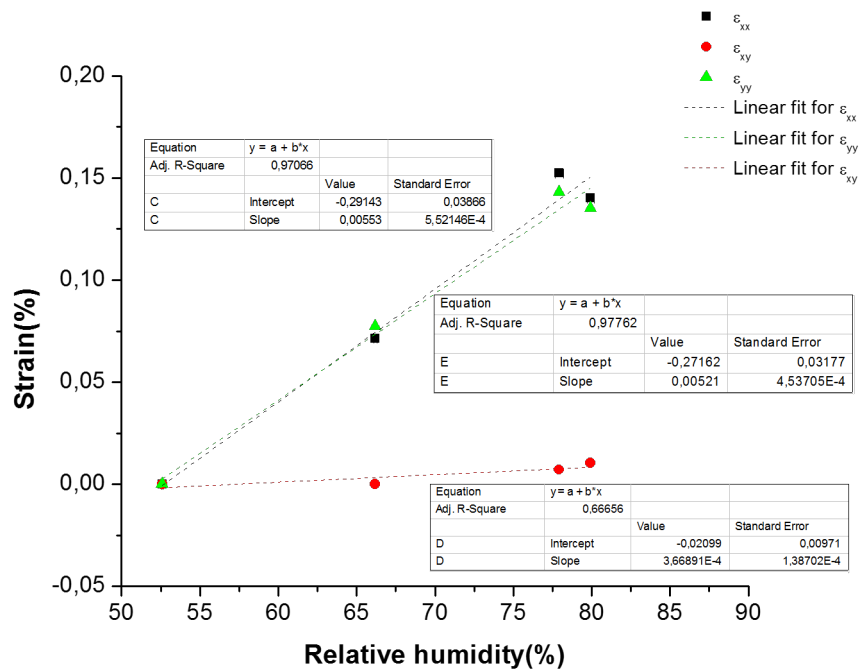


Figure C.8 – Free dilatation coefficient of human dentin as a function of relative humidity for sample AC9

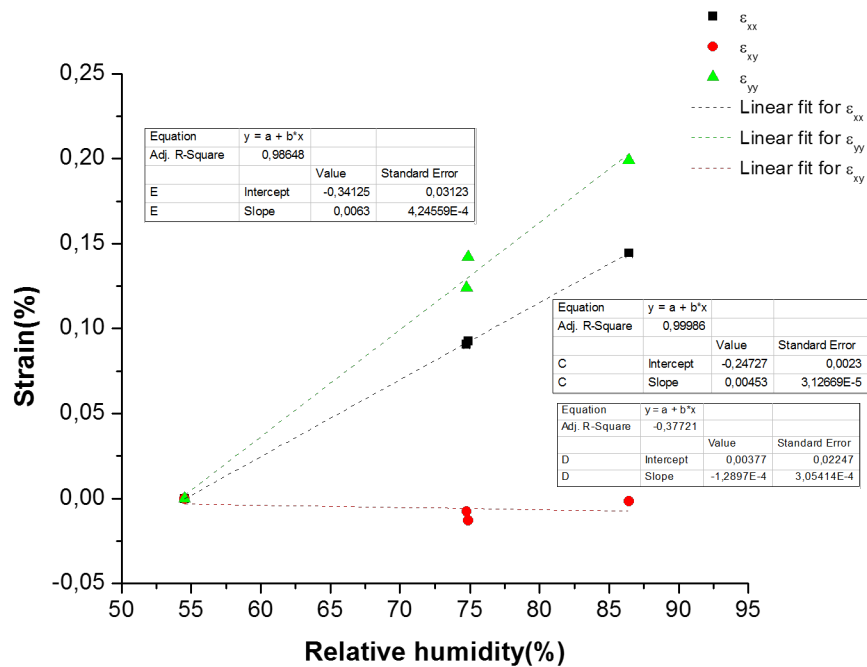


Figure C.9 – Free dilatation coefficient of human dentin as a function of relative humidity for sample AC10

**A NEW METHOD COMBINING FINITE
ELEMENT ANALYSIS AND DIGITAL
IMAGE CORRELATION TO ASSESS
MACROSCOPIC MECHANICAL
PROPERTIES OF DENTIN**

A new method to assess stress and strain in the case of a three-point bending test is proposed. A two-step procedure is thus chosen: first, for typical, published, bending tests, a re-evaluation of the stresses by the finite element method (instead of using the Bernoulli-Euler beam theory as it is classically done) was proposed. The differences in terms of maximum stress will be illustrated through the analysis of two articles [Rees et al., 1994; Eltit et al., 2013]. Secondly, a three-point bending test combined with Finite Element Analysis (FEA) and Digital Image Correlation (DIC) is proposed, taking advantage of the complementarity of these two methods.

Recalculation of the Stresses Found in the Literature

Two articles were chosen because they provide sample geometries and some results from three-point bending tests and four-point bending tests respectively [Rees et al., 1994; Eltit et al., 2013]. The values from the published articles were recalculated using the classical beam theory (Chap. D). Then, using the experimental conditions mentioned in the two selected articles, the stresses were recalculated by the finite element method (Chap. D).

Rees et al. [1994] performed static three-point bending tests to measure dentin elastic modulus (Fig. D.1)

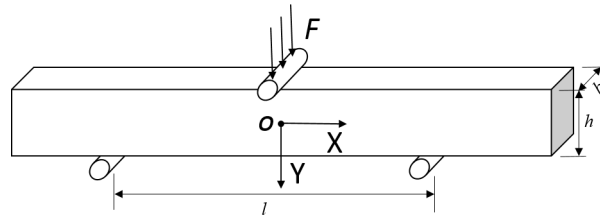


Figure D.1 – Scheme of three-point bending test.

To assess the stresses in the beam, the Bernoulli–Euler beam model can be used (at $x = 0$, which is the cross-section where the stresses are the highest) with:

$$\sigma_{xx} = \frac{3Fl}{bh^3}y$$

where σ_{xx} is the normal stress in direction x, F is the load, l is the supporting span, b is the beam width, h is the beam thickness, and y is the coordinate in direction y. In Rees et al. experiment [Rees et al., 1994], beams were 2mm wide, 2mm in depth and presented an average length of 13mm. The distance for the supporting span was 11mm. Thus, the ratio (l/h) was 5.5. Then, the modulus was calculated from Bernoulli-Euler beam equation:

$$E = \frac{Fl^3}{4bdh^3}$$

where F is the load, and d is the deflection at the given load.

Eltit et al. [2013] performed four-point bending tests on dentinal samples. They studied the max-

imum flexural stress of coronal and root dentin. The tested beam dimension was $0.4 \times 1.2 \times 7$ mm (thickness \times width \times length). The supporting span of the bending device was 5 mm, and the loading span was 1.5 mm, as is shown in Fig. D.2.

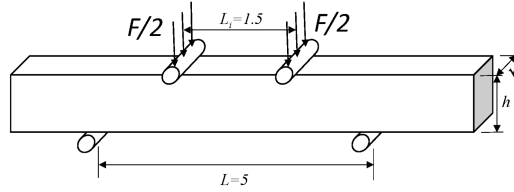


Figure D.2 – Scheme of four-point bending test.

According to the Bernoulli-Euler beam equation, the maximum flexural stress can be expressed as:

$$\sigma_f = \frac{3F(L - L_i)}{2bh^2}$$

where σ_f is the maximum flexural stress, F is the load, L is the supporting span, L_i , is the loading span, b is the beam width, and h is the thickness of the beam.

Recalculations by finite element analysis (FEA)

The simulations were performed with the commercial software Comsol Multiphysics. In the FEA, we use the static equilibrium equations under small deformation assumption with an isotropic relation:

$$\mathbf{f}_b + \nabla \cdot \boldsymbol{\sigma} = 0$$

$$\boldsymbol{\varepsilon} = \frac{1}{2}[\nabla \mathbf{u} + \nabla \mathbf{u}^T]$$

$$\boldsymbol{\varepsilon} = \frac{1 + \nu}{E} \boldsymbol{\sigma} - \frac{\nu}{E} \text{tr}(\boldsymbol{\sigma}) \mathbf{I}$$

where \mathbf{f}_b is the body force, $\boldsymbol{\sigma}$ is the stress tensor, $\boldsymbol{\varepsilon}$ is the strain tensor, \mathbf{u} is the displacement, ν is the Poisson ratio, E is elastic modulus, and \mathbf{I} is the identity matrix.

For recalculating the stress in three-point bending test, about 204000 tetrahedral elements were used in the mesh. The boundary conditions are the following:

- Fixed constraints ($\mathbf{u} = 0$) were applied to the two support edges

Appendix D. A New Method Combining Finite Element Analysis and Digital Image Correlation to Assess Macroscopic Mechanical Properties of Dentin

- Boundary load of total force (50N) was applied to the middle area (0.6mm×2mm) between the two supporting edges

For recalculating the stress in four-point bending test, about 240000 tetrahedral elements were used in the mesh. The boundary conditions are the following:

- Fixed constraints ($\mathbf{u} = 0$) were applied to the two support edges
- Edge load of total force (5 or 12N) was applied to the loading part (consisting of two loading edges here)

The edge load was chosen in order to reproduce data from [Eltit et al. \[2013\]](#) experiment. Within the load-deflection curves from the four-point bending tests of [Eltit et al. \[2013\]](#), it can be inferred that the maximum bending force used for crown dentin beams was about 5N, and for root dentin beams, the bending force was around 10-15N (here, 12N was chosen as an example).

Proposed experimental protocol

Sample preparation

A dentin specimen was obtained from sound human third molar. The specimen was polished progressively by 80, 500, 800, 1200, 1400, 2000, 2400, 4000 grit. SiC polishing papers under water irrigation, and finally turned to cloth polishing with 1 μ m diamond suspension liquid for both sides. Then, the dentin slice was cut into one beam with a line cutting saw (Isomet low speed saw, BUEHLER Co., USA). The sample preparation scheme was shown in [Fig. D.3](#). After cutting, the new surfaces were then polished with the same previous polishing steps. Finally, the beam dimensions were controlled as 8mm×1.38mm×1.15mm. Before each step, the sample was washed in an ultrasonic cleaner for 3-5 minutes. Then, the specimen was stored in the distilled water below 4 °C until the test.

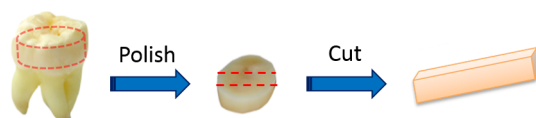


Figure D.3 – Scheme of sample preparation

Three-point bending set up

Three-point bending test was performed using a bending test device equipped with a 1kN load cell (MICROTEST, DEBAN, UK) with a supporting span of 5mm. Motor speed was selected as 0.2mm/min. All the setup was mounted under an optical microscope (InfiniteFocus, Alicona Co., Germany) in order to get the strain distribution of the beam side surface located below the force-indenter as shown in Fig. D.4. The direction of the load is applied perpendicular to the tubular orientation.

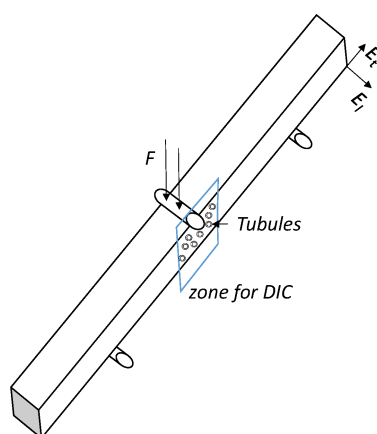


Figure D.4 – Three-point bending test under the optical microscope.

DIC

The software *correli_q4* [Hild & Roux, 2008] was used to analyze the strain distribution comparing the reference and deformed images. The deformed image was taken under the load force of 60N. The element size for DIC was selected as 64 pix.

Determination of the elastic modulus and σ_{max}

The mechanical set up is placed under an optical microscope in order to get images of a selected area of the sample (Fig. D.4) at different loads. Strain estimates are obtained by DIC and the stresses are estimated by FEA. The edge load can be known from the three-point bending test device. With the maximum total force, one can obtain the maximum tensile stress by FEA. During the bending test process, the strain is evaluated by DIC. Using stress and strain estimates in x direction as it is shown

Appendix D. A New Method Combining Finite Element Analysis and Digital Image Correlation to Assess Macroscopic Mechanical Properties of Dentin

in Fig. 1, when the terms σ_{yy} and σ_{zz} were much lower than σ_{xx} , elastic modulus in x direction (E_t) can be derived by Hooke's law:

$$E_t = \frac{\sigma_{xx}}{\varepsilon_{xx}}$$

In our case, the maximum total force which was found in the experiment ($F_{max} = 65N$) was used to determine the maximum bending stress. Tensile test and bending test are known to give slightly different results even when the material fails in tension in both tests that is why the bending tests results in term of strength are called flexural or bending strength and not tensile strength. In this article, we will estimate the maximum tensile stress in the experiment and call it as it is usually done "flexural strength". A total force of 60N (F_x) was used to determine the stress in order to obtain the elastic modulus, as it is shown in Fig. D.5.

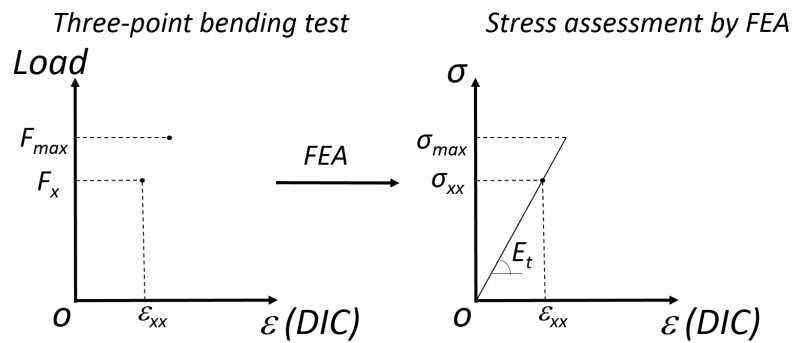


Figure D.5 – Method of the determination of elastic modulus and of the maximum stress values σ_{max}

Results and Discussion

Recalculation of the stresses in bending test configurations found in the two selected articles

With the beam dimensions in three-point bending test of Rees et al. [1994], using the Euler-Bernoulli equation, the maximum tensile stress (often called maximum bending or flexural stress) with assuming boundary force ($F = 50N$) is calculated as 103.1 MPa, whereas, using FEA, the maximum tensile stress is 58.2 MPa. Fig. D.6 shows the distribution of σ_{xx} in three-point bending test. As

expected, there is a neutral plan in the middle of the beam, and the values are antisymmetric relatively to the stress direction (compression and tension). The maximum tensile stress is located at the outside surface of the beam.

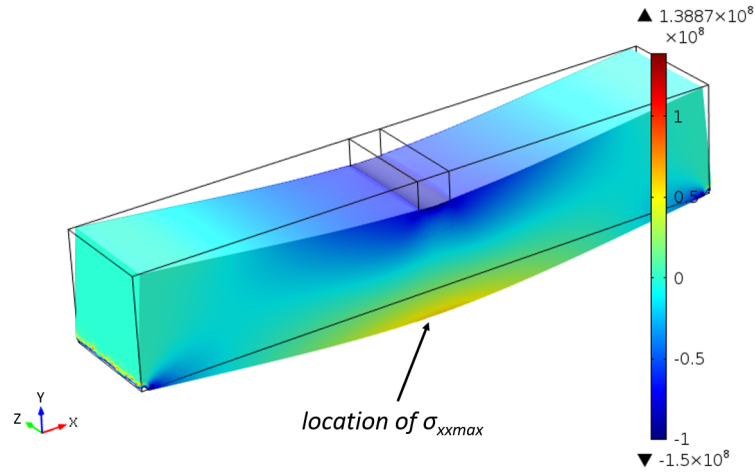


Figure D.6 – σ_{xx} distribution in the beam (unit for color scale bar: Pa)

For four-point bending test, according to the Bernoulli-Euler beam equation, the maximum tensile stress for crown and root dentin samples (loads of 5N and 12N which are the maximum loads found by Eltit et al. [Eltit et al. \[2013\]](#) were 136.7MPa and 328.1MPa, which matched the values expressed in their work. However, by using FEA, the maximum tensile stress for coronal and root dentin test is found as 59.1 MPa and 141.8 MPa, respectively. σ_{xx} distribution map was shown in [Fig. D.7](#) with an edge load of 12N. The maximum bending stress can be found in the outside edge of the beam withstanding tensile stress.

Experimental results from the proposed method

Strain distribution map along direction y obtained by DIC is shown in [Fig. D.8](#). ε_{xx} shows a linear relationship with respect to the local coordinate in direction y. Five areas (columns 1 to 5) were selected to evaluate ε_{xx} distribution which is approximately antisymmetric relatively to the middle neutral plan as expected. In the same positions, stress distributions were assessed by FEA. Thus, mean elastic modulus was found as 11.9 GPa. With the maximum boundary load of 65N found in the experiment, the stress distribution map is obtained by FEA with beam dimensions corresponding to our dentin sample. Tensile stresses are logically located under the neutral plan. σ_{xx} was found as 143.9 MPa on

Appendix D. A New Method Combining Finite Element Analysis and Digital Image Correlation to Assess Macroscopic Mechanical Properties of Dentin

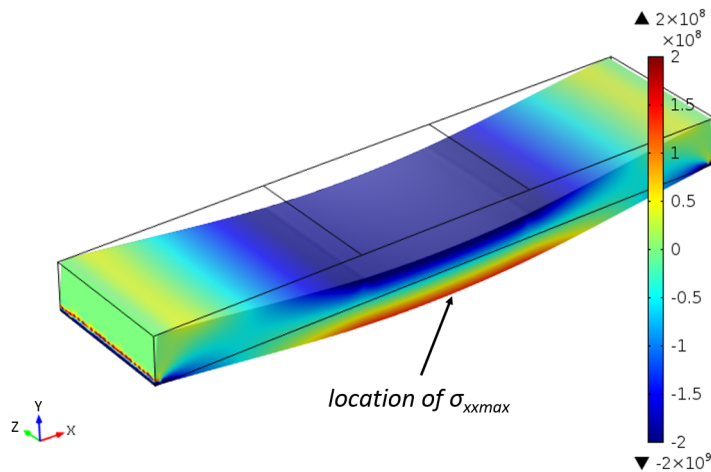


Figure D.7 – σ_{xx} distribution map of four-point bending test (unit of color scale bar: Pa)

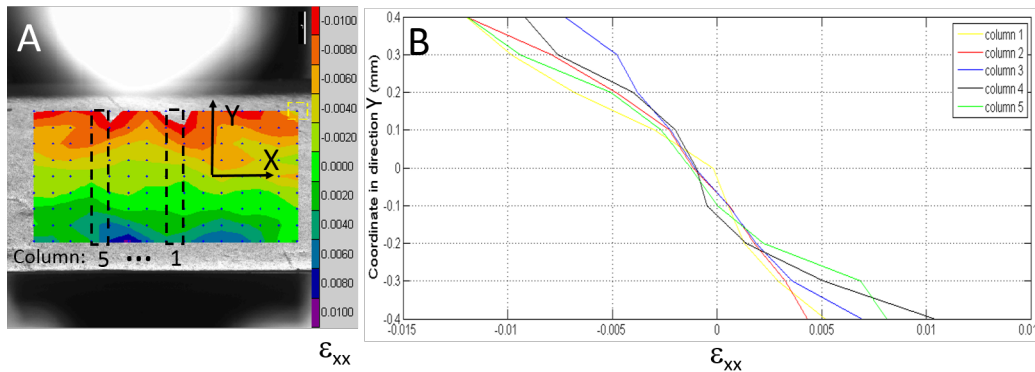


Figure D.8 – DIC strain distribution for intact dentin beam. (A) Three-point bending test and selected areas to acquire ϵ_{xx} using DIC. (B) ϵ_{xx} distribution along direction Y (from DIC).

the location marked in Fig. D.9. And, at this location, σ_{yy} and σ_{zz} were found to be below 0.4MPa, which were much lower than σ_{xx} , hence the possibility to apply the formula $E_t = \frac{\sigma_{xx}}{\epsilon_{xx}}$.

In order to validate our method, the deformations measured by DIC and FEM (using our experimental result and the result from Rees et al. (1994)) were compared (Fig. D.10). Strain distribution along Y coordinates under the indenter (column 2 in Fig. D.8) measured by DIC was selected as an example

Discussion

Large discrepancies have been found in the literature concerning dentin mechanical properties (and especially its Young’s modulus). It is probably caused by stress and strain assessment errors. Indeed Bonfield & Datta [1974] compared the value of elastic modulus for compact bone with two kinds of

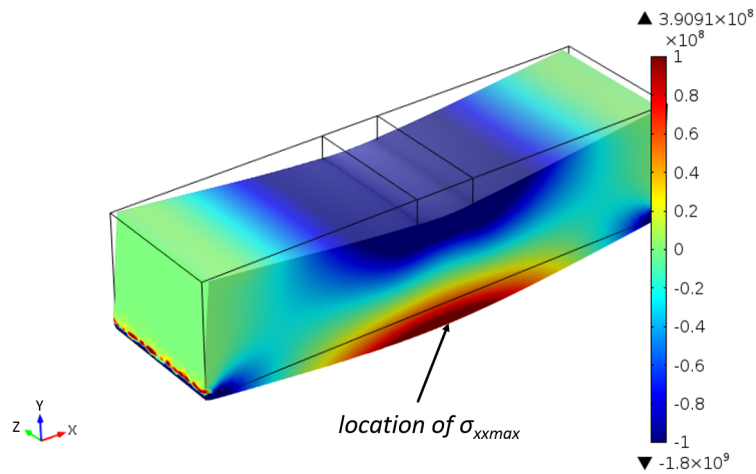


Figure D.9 – σ_{xx} distribution estimation (unit of color scale bar: Pa)

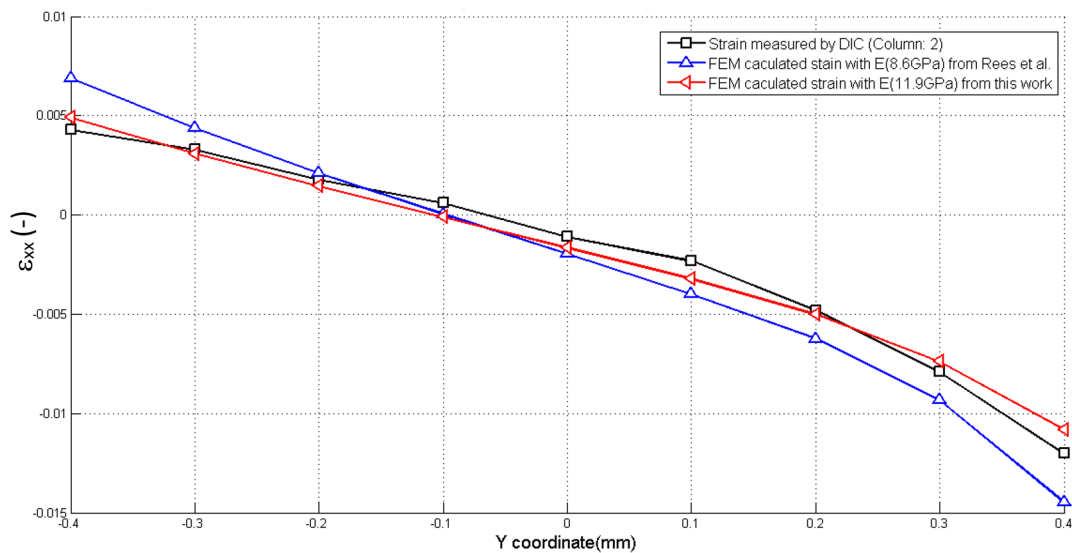


Figure D.10 – ϵ_{xx} comparison between FEM and DIC along Y coordinate

micro-strain measuring techniques: they have shown that with different strain measurements, the value of elastic modulus was clearly affected. It is likely to be the same while assessing dentin mechanical properties. The elastic modulus is also very sensitive to the strain rate. As reported by Jantarat et al. [2002] and McElhaney [1966], great differences of elastic modulus can be observed due to the strain rate variation (from 0.001 to 1500 per second).

From the recalculation of the selected articles, it can be inferred that the Bernoulli-Euler beam equation is probably used to get the flexural strength and elastic modulus. However, Bernoulli-Euler beam theory is based on the hypothesis of a large slenderness ratio. Depending on the slenderness

Appendix D. A New Method Combining Finite Element Analysis and Digital Image Correlation to Assess Macroscopic Mechanical Properties of Dentin

ratio, the Bernoulli-Euler equation can lead to an inaccurate assessment of stresses. This would also lead to an error of evaluation of the modulus. Compared with the results of four-point bending test of [Eltit et al. \[2013\]](#), the maximum bending stress of root dentin obtained from classical beam equation was reported at more than 300MPa. This is in contradiction with the maximum tensile stress deduced from uniaxial tension test [[Bowen & Rodriguez, 1962](#); [Sano et al., 1994](#); [Palamara et al., 2000](#)]. However, the maximum bending stress of 55MPa and 132 MPa (for root and coronal dentin, respectively) deduced using FEA stress assessment seems to better match the results from the literature value, which reported a value of 31MPa to 130MPa under uniaxial tension tests [[Bowen & Rodriguez, 1962](#); [Sano et al., 1994](#); [Marshall et al., 1997](#)]. Thus, it can be inferred that with such sample dimensions, it is inaccurate to use the classical beam theory to assess the stress distribution inside the beam, and that would also lead to an incorrect estimate of the elastic modulus. However, elastic modulus determined with beam theory can be used as a comparative tool.

For stress determination, the geometry and positioning of sample are crucial. Some non-parallel alignment of the load due to not-well controlled geometry of the sample in uniaxial compression can occur. In order to well bond the sample with the grips of the machine, an adhesive glue can be used in the tension test [[Sano et al., 1994](#)], but this would increase the relaxation effects. Those effects are not taken into account when using Bernoulli-Euler beam equation to assess stresses but FEA can also well avoid the influence of those effects.

For strain determination, [Sano et al. \[1994\]](#) and [Rees et al. \[1994\]](#) used the load-displacement curve from the testing device to get the strain and elastic modulus. Lower values of elastic modulus were reported, which were probably caused by the inaccurate evaluations of strain: the measured displacement includes not only the whole sample displacement but also motions of the loading set-up. This is leading to the impossibility of comparing the results in different studies done on different machines. In our study, DIC was used to assess the strain on the external surface of the beam for three-point bending. It allows a more global assessment of strain (on a whole surface) with a satisfactory resolution. The accuracy of the DIC technique is determined by the optical resolution of the focusing system used for the image capture. The precision, therefore, mainly depends on the pixel resolution of the camera. The camera in the microscope used in our test has a size of 1280 (horizontal) by 1024 (vertical) pixels, which is higher than in the study of [Palamara et al. \[2000\]](#), and thus may lead to a higher resolution on the strain measurement. Moreover, according to Fig. 11, we can observe that

the values from our finite element model matches well with our experimental results.

As discussed above, stress and strain assessment is crucial to get accurate estimates of dentin mechanical properties. For three-point bending test, combined FEA for stress estimate and DIC for strain determination may be a method to explore the dentin elastic modulus and maximum tensile stress. Elastic modulus determined by our method is E_t (because the tensile stress direction is perpendicular to the tubular orientation); our feasibility test allowed us to measure E_t as 11.9GPa, and the maximum stress as 143.9MPa. The elastic modulus measured here matches the results in the references [Bowen & Rodriguez, 1962; Sano et al., 1994; Palamara et al., 2000], in which elastic moduli are reported between 6 and 19GPa (determined by tension tests). Similarly, our maximum tensile stress corresponds to the magnitude of uniaxial tension test results [Bowen & Rodriguez, 1962; Sano et al., 1994; Marshall et al., 1997].

However, for dentin sample, the location in the tooth from where the sample comes, may significantly influence the properties of the mechanical test. The density of the mineral phase indeed varies due to the change in tubule density and diameter in the different dentin locations. The statistical structure characteristics have been summarized by Marshall et al. [1997]. The percentage of peritubular dentin in crown dentin varies from 60% near the pulp cavity to 3% at the dentin-enamel junction, and the percentage tubule area and diameter vary from about 22% and 2.5 μm near the pulp to 1% and 0.8 μm at the dentin enamel junction (DEJ). The intertubular matrix area varies from 12% at the pulp cavity up to 96% near the DEJ. It can be inferred that there is a sharp variation in the density and diameter size of tubules and of peritubular dentin in the different locations from the pulp to dentin-enamel junction [Garberoglio & Brännström, 1976]. So, the variations in the properties of the dentin sample may be explained probably by the mineral phase density changes within the tooth. Tests on bone specimen have been found that the elastic modulus is proportional related to the mineral density Carter & Hayes [1977]. As local mineral densities are different in the parts of peritubular and intertubular dentin, indentation tests on dentin samples have shown the elastic modulus strongly depends on the location Ziskind et al. [2011]. So, the bending test measured here can be done on different samples taken from different depths to assess the variation of E_t with depth (and also with mineral density).

To model the dependency of the dentin modulus with its components ratio, a classical composite model can be used. To do this, the local moduli are needed. With an indentation system, Kinney et al. Kinney et al. [1996] have reported significantly different elastic modulus for peritubular (29.8 GPa)

Appendix D. A New Method Combining Finite Element Analysis and Digital Image Correlation to Assess Macroscopic Mechanical Properties of Dentin

and intertubular (18-21GPa). According to the composite modulus model, elastic modulus in direction 2 can be described as:

$$E_t = \frac{E_p E_i}{E_p r_i + E_i r_p}$$

where E_p , E_i are the elastic modulus of peritubular and intertubular dentin, respectively, and r_i , r_p are the area ratios of intertubular and peritubular dentin respectively. Without considering the percentage of tubular area, an approximation of the elastic modulus in X direction can be inferred between 25 and 18GPa. However, the density of the tubules changes a lot within the tooth. With the addition of the tubular ratio in the composite model, the elastic modulus becomes as:

$$E_t = \frac{1}{\frac{r_p}{E_p} + \frac{r_i}{E_i} + \frac{r_{tubule}}{E_{tubule}}}$$

where r_{tubule} and E_{tubule} are ratio and modulus for the tubule respectively. So since a very low modulus is expected for the tubules, we can expect a significant decrease of E_t .

Besides, lower values of elastic modulus on dentin have also been found by [Marshall et al. \[1997\]](#). The elastic moduli should be more reasonably represented as a range of values rather one absolute value or more accurate values should be obtained to show the relation between the exact location within the tooth (and also mineral density). Other factors like the storage medium, the time span between extraction and testing, the tooth age, and the condition of the tooth (sound vs. carious) might also influence the mechanical properties of dentin.

Conclusion of three point bending test

Errors in stress and strain assessment during mechanical tests can possibly lead to a mis-evaluation of the mechanical properties. In this paper, a review of dentinal mechanical properties has been done and large discrepancies were found in the literature.

Two articles of the literature using bending tests were selected and re-examined using FEA to highlight the importance of stress and strain evaluation to get mechanical properties. Then, a new method (using FEA and DIC) is proposed to better evaluate stress and strain distributions, and so elastic modulus. To illustrate and prove the feasibility of the method, elastic modulus and maximum

flexural stress were obtained for a dentinal sample and were respectively 11.9 GPa and 143.9 MPa. The next step of this study is to improve the stress field assessment in the beam by considering dentinal anisotropy in FEA.

Using accurate and robust methods to assess stress and strain is needed to avoid set-up dependent measurements. Keeping this idea as ultimate objective, an experimental protocol based on a three-point bending experiment under an optical microscope is proposed and it should perhaps trigger discussion on the standardization of dentinal sample mechanical testing. Being able to compare results of different research groups will indeed lead the community to a better understanding of the differences arising from other relevant factors such as species, age, disease, storage condition, etc. (instead of comparing indirectly their equipment).

RÉSUMÉ

La dentine est l'un des principaux éléments constitutifs de la dent humaine. Elle montre une structure hiérarchique. A l'échelle microscopique, la dentine est composée de tubules (porosité naturelle du tissu), de dentine péritubulaire et de dentine intertubulaire. La dentine contient des canaux microscopiques appelés tubules dentinaires. Les tubules rayonnent vers l'extérieur à travers la dentine de la pâte à la frontière extérieure cémentum ou émail. Le cours des tubules dentinaires est une légère courbe en "S" dans la couronne, mais les tubules sont plus droits dans les crêtes des incisives, les cuspidés et les racines. Les extrémités des tubules sont perpendiculaires à la jonction dentino-amélaire. La dentine péritubulaire est l'anneau environnant autour de la lumière tubulaire. La dentine intertubulaire est la matrice entourant la dentine péritubulaire. En raison des tubules dentinaires, la dentine peut être considérée comme un matériau poreux. La différence entre la dentine péritubulaire et la dentine intertubulaire est la teneur en minéraux des deux composants. Sur la base de cette structure tissulaire, la dentine est souvent modélisée comme un composite poreux renforcé de fibre continue avec des manchons péri-tubulaires comme renforcement et une matrice de dentine intertubulaire. À la nano-échelle, la dentine montre une structure bien organisée et complexe. Environ 50% (pourcentage en volume) de la dentine se compose d'une phase minérale d'apatite nanocristalline qui est une hydroxyapatite riche en carbonate. Un autre 30% (pourcentage en volume) est occupé par un réseau de fibrilles de collagène de type I, tandis que le reste est principalement de l'eau. L'hydroxyapatite est une forme minérale d'apatite de calcium. La dentine péritubulaire est une gaine minérale haute, dépourvue de fibrilles de collagène, tandis que la dentine intertubulaire environnante est une matrice composite faite

de fibrilles de protéines et d'hydroxyapatite. Le diamètre des fibres de collagène est d'environ 50 à 100 nm. Les fibrilles disposent dans un plan perpendiculaire à la direction du tubule. Dans ce plan, ils sont répartis au hasard. L'hydroxyapatite minérale est principalement extra fibrillaire. Les formes du minéral hydroxyapatites dépendent de l'emplacement. Ils varient continuellement d'aiguille-près de la pulpe à plat-comme près de l'émail. L'épaisseur de la cristallite est d'environ 5nm, indépendamment de l'emplacement. Dans la dentine périctubulaire, les cristaux d'hydroxyapatite n'ont pas d'orientation générale préférée. Dans la dentine intertubulaire, l'axe c de l'apatite des cristallites minérales préfère s'orienter le long de l'axe de la fibre de collagène. Les particules minérales alignées avec le collagène comprimé dans la dentine intertubulaire. Ce stress réparti peut agir comme un mécanisme de prévention des dommages à l'échelle nanométrique, en protégeant contre l'initiation de fissures due aux charges de mastication.

L'organisation de ces structures détermine fortement ses propriétés mécaniques. Dans la littérature, seules quelques études portent sur la relation entre la structure et la propriétés mécaniques de la dentine. Depuis le siècle dernier, la micro-structure et les propriétés mécaniques du tissu dentinaire ont été étudiées à différentes échelles par diverses techniques. Propriété élastique comme l'un des paramètres essentiels a été attiré une grande attention. Les cavités à l'intérieur de la dent sont réparées par les composites de résine. Le module du composite doit correspondre avec la substance dentinaire afin d'éviter la concentration du stress à l'interface dentine-restauration. En outre, les prédictions numériques en dentisterie nécessitent une connaissance approfondie du module élastique de la dentine. Cependant, le module de Young annoncé de dentine humaine montre une grande variabilité parmi toutes les mesures, basées soit sur la flexion, l'indentation, la tension, la compression ou les techniques d'ultrasons. Quatre causes de la variabilité sont inter-donneur, intra-donneur, artefact technique et problèmes expérimentaux (fausse géométrie). Ainsi, une évaluation bien établie de la structure géométrique et de la caractérisation mécanique de la dentine humaine est encore nécessaire. Le but de cette thèse est d'explorer les protocoles de caractérisation géométrique et mécanique de la dentine humaine, puis d'étudier ses propriétés mécaniques à différentes échelles. La connaissance de sa structure, de ses propriétés mécaniques et de ses déformations dues aux variations de l'environnement extérieur peuvent être utiles afin d'améliorer les protocoles de restauration de la dentine.

Dans ce travail, quatre techniques d'observation (μ CT, microscope optique, ESEM et microscope confocal) ont été explorées et comparées. Micro-CT fournit le plus grand champ d'image, permettant

une visualisation 3D de la dent entière. Cependant, la résolution limitée du voxel rend impossible de distinguer les constituants détaillés de la dentine (tubules, dentine pérítubulaire et dentine inter-tubulaire). Le microscope optique a une taille d'image modérée. C'est le moyen le plus simple. Un aperçu de la dentine à mi-échelle avec une résolution intermédiaire. Le contraste n'est pas suffisant pour observer quantitativement les différents composants de la dentine, mais il donne la géométrie de l'échantillon en peu de temps. ESEM possède une puissante capacité de contrôle de l'environnement avec une résolution et un contraste élevés. La dentine peut être observée sans aucune préparation de surface particulière, et ses composants principaux de structure sont visibles. Sur le contraste de fluorescence, la microscopie confocale est intéressante pour la visualisation 3D et la caractérisation de la structure poreuse de la dentine. La limitation principale de cette technique est la restriction de la profondeur de l'image (environ 50 μ m). Des caractéristiques géométriques, telles que la porosité et la distribution des tailles de pores, peuvent être évaluées, la haute résolution permettant de visualiser les branches fines. Comparée à l'observation 2D, elle permet d'obtenir des informations supplémentaires. Par exemple, les tubules montrent des structures en arbre plus complexes près de l'email que la forme en Y déduite des observations 2D. Ces résultats peuvent également nous fournir des données d'entrées pour une modélisation réaliste prenant en compte la structure poreuse complexe à l'intérieur de la dentine humaine. Malheureusement, l'analyse morphologique est limitée au réseau poreux dans lequel le fluide fluorescent peut pénétrer. De toute évidence, aucune de ces techniques d'observation ne peut être considérée comme la meilleure. Chaque technique a ses propres avantages et inconvénients. Pour différentes questions, il sera toujours nécessaire de choisir la bonne ou de peigner différentes technologies. Par exemple, bien que les méthodes de seuil choisies manuellement apportent du bruit dans les mesures par microscope confocal, elles peuvent être réduites par l'utilisation d'images SEM. D'autres techniques sont également disponibles, qui ne sont pas utilisées ici. Par exemple, le faisceau d'ions focalisé (FIB) combiné avec SEM (sous le mode BSE) peut être utilisé pour réaliser la visualisation 3D de la structure de la dentine avec de grands détails.

Les conditions environnementales externes (température et humidité relative) jouent un rôle important dans le comportement mécanique de la dentine. Durant la chirurgie dentaire générale, l'humidité relative de l'air est toujours considérée comme un facteur clé de la force de liaison entre le matériau de restauration et le substrat dentinaire. Cette liaison est également très sensible à l'humidité de l'environnement, avec une adhérence très faible à une humidité relative élevée de l'air. Ainsi, la com-

préhension de l'influence des conditions environnementales sur la dentine est cruciale pour anticiper les propriétés demandées pour les matériaux de restauration. Plusieurs études ont été faites pour caractériser le coefficient de dilatation thermique de la dentine humaine. La plus ancienne étude a été réalisée en utilisant un dilatomètre traditionnel dans de l'eau distillée. Une telle mesure globale ne fournit aucune information locale sur la réponse des différentes composantes de la micro-structure de la dentine. Plus tard, les informations locales ont été obtenues par interférométrie Moiré numérique et analyse thermo-mécanique. On a obtenu des preuves directes de deux grandes régions de déformation thermique: une expansion à basse température (inférieure à 55°C) et une contraction à des températures plus élevées. On a signalé que le coefficient de dilatation thermique dépendait non seulement de la plage de températures mais aussi de l'emplacement à l'intérieur de la dent. Récemment, la preuve de Forien et al. ont montré que le couplage fonctionnel assisté par l'eau entre les fibrilles de collagène et l'hydroxyapatite à l'intérieur de l'échantillon de dentine conduirait à une contrainte de compression après traitement thermique. Dans ce travail, un système intégré a été développé pour contrôler simultanément l'humidité et la température de l'environnement autour d'un dispositif de compression, équipé pour la mesure en temps réel de déformation DIC. Les erreurs de bruit ont été quantifiées dans la plage de quelques dixièmes de $\mu\epsilon$. Des tests de compression sur la dentine humaine ont été effectués dans ce système. Le module d'élasticité de la dentine humaine à l'échelle méso a été déterminé comme étant de 16.7GPa avec un écart type de 5.1GPa. Le rapport de Poisson était de 0.31. On n'a observé aucune forte influence d'humidité et de température sur ce module. On a exploré le comportement de dilatation de la dentine humaine avec l'humidité relative: une augmentation de l'humidité relative induit une dilatation isotrope importante de la dentine. Les effets thermiques ont été étudiés de la même manière. Étonnamment, nous avons observé une contraction de l'échantillon lorsque la température a augmenté. Ce comportement est lié à une modification des molécules d'eau autour des fibrilles de collagène dans la dentine. D'autres méthodes ont été testées pour mesurer les propriétés mécaniques de la mésoéchelle: RUS et essais de flexion à trois points (voir annexe D). La méthode RUS fournit toutes les constantes élastiques en un seul test. Les résultats montrent que les modules élastiques de la dentine humaine présentent de légères caractéristiques isotropes transversales et une forte anisotropie dans le ratio de Poisson avec peu de variation entre nos échantillons. Cependant, les résultats obtenus sont comparables aux résultats de compression, mais plus sensibles aux micro-défauts.

Les propriétés mécaniques macroscopiques de la dentine humaine ont été mesurées par des es-

sais de compression insitu dans le chapitre précédent. Cependant, ces propriétés n'étaient pas liées à la micro-structure des échantillons. Pour les applications biomédicales, ou pour la modélisation fine, il est intéressant de relier une micro-structure comme observée par exemple en partie aux propriétés macroscopiques. Ceci requiert évidemment une connaissance approfondie des propriétés de chaque composant de la dentine. Le module élastique pour les deux composants de la dentine (dentine péri-tubulaire et intertubulaire) a été déterminé par nanoindentation. Deux méthodes (CSM et déchargement) ont été utilisées. Les localisations des indentations ont été déterminées par des observations AFM. Les modules élastiques résultants de la dent péri et intertubulaire ont été déterminés comme 16.2GPa et 26.7GPa pour les mesures CSM, et comme 16.1GPa et 25.1GPa, pour la méthode de déchargement. Les rapports de surface de chaque composant dentinaire ont été estimés à partir du test d'indentation associé à l'observation de localisation par AFM. Les valeurs moyennes pour les tubules, la dentine péri-tubulaire et la dentine intertubulaire ont été estimés: 5.2%, 10.1% et 84.6%. La loi de mélange a ensuite été utilisée pour prédire les propriétés efficaces de méso-échelle, qui sont trouvées dans la plage de celles déterminées par des essais de compression. Le comportement de fluage de la dentine a également été évalué et modélisé par un hamburger à quatre éléments modèle.

Pour résumer, une étude morphologique et mécanique du tissu dentinaire a été effectuée. De nouvelles techniques, par exemple, la microscopie confocale ont été utilisées et ont montré leur utilité dans le but de donner un nouvel éclairage sur le tissu dentinaire. Les protocoles d'essais mécaniques qui ont été mis en place à différentes échelles permettront de mieux comprendre la relation structure-propriété en utilisant les outils d'observation validés dans ce travail.

Titre : Caractérisation géométrique et mécanique multi-échelle de la dentine humaine

Mots clés : propriétés mécaniques, dentine humaine, étude multi-échelles, morphologie dentinaire

Résumé :

La dentine est l'un des principaux éléments constitutifs de la dent humaine. Elle montre une structure hiérarchique. A l'échelle microscopique, la dentine est composée de tubules (porosité naturelle du tissu), de dentine pérítubulaire et de dentine intertubulaire. L'organisation de ces structures détermine fortement ses propriétés mécaniques. La connaissance de sa structure, de ses propriétés mécaniques et de ses déformations dues aux variations de l'environnement extérieur peuvent être utiles afin d'améliorer les protocoles de restauration de la dentine. Dans ce travail, quatre techniques d'observation (μ CT, microscope optique, ESEM et microscope confocal) ont été explorées et comparées. En particulier, la microscopie confocale a été utilisée afin de visualiser en 3D le réseau poreux dentinaire. Comparée à l'observation 2D, elle permet d'obtenir des informations supplémentaires. Par exemple, les tubules montrent des structures en arbre plus complexes près de l'email que la forme en Y déduite des observations 2D. Ces résultats peuvent également nous fournir des données d'entrées pour une modélisation réaliste prenant en compte la structure poreuse complexe à l'intérieur de la dentine humaine.

Par la suite, un test de compression associé à la corrélation d'images numérique a été mis en place avec un système qui permet de commander simultanément l'humidité et la température de l'environnement. Grâce à ce dispositif, le module d'élasticité de la dentine humaine a été mesuré (16.7GPa avec un écart-type de 5.1GPa), et le coefficient de Poisson a été estimé à 0.31.

Le comportement de dilatation de la dentine humaine avec l'humidité relative a été étudié. La spectroscopie par résonance ultrasonore (RUS) a été utilisée et ses résultats comparés au test de compression mécanique. À échelle microscopique, les propriétés mécaniques de la dentine pérítubulaire et de la dentine intertubulaire ont été caractérisées par nanoindentation. Les deux méthodes utilisées (méthode dynamique CSM et méthode de déchargement statique) indiquent les mêmes tendances en matière de module d'Young pour les deux composantes de la dentine. La dentine pérítubulaire a un module d'élasticité plus élevé (26.7GPa avec un écart type de 3.1GPa) que la dentine intertubulaire (16.2GPa avec un écart type de 5.5GPa). De plus, le comportement en fluage de la dentine a été étudié par nanoindentation. Il se trouve qu'un modèle de Maxwell-Voigt à quatre éléments peut être utilisé pour évaluer le comportement en fluage de la dentine

Pour résumer, une étude morphologique et mécanique du tissu dentinaire a été effectuée. De nouvelles techniques, par exemple, la microscopie confocale ont été utilisées et ont montré leur utilité dans le but de donner un nouvel éclairage sur le tissu dentinaire. Les protocoles d'essais mécaniques qui ont été mis en place à différentes échelles permettront de mieux comprendre la relation structure-propriété en utilisant les outils d'observation validés dans ce travail.

Title : Multiscale geometrical and mechanical characterization of intact human dentin

Keywords : mechanical properties, human dentin, multi-scale

Abstract :

Human dentin is one of the main components of human tooth. It shows a hierarchical structure from a multi-scale point of view. Generally speaking, dentin can be seen as a hard biomaterial consisting in 3 phases: the porous phase made of tubules, the inclusion phase made of peritubular dentin and the matrix phase made of intertubular dentin. These hierarchical structures strongly determine its mechanical properties. The knowledge of its structure, its mechanical property and its deformation behavior due to the variation of the external environment may be useful to improve the dentin restoration process. In this work, four observation techniques (μ CT, optical microscope, ESEM and confocal microscope) have been used and compared. Particularly, confocal microscopy is proposed to allow 3D visualization of the complex dentin porous network. Compared with usual 2D observation tool, it may provide new information. For example, near the DEJ, tubules show a more complex tree structure than the Y-shaped deduced from 2D observations. These findings may also allow to achieve more realistic modeling considering the complex porous structure inside human dentin.

Later on, compression test associated with DIC was carried out within an integrated system which can control simultaneously the humidity and the temperature of the environment. Using this system, the elastic modulus of human dentin was measured to be 16.7GPa with a standard deviation of 5.1GPa. And the Poisson's ratio was found to be 0.31.

The dilatation behavior of human dentin due to relative humidity was also explored. Furthermore, resonant ultrasound spectroscopy was performed in order to compare the results with these mechanical testing. At the micro-scale, the mechanical properties of peritubular dentin and intertubular dentin were characterized by nanoindentation. The two methods used in this work (dynamic CSM method and the static unload method) present the same trends of elastic moduli for the two components. Peritubular dentin has a higher elastic modulus (26.7GPa with a standard deviation of 3.1GPa) than intertubular dentin (16.2GPa with a standard deviation of 5.5GPa). Besides, the creep behavior of dentin was assessed by nanoindentation. Four elements Maxwell-Voigt model can be used to model dentin's creep behavior.

To sum up, a morphological and mechanical study of the dentinal tissue has been performed. New techniques, such as confocal microscopy have been used and showed their usefulness in order to give new insight into the dentinal tissue. The mechanical testing protocols that have been set up at different scales will enable to better understand the structure-property relationship by using them associated with the observation tools validated in this work.

